ADDRESSING THE ROLE OF ELECTRODE MICROSTRUCTURE IN LI-ION BATTERY THERMO-ELECTROCHEMICAL INTERACTION

A Thesis

by

DON VU

Submitted to the Office of Graduate and Professional Studies of
Texas A&M University
in partial fulfillment of the requirements for the degree of

MASTER OF SCIENCE

Chair of Committee,	Partha P. Mukherjee
Committee Members,	Sarbajit Banerjee
	Hong Liang
Head of Department,	Andreas Polycarpou

August 2017

Major Subject: Mechanical Engineering

ABSTRACT

Lithium-ion batteries are a ubiquitous part of modern technology as portability and reusability are heavily emphasized. As this is the case, it is important to further improve their electrochemical capabilities while minimizing the increase in thermal effects and maximizing safety. There are many ways to do this, but one area that has had little focus is the role of microstructure morphology on the thermo-electrochemical performance of the cell. Thus, a study was done to characterize how changes in the microstructure affect properties pertinent to the thermal and electrochemical characterization. The thermal and electrochemical effects were then characterized considering the changes in the microstructure.

The research done here has developed functional relationships that can be used to determine the active area, conductivity, and tortuosity in a graphite anode and NMC cathode. Changes in the porosity volume percentage, binder morphology, and binder volume percentage can cause significant variation in these properties. As those properties change, there are possibly significant changes in the overpotential, and concentration and potential gradient that then change the temperature rise and electrochemical performance in the cell.

CONTRIBUTORS AND FUNDING SOURCES

Contributors Section

This work was supervised by a thesis committee consisting of Dr. Partha P. Mukherjee of the Department of Mechanical Engineering, Dr. Hong Liang of the Department of Mechanical Engineering, and Dr. Sarbajit Banerjee of the Department of Chemistry.

All work for the thesis was completed by the student, under the advisement of Dr. Partha P. Mukherjee and supervising PhD student Aashutosh Mistry.

Funding Sources

Graduate study was supported by a fellowship from Texas A&M University.

TABLE OF CONTENTS

Page

LIST OF FIGURES

Page

LIST OF TABLES

Page

1. INTRODUCTION

As lithium-ion batteries come to enjoy a more pervasive role in the modern world due to the rapid growth of portable electronics and electric vehicles there is an increasing need to improve the size, capacity, weight, and price. Right now, Li-ion batteries are widely considered to be the best storage technology available due to their ability to deliver high voltage, high energy, cycling, and storage capacities. However, that does not mean that Li-ion cells do not have drawbacks as well. A major component that affects the capabilities of a Li-ion cell is the electrode. The structure, components, and material used in the electrode can lead to a wide spread in how well or how poorly a cell performs. A systematic understanding how changes in the cathode microstructure affects cell performance and how variation in the makeup of the cathode affects the electrode microstructure itself are important to addressing the problems that exist in Li-ion cells.

Li-ion batteries are attractive as an energy storage medium due to their high capacity, high power output, high efficiency, low maintenance, compact size, and a variety of different li-ion cell types that allow for versatility and use in many different applications. However, li-ion batteries do have their faults. Li-ion batteries are expensive, have problems with overcharge and over discharge, safety concerns, sensitive to temperature, and capacity loss as the cell ages. Another issue is that while the benefits of a li-ion cell is that it can have high capacity and high power output, the reality is that often times, these are often mutually exclusive choices as can be seen in the Ragone plot in Figure 1. This is important to note because of the recent surge in interest in electric vehicles. While EVs are viable, they use relatively small batteries. EV battery systems need to have high power densities to drive the motor while also being safe to use but the li-ion technologies that apply also have low energy densities. Increasing the energy density typically results in cycling or power losses. In order to improve the outlook for EVs and li-ion batteries in general, it is crucial to improve safety, energy density, and power output simultaneously.

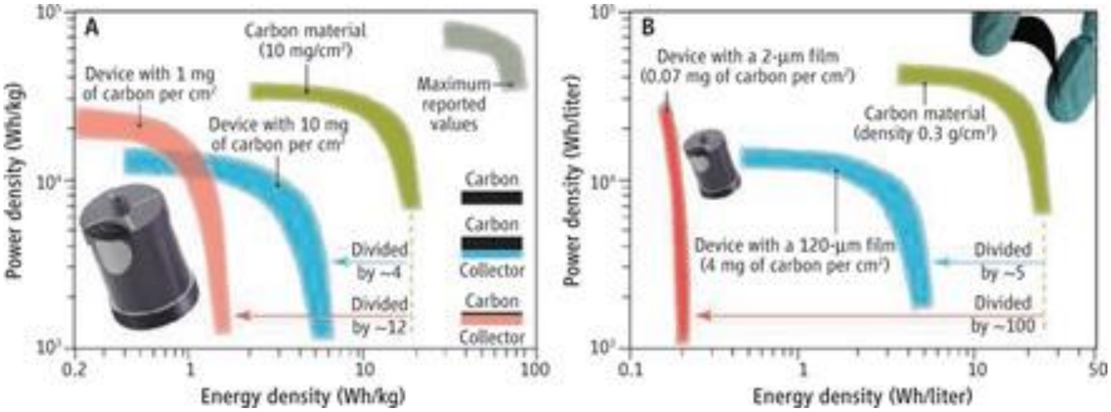

Figure 1. Ragone Plot on (a) a gravimetric basis and (b) a volumetric basis from Gogotsi and Simon [1]

1.1 Basic Electrochemical Cell

An electrochemical cell is primarily made up of two electrodes, the anode and the cathode, and an ionically conductive electrolyte that separates the two. The electrolyte conducts the ionic component of the electrochemical reaction between the anode and cathode while simultaneously preventing electrons from passing through it and forcing it through an external circuit. Since the ionic conductivity is much lower than the electronic conductivity, the electrodes typically have a high surface area while being separated by a thin electrolyte to maximize the ionic mobility. A metallic current collector delivers an electronic current from the electrodes to an external circuit.

This electronic current is generated during the electrochemical reaction by the transport of ions from the positive electrode to the negative anode via the electrolyte and the transport of electrons via the current collectors during discharge.[2]

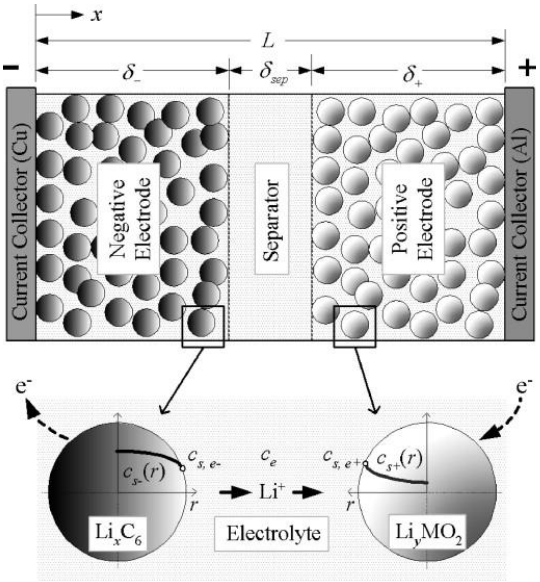

Figure 2. Li-ion Schematic from Smith, Rahn, and Wang [3]

In a rechargeable battery, each electrode is capable of reversible chemical reactions. These reversible chemical reactions involve displacement and insertion, or intercalation, reactions. The solid cathode undergoes the intercalation reaction while the anode often undergoes displacement reactions, but intercalation reactions are also common. Electrodes that undergo intercalation reactions consist of electronically conducting host structures where cations can insert or extract from reversibly. So for a rechargeable lithium-ion secondary cell, seen in Figure 2, lithium ions deintercalate from the anode and are transported through the electrolyte where it then lithiates onto the cathode during discharge and once the cell is completely discharged, an externally applied electrical energy can be used to recharge the cell by reversing the electrochemical process to cause lithium ions to delithiate from the cathode to intercalate into the anode. An example of the cell electrochemical reaction during discharge with $LiCoO_2$ is as follows:

$$\text{Anode: } Li_xC_6 \rightleftharpoons 6C + xLi^+ + e^-$$

$$\text{Cathode: } Li_{1-x}CoO_2 \rightleftharpoons LiCoO_2 + xLi^+ + \ xe^-$$

$$\text{Overall: } Li_{1-x}CoO_2 + Li_xC_6 \rightleftharpoons LiCoO_2 + 6C$$

1.1.1 Li-ion Battery Components

In the Li-ion cell, there are five components that need to be addressed: the anode, the separator, the electrolyte, the cathode, the separator, and the current collectors. During discharge, the anode is the electrode at which oxidation occurs. Oxidation refers to the electron transfer from a molecule or an ion to change its oxidation state. In Li-ion batteries, Li metal was once the active material used for anodes because of its low density of 0.59 g/cm^3, high electrochemical potential of 3.04V, and a specific capacity of 3860 mAh/g but it was discovered that cycling had a low coulombic efficiency that led to short cycling life, and dendrite formation was also a safety concern. These dendrites penetrate the separator that prevent electron flow through the cell which can cause short circuits that can lead to thermal runaway. [4]

Since lithium was not a viable choice, graphite has become a common choice as an anode material. When graphite is fully intercalated as LiC_6, graphite has a specific capacity at only 372 mAh/g. [5]The use of graphite avoids cycling and safety concerns that lithium metal has because lithium ions can intercalate reversibly into the layered structure of graphite which prevents dendrite formation. As a result, coulombic efficiency increases and cycling life but graphite is still generally limited by its low specific capacity and rate capabilities. In combination with several chemical like pyrolytic processing and physical modifications like mechanical milling, carbon negative electrodes continue to show electrochemical performances as well.[6]

The separator is a porous media between the cathode and anode that allows for the flow of ions while preventing the flow of electrons between the electrodes. The separator also needs to be mechanically and dimensionally stable, chemically resistant to degradation, readily wetted by the electrolyte, and uniform in its properties. All Li-ion batteries use nonaqueous electrolytes because of the reactivity of lithium in aqueous solutions. Most cells use microporous membranes made of polyolefins that fill the necessary requirements as the separator. These separators are very thin <30 μm and are made of polyethylene, polypropylene, or a laminate of the two. Polyolefins provide good mechanical properties, chemical stability, and reasonable costs and are compatible with most cell chemistries while also able to cycle for hundreds of cycle with minimal degradation of its chemical and physical properties. Out of all the components in the battery, the separator has seen the least amount of change to its material ingredients over time.[7]

In most Li-ion batteries, the most commonly used electrolyte are nonaqueous liquid electrolytes that consist of lithium salts dissolved in organic carbonates such as propylene carbonate(PC), dimethyl carbonate(DMC), diethyl carbonate(DEC), ethyl methyl carbonate(EMC), or a mixture of DMC/DEC and ethylene carbonate(EC). The presence of EC provides a passivating SEI layer onto carbon electrodes that prevents the ionic transfer of carbonates while allowing the ionic transfer of lithium. The SEI layer provides stability by preventing further electrolyte reduction or oxidation. [8]The formation of this SEI layer makes it possible to use graphite as an anode material. (find exact source) However, cycling over time can result in degradation of SEI and reformation that further depletes Li and electrolyte which results in capacity losses.[9]

Carbonates are good solvents for Li salts with low viscosity that results in a low activation energy for Li^+ ion diffusion. An SEI layer can also stabilize Ni and Mn oxides on cathodes but at the expense of higher Li^+ ion activation energy but there are other options to decrease the activation energy such as doping to remove Ni from the cathode surface or coating particles with Li or a conductive additive that replaces the SEI layer. One concern though is that organic electrolytes like these are flammable which can be a safety issue. So ionic liquids have been considered as an alternative since they are not flammable but they are too viscous and lead to a decrease in rate capabilities compared to liquid carbonates. There are solid electrolytes and aqueous electrolytes but solid electrolytes have conductivities that are far lower and the presence of water in aqueous electrolytes will cause exothermic reactions when in contact with lithium.[10]

The current collectors are also critical components of a lithium ion battery. While the anode and cathode are comprised of a porous active material that is needed to store energy, the electronic conductivity is usually low. The current collector is needed to provide an electronically conductive path through the electrode to minimize the resistance in the battery while also acting as a substrate for the active material. In a typical cell, the current collectors at the anode and cathode are different. The anode current collector is copper, while the cathode current collector is aluminum.[11]

Current collectors need to be electronically conductive while also being resistant to degradation. [12]For instance, aluminum is the current collector of choice for high voltage batteries since it is inexpensive, widely available, as well as being highly electronically conductive. In air and aqueous solutions, Al can be protected by an Al_2O_3 passivation layer but Al does experience pitting after extensive cycling and severe corrosion when used in certain battery chemistries. At low potentials near 0V, a high cathodic current density is induced that leads to a Li-Al alloying process that hinders the ability of aluminum as a current collector in negative electrodes. [13]Although corrosion occurs at higher voltages, a passivation layer also forms that protects the aluminum from further corrosion which makes it a suitable current collector for positive electrodes. [14]

Copper is another highly conductive material that is often used for anodes. While aluminum is unstable at low potentials, copper is stable which makes it a good current collector for negative electrodes even though it does not form a passivation layer that prevents corrosion. However, at high potentials, copper corrosion is a concern which then makes it a poor choice as a current collector in positive electrodes. [15]

Finally, the cathode can be considered to be the most important part of the battery structure. The cathode is the positive electrode where chemical reduction occurs in a discharging cell. During discharge, electrons move through the circuit and cations move through the electrolyte towards the cathode. Then the process reverses when charging in a Li-ion battery. While many parts of the battery have standardized materials, there are still many different materials that can serve as the cathode active material. The active material is a major determinant in the performance and cost of a Li-ion battery. Like the graphite anode mentioned earlier, the necessary requirement for a cathode material in li-ion batteries is that it needs to allow for intercalation reaction of lithium cations. As a result, most cathodes are generally prepared while lithiated so that they can be prepared with delithiated anodes. Since the most commonly used anode, graphite, imposes a -0.1 V cell potential, cathodes should have a high average potential to maximize energy density and to compensate for the graphitic anode. High specific capacity is preferred but this limits the active material choices to first-row transition metals like Mn, Fe, Co, and Ni.[16] Presently, most cathodes used today are either metal oxides or polyanionic compounds. Layered Transition Metal Oxides, specifically NMC, will be the main focus in this thesis.

The layered transition metal oxides include materials such as $LiCoO_2$ (LCO), $LiNi_{0.8}Co_{0.15}Al_{0.05}O_2$(NCA), and $LiNi_{1/3}Co_{1/3}Mn_{1/3}O_2$(NMC). Layered transition metal oxides have structures where Li and the transition metals are located in octahedral sites that occupy alternating layers in a cubic close-packed oxygen array. This layered structure allows for intercalation and reversible deintercalation in the cathode. In Li_xCoO_2, this gives a practical specific capacity of 140mAh/g and specific energy of 546 Wh/kg when $1 \geq x \geq 0.5$. Full delithiation when $x<0.5$ can result in higher practical capcity but this can lead to cycling losses due to unwanted side reactions that increase cell impedance and structural instability. [17]$LiNiO_2$ was also studied at one point due to the lower cost of production compared to $LiCoO_2$ while also having higher energy density as well. However, $LiNiO_2$ has a tendency to lose lithium and reduce Ni to Ni^{2+} which results with Ni^{2+} migrating into Li^+ sites due to similarities in their sizes. To overcome these obstacles, Ni was partially substituted with Co to improve the cationic disordering resulting in compositions like $LiNi_{0.8}Co_{0.2}O_2$(LNCO). Cobalt has an extra benefit of reducing oxygen loss at high states of charge which improves safety. To improve thermal stability of LNCO at high states of charge, aluminum can be used as a coating or a doping agent to produce $LiNi_{0.8}Co_{0.15}Al_{0.05}O_2$ (NCA). The presence of Al improves the thermal and electrochemical properties by improving the capacity to 180-200 mAh/g and specific energy of 680-760 Wh/kg.[17]

Another important doping agent is manganese. Li_xMnO_{2+y}(LMO) cells have shown to have excellent cycling characteristics and rate capabilities but poor capacity. LMO cells typically convert to a spinel structure during cycling but some forms like

Li_2MnO_3 can be considered layered structures similar to LCO except there is alternate layering of Li and$Li_{1/3}Mn_{2/3}$ instead of just Li. The problem with this compound is that there is a noticeable oxygen loss during initial charge as well as the loss of Li_2O from the structure and ion exchange during discharge. To improve on this, the development of $LiNi_{0.5}Mn_{0.5}O_2$(LMNO) was one of the options pursued. Unlike LMOs, LMNO does not convert to a spinel structure since all Mn remain tetravalent instead of reducing to a trivalent form. One of the other features of LNMO is that it allows for anti-site mixing so that some Ni^{2+} ions will locate itself in Li sites while some Li^+ will locate itself into transition metal sites. Mn will place itself in sites to surround the Li^+ ion while Ni ions will occupy the sites adjacent to to Mn. An advantage of this anti-site mixing is decreased cation mixing which will then improve rate capabilities. However, the presence of Ni also decreases the Li diffusivity as well. To improve diffusivity, the addition of Co has been found to be successful. This leads to the development of $Li[Ni_{1/3}Co_{1/3}Mn_{1/3}]O_2$(NMC) which combines Ni, Co, and Mn in the cell. NMC has better electrochemical properties in addition to better structural, chemical, and thermal stability compared to LCO and NCA which makes it a promising candidate for batteries in consumer electronics as well as larger scale devices such as EVs. However, the presence of cobalt makes it costly to manufacture.[5, 17, 18]

When it comes to the electrodes, there are additional materials that need to be included for it to function. The binder and conductive additive are key additions that are necessary to increase the mechanical durability and conductivity of the cathode. The binder is critical in preserving the structural integrity of the electrodes. While the conductive additive increases the conductivity of the active material, which is typically very low. The binder and the conductive additive are mixed to form a porous conductive matrix into which, an active material is inserted into. The mixture of binder and conductive additive provides a path for electron conduction and provides a structure into which all the active material particles can become a porous electrode structure. The binder and conductive additive matrix also has a requirement of being able to handle the mechanical load due to the expansion of the active material particle due to volume change as well as its neighboring particles during. A common binder used is PVdF and most conductive additives are a form of carbon like acetylene black. Since the anode is typically graphite, the addition of carbon additives are unneeded whereas the cathode needs carbon additives. [19] Studies have shown that better adhesion can improve capacity during cycling, especially when the electrode exhibit quick volume expansion. A stronger bond from the binder can also increase the conductivity as it provides an improved conductive particle network which leads to better capacity during cycling. When the binder loading is low, it can lead to worse conductivity and flaking and mechanical degradation of the electrode that leads to capacity loss as well.[20] While higher binder phase can be beneficial, too high of a ratio can lead to an ion-blocking effect but too much conductive additive can lead to agglomeration that creates cell-resistant growth. So a balanced ratio of binder and conductive additive is necessary to stabilize the cell resistance.[21]

1.2 Electrochemical Performance Criteria

Several electrical, thermal, and mechanical factors are taken into account when studying battery technology. Right now, different technologies have different characteristic advantages. For example, lead-acid batteries are cheap but have poor cycling abilities and energy density, NiMH provide good power but have lower capacities and shorter cycle lifes, and Li-ion have high energy densities but lower power densities. In studies, maximizing energy and power capabilities has been a primary goal as providing high power and capacity is one of the goals in large scale energy systems. Different cathode active material choices have proven to affect a cell's specific capacity and specific power. [7]

Fast recharge capabilities is another design goal as well. For many battery technologies, increasing the rate of charge has detrimental effects on the discharge capacity of a cell. The goal is to have the amount of specific energy a device and the percentage of maximum discharge be the same regardless of charge rate but in many cases, the capacity will decrease as charge rate increases. Li-ion batteries are particularly handicapped by fast charging as ohmic drops in the anode results in Li plating which causes performance degradation and is a safety concern. [7]

As Li-ion cells are a primary focus in automotive applications, it is also important to study cell capabilities at low temperatures for regions in colder climates. Power delivery and charge and discharge capability of cells at temperatures below -20

°C needs to be considered especially with regards to the electrolyte as the electrolyte is typically in a liquid phase which can be affected by freezing and phase change.

Cell cycle-life is another parameter that research tries to optimize as well. Some technologies age faster but it doesn’t necessarily mean that a cell capable of more cycles is better. For example, a cell that is capable of 1000 cycles but only has a capacity 10 Wh/kg is, at best, equivalent to a cell capable of 100 cycles but has a capacity 100 Wh/kg. However, the cycle life depends on several factors such as the chemistry, discharge and charge rates, temperature, and previous storage. Even cells from the same manufacturer can vary from cell to cell. So, to accurately determine cycle life, multiple cells from a batch needs to be tested to determine the cell capacity. it is prudent to observe the effect on discharge energy in terms of cycle as well as how well discharge energy is retained. Generally, a cell’s end of life is determined to be when the cell’s capacity drops to 50-80% of its initial capacity.[17]

Li-ion cells eventually go through self-discharge as well. This is determined as the amount of voltage decay and capacity loss over a set amount of rest time. Ideally, a cells should go through as little self-discharge as possible. Self-discharge profiles typically follow the discharge profile of a cell as self-discharge is basically the same as low rate discharge.[6]

1.3 Safety and Thermal Performance Criteria

Safety is a key aspect of li-ion cells as well. It is important to understand that a li-ion cell is compact container that contains flammable materials that under normal operations, converts chemical energy to electrical energy with minimal heat and gas. However, if allowed to react chemically, the chemical energy will convert directly to heat and gas and will continue to completion once it has begun. For a li-ion cell, safety is determined by reducing the probability of occurrence and lessening severity. The general goal of battery research is to increase capacity and voltage, as a result, designing safer battery cells becomes more challenging as energy density increases. So it is imperative that safety also be considered as materials are chosen and designs are made.

In order to protect batteries from abnormal conditions, several safety devices have already been implemented. Shutdown separators that come between anode and cathodes can prevent ionic conduction above higher internal temperatures to prevent charge and discharge. Cell vents can conduct the safe release of gas if internal pressures are too high. Current interrupt devices protect from over-current and stop internal electrical currents when internal pressure is too high. Positive temperature coefficient disks can be used to limit high currents. Current limiting fuses can be used to disrupt sustained discharge. Diodes can prevent inadvertent charge or discharge currents. Battery Management systems can control electrical distribution and protect from over and under voltage conditions.[22]

To evaluate battery materials, there have been many techniques to evaluate thermal response. Electrochemical characterization can provide baseline data of electrochemical stability, thermodynamic stability, and kinetic stability. Thermal characterization of individual materials and whole cells provide understanding of failure modes that can be used for improved abuse tolerant cells. While characterization provides a baseline for thermal conditions in a cell, they are not ideal for analyzing the effects of thermal abuse conditions in a cell. Differential Scanning Calorimetry(DSC) and Accelerating-Rate Calorimetry(ARC) are more common ways of analyzing these conditions. DSC allows for the thermal response of cell components and combinations of cell components to be measured over a wide temperature range with a fixed temperature rate. What this does is give qualitative data of the effects of local charge states of electrodes which is related to the cell thermal reactivity that leads to thermal runaway and cell self-discharge. However, DSC can only be applied to small sample sizes. ARC can be conducted on full cells and on cell components. ARC tests cells under adiabatic conditions so that there is precise control of temperature and the conditions are more uniform. This way, the cell heating rate is a function of the heat generating reactions in the cell. During testing, the reaction rate starts off slowly and the reaction rate increases until thermal runaway occurs. ARC can be used to find where the onset of self-heating occurs.[23]

While those techniques mentioned are for evaluation of batteries and their components, batteries have various failure modes from abusive conditions that lead to thermal runaway. Abuse tests are done to observe the behavior of batteries and to characterize the resistance of a cell to abuse and how self-heating and thermal runaway occurs in a cell. There are five widely used abuse tests that can be used: the oven test whereby a battery is exposed to a higher temperature, the short-circuit test where a low resistance is connected to the battery terminals, the overcharge test where current of a cell is forced past the cell’s limiting voltage, the nail test where a nail is forced through the battery at a set rate, and the crush test where a bar applies pressure onto the battery.

In oven tests and other thermal abuse tests, an external heat source raises the temperature of the cell from a beginning temperature to the onset temperature where self-heating starts. If this self-heating is not dissipated, the temperature will keep on rising due to exothermic reactions. Heat continues to increase at accelerating rates as these reactions occur, and is characterized by electrolyte reduction at the anode and electrolyte oxidation at the cathode until thermal runaway occurs between 130 ° C and 200 °C, depending on chemistry, where the temperature rises rapidly where flames and rapid disassembly may occur. Overcharge and discharge tests can be caused by problems with the control software and electronics that handle current in charging stations. A cell’s ability to withstand overcharge depends on the current applied and the chemistry of the cell. At low currents, overcharge results are benign but at high currents, cells would go through thermal runaway. While the cell response is complex, the thermal response is largely dependent on the chemistry of the cathode. Different cathode oxides have different levels of minimum lithium intercalation when a cell fully charged and overcharging can cause permanent structural changes by continuing to remove lithium. There is typically a rapid increase of heat generation when overcharging occurs as lithium is further removed from the cathode. [24]

In abuse tests that result in physical damage like the nail test or the crush test, they attempt to test the resistance to creating internal short circuits within the cell or within the battery pack to cause unexpected electronic flow. When unexpected deformation occur or the introduction of foreign objects, like in the nail test, occur, internal shorts happen but each test has nuances. The nail test allows for uniform discharge throughout the cell but heat generation is focused around the nail while also allowing electrolyte to react with air. The crush test is similar in that the cell is allowed to discharge in a uniform manner but heat is generated locally in the cell where the short would occur and can act similarly to short circuit tests. So while those tested for internal shorts, the short circuit test is where external short circuit abuse is tested. These are typically the most common types of abuse that batteries go through. The cell is connected to a circuit with an external resistance of around 1 mΩ and the current and cell temperature are recorded as well as other thermal responses that may occur. Thermal management of the cell usually determines whether or not the cell response will lead to thermal runaway or not as the thermal output is low.[24]

1.4 Electrode Microstructure

The field of Li-ion batteries is still fairly immature so it is crucial that development of every component undergoes rigorous studies of every composition, morphology, structure, surface chemistry and their effect on electrochemical performance, and thermal stability. Due to how important the cathode is in determining electrochemical and thermal performance, extensive research is needed to determine how each aspect of the cathode affects performance. For example, in large scale and vehicular use, there is a possible risk of fire. The conditions that lead to the critical temperatures that lead to thermal runaway needs to be studied. The cathode performance and stability, in particular, involves a strong interplay between material effects and electrode microstructure. Given a combination of materials for different phases of the cell, the system dynamics is a strong function of relative arrangements and effectiveness of species and charge transport. Variation in the formulation and manufacturing of electrode microstructure plays a large role in determining the porous media properties of the cathode which in turn play a large role in determining the electrochemical and thermal performance of a cell.[18]

When discussing porous media properties, it refers to the properties of a material containing pores like the porous cathode microstructure. Characterization of li-ion performance relies on three main porous media properties: tortuosity, active material surface area, and effective electronic conductivity. Tortuosity is the measurement of how tortuous something is or how curved a path is. Tortuosity is simply defined as the ratio of the length of a curve C vesus the distance between the endpoints L or:

$$\tau = \frac{C}{L}$$

Tortuosity is generally used to quantify ionic transport by giving simplified information on the movement of ions through available paths in the porous media. A $\tau = 1$, describes an ideal porous media while a $\tau > 1$ describes a porous body with obstructions.[25]

The active area of the electrode/electrolyte interface describes the surface area of the active material in the cathode that is in contact with porous space. This is important to measure because a cathode is made up of active material, binder, and conductive additive. However, the surface area of the active material will be partially covered by binder and conductive additive which then limits the area of the electrode that will be in contact with the electrolyte phase and inefficient utilization of active material phase. So the active area can be used to describe the amount of active material surface area available for lithium ion transfer through the electrolyte.

The effective electronic conductivity is the conductivity of the components of the electrode when taken as a whole. Active materials like NMC do not have very high electronic conductivities so the addition of a conductive additive like acetylene black or graphite is necessary to increase the electronic conductivity to reasonable values. Without the addition of conductive additive, low electronic conductivity can lead to inefficient charge and discharge. The measurement of effective electronic conductivity can provide details of the composite electrode material.[26]

1.5 Microstructure Properties

When measuring the active material fractions in regards to a layered transition oxides, the fractions are typically measured on a gravimetric basis. This is simpler to measure in the experimental phase but it is not as useful as a volumetric measurement. Ragone plots, as previously mentioned, can be useful in showing the relation between power density and energy density but they can also be somewhat misleading if they show a comparison on a gravimetric basis. In a complete system, this does not take into account the weight of other components of the device. While two devices could use the same graphite material as the anode, if one used an electrode that was 10 times thinner, the energy density would decrease by a factor of 3-4. On a gravimetric basis, the graphite materials would have the same energy density but on a volumetric basis, that is no longer the case. These devices could also show high gravimetric power densities but they don’t scale linearly with thickness. As a result, gravimetric active material density measurements are less important compared to the volumetric and areal measurements in electrodes when determining the performance of a cell [1]. However, it should be noted that batteries are typically are manufactured on a gravimetric basis as it is very difficult to adjust a cell’s volumetric and areal properties in a consistent manner.

So when it comes to discussing about the composition of a cathode, the composition will be noted in a weight ratio such as 75:15:10 where the first number is the active material weight percentage, the second number the conductive additive weight percentage, and the third number is the binder weight percentage or 75:25 where the first number is the active material and the second number the combination of the conductive additive and binder phase. These three numbers will add up to 100%. There is no standard composition ratio that gives the optimal results so it is currently up to research efforts to test and create experiments to investigate different compositions. Compositions can range anywhere from 60-90wt% active material and a corresponding conductive additive and binder composition of 10-40wt%. Cathodes will need conductive additives and binders for the foreseeable future which prevents the active material phase from ever being a homogeneous cathode with 100 wt% active material. One area of concern is that these numbers assume that the cathode is free of contaminants but that is not always the case. The possibility exists for the addition of metallic particle contaminants as well can cause unintended consequences in the development of the electrode.

However, when it comes to the microstructure, it is more useful to talk about the composition in volume percentages. This way, a corresponding volume ratio of the composition, which would need to be calculated, would be about 35.1:29.9. However, the volume percentages do not stay constant in the same way the weight percentages do. Each cathode microstructure for the same weight ratios will have slightly different volume ratios. Notice that the volume percentages do not add up 100% since it does not include the porosity. Cathodes are porous media that include porous in order to maximize the electrode/electrolyte interface. In a lithium ion cell, the porosity typically comes about to be about 35% of the volume of the cathode but it can be adjusted through manufacturing means. Changes in porosity can also lead to changes in the porous media properties as well.

Another thing that can change the microstructural properties are the particle sizes. The size of the particles of the active material, binder, and conductive additive can have an effect on the porosity, conductivity, and active material as well. Ideally, active material particles should be as small as possible to give the best results but in real world circumstances, manufacturing procedures can not always provide consistent particle sizes. Manufacturing defects such as particle agglomeration can be caused by improper mixing of the cathode slurry or deviations from slurry-feed rates. Whether it is deviation in the size of the active material particles or the binder and conductive additive particle size, it can lead to higher levels of inactive material to reduce the active area or tortuosity or conductivity. [27]

The variation in the size of the particle, porous space, and composition can cause a wide array of changes to the porous media properties. However, there isn't any expected differences between different layered transition oxides.(book) For many cases, layered transition oxides have similar microstructures that would result in similar properties but the electrochemical properties still differ. The only significant difference in regards to the microstructure is how changes in the electrochemical properties like the conductivity of the active material affects the effective conductivity of the overall cathode composition.

1.6 Objective

The intended goal of this research is to develop a guideline for electrode microstructures that can be used in future works to optimize choices in regards to electrode design depending on specific design criteria. To perform this study, a series of microstructures will be developed for the cathode and anode to examine how variation of porosity, composition, particle size, and other possible changes affect the porous media properties such as tortuosity, active area, and effective conductive. A correlation will be developed considering the particle size, the active material volume percentage, secondary phase volume percentage, and self-deposition ratio will be extracted from the microstructural properties. Then, a parametric study will be done to model how the change in these properties affect the electrochemical and thermal performance and rate capabilities of a lithium ion cell considering variation in various microstructural properties that occur in the anode and cathode. By incorporating these factors, it will be possible to find combinations of properties that can best optimize a cell in regards to performance, safety, longevity, or any other design goals.

2. LITERATURE REVIEW

This literature review will focus on various factors and parameters that can ultimately cause changes in the electrochemical and thermal interactions inside a lithium-ion cell. Factors include fundamental components like the choice of active material, binder, conductive additive, and electrolyte as well other electrode properties in processing that may affect thermal-electrochemical interactions as well.

2.1 Active Materials

An electrode is comprised primarily of the active material, the conductive additive, the current collector, and the binder. The main identifier of what kind of cell is being used is the active material. The active material is the chemically active component of the electrode and is what determines the electro-power capabilities, energy density, cycle life, cost, and safety. As active materials can have very different properties, determining the right active material for a particular application is an important consideration. [18]

The main type of active material used in cathodes are called intercalation cathode materials. These are types of cathodes that have a solid host network which can then store a guest ion that can be inserted and removed reversibly. There are a number of types of intercalation materials classified as metal chalcogenides, transition metal oxides, and polyanion compounds. They can also be divided based on their crystal structure as layered, spinel, olivine, or tavorite. However, not all of these materials are still used. Most research is done on transition metal oxides and polyanion compounds while metal chalcogenides have been mostly phased out.[28]

When it comes to transition metal oxides, $LiCoO_2$ (LCO) is the first and most successful active material used right now. It uses cobalt and lithium which are intercalated into octahedral sites in alternating layers. LCO has been popular because of its high theoretical specific capacity of 274 mAh g^{-1}, a high volumetric capacity of 1363 mAh cm^{-3}, low self-discharg, high discharge voltage, and good cycling performance.[29] However, LCO is limited due to the high cost of cobalt, low thermal stability from the release of oxygen of lithium metal oxides when exothermic reactions occur at relatively low temperatures of 200 °C that will result in thermal runaway. LCO also suffers from high capacity fade from high current rates and deep cycling that causes lattice distortions that affect the structure of the intercalation sites.

Since then, research has been done of other types of transition metal oxides. $LiNiO_2$ (LNO) is similar to LCO and had a similar specific capacity of 275 mAh g^{-1} but is also cheaper as the cost of Ni is lower than the cost of Co. However LNO has a problem where Ni^{2+}would calate into Li^+ sites during synthesis and delithiation and block Li transport as a result. LNO was also more unstable than LCO as well. It was possible to improve the thermal stability and electrochemical performance by doping it with either Mg or Al. Additionally, well-ordered LNO is difficult to manufacture. This would lead to the development of $LiNi_{0.8}Co_{0.15}Al_{0.05}O_2$ (NCA). In this way, Ni is substituted in place of Co to reduce costs while the addition of Al improves the ordering of Li. [18] NCA is known for its high discharge capacity and long storage life, especially compared to LCO but it suffers from capacity fade in warmer temperatures between 40-70 °C.

LiMnO$_2$ (LMO) was another material developed as a result. The benefit of using manganese is that it is less expensive and less toxic than Co or Ni. However, the cycling performance of LMO is not very good due the the layer structure changing to a spinel structure during Li extraction and Mn has been seen to dissolve into the electrolyte as a result of cycling. This results in a relatively short life span.[30] With the previous research done, efforts to decrease the cost of LCO lead to the formulation of Li(Ni$_{0.5}$Mn$_{0.5}$)O$_2$ (NMO). NMO has similar properties to LCO but at a reduced cost due to the use of cheaper materials. Using Ni allows for better Li extraction that allowed for higher reversible capacities of 200 mAh g^{-1} but the poor ordering lead to low Li diffusivity and poor rate capabilities.

Which then ultimately leads to the development of LiNixCoyMnzO2 (NMC). The important thing about this chemistry is that the presence of Co to NMO improved the defects of Ni in the Li layer which would then improve the rate capabilities and Li diffusion that were problematic in the NMO chemistry. NMC has a high reversible capacity of 234 mAh g^{-1}, and a voltage window of 3.6-4.7V. However, the cycle life, specific charge, and safety qualities depend on the upper cut-off potential.[31] Good thermal stability has also been observed as up to 80% of the cell capacity could be retained even at 55 °C. [32] It is also quite versatile in its ability to provide either a high amount of power or a large energy capacity but it isn’t capable of both. In the mean time, challenges involving material stabilization during prolonged cycling and improving rate capabilities and safety still exist. However, the capabilities of NMC along with a large energy density makes NMC-based cells one of the more promising and enticing active material chemistries going forward. Futhermore, for these reasons NMC will be the focus in this thesis.

Another active material of interest is $LiFePO_4$ (LFP) which is classified as a polyanion compound and consists of an olivine structure. Li^+ and Fe^{2+} LFP cells are known for their thermal stability and excellent cycling capabilities while also being inexpensive and environmentally friendly. However, the downside to LFP is that they have low average potential and conductivities that also result in a lower average capacity at 165 mAh g^{-1} [31]. Regardless of that, LFP is a promising active material that is being heavily-researched.

2.2 Binders

As previously mentioned, the binder is one of the components in an electrode. It typically only makes up for a small part of the composition but can be an important part that affects cycling stability and rate capability. Poly(vinylidene difluoride) (PVDF) is the most widely used binder of choice in most mainstream Li-ion cells due to its electrochemical stability and ability to absorb electrolyte for Li transport. Unfortunately, PVDF manufacturing relies on toxic and expensive organic solvents. Research into aqueous binders have begun to replace PVDF due to aqueous binders having low costs, being better for the environment, better active material to binder ratio, and simpler and faster manufacturing. [33] For NMC based cathodes, research has been on typical binders like PVDF as well as explorations into the use of aqueous binders such as carboxylmethyl cellulose (CMC), alginate from brown algae, and fluorine acrylic hybrid latex (TRD 202A).

Binders are electrochemically inactive substances but they can have a significant influence on performance. PVDF is a popular choice in commercial cells due to their good electrochemical stability and adhesion to electrodes and current collectors but they are expensive and not environmentally friendly. Xu, et. al., have explored aqueous substitutes like CMC and alginate that are cheaper and safer than PVDF. CMC is produced from the insertion of carboxymethyl groups into cellulose and dissolves easily into water and is much cheaper than PVDF and has shown good cycling stability and electrochemical capacity improvements. Alginate is another cheap and naturally occurring polysaccharide that has also shown impressive capacity and cycling abilities. Their results show that PVDF and alginate had better discharge capacities than CMC did at 0.1C, CMC had better capacities and rate performance overall. At 5C, the capacity of CMC was much better than PVDF and alginate. The CMC binder also showed the best cycling capabilities as well with better capacity retention and rate performance than the alginate and PVDF. Xu also investigated charge transfer resistances and activation energy which showed that CMC had lower values than PVDF and alginate which leads to better mass transport of lithium ions.[34]

Another aqueous binder known as TRD 202A has also been looked into as a substitute for PVDF as well. Wu, et. al., used TRD 202A to determine its capabilities as a binder for LMR-NMC which is a lithium manganese rich variation of NMC. Like, Xu’s CMC results, the TRD 202A showed equivalent or better performance. TRD 202A had high specific capacity, low impedance, good rate capability and good capacity retention. [35] Notably, TRD 202A rate capability and specific capacity were better than CMC when comparing discharge curves at similar C-rates.

Research has continued on CMC by groups like Doberdo, et. al, [36] and Loeffler, et. al, [37] to improve and prevent some of the problems involved with the use of aqueous binders. Doberdo identified that the use of CMC as the binder and water as the solvent for NMC electrodes causes an increase in pH level of the slurry. However, aluminum, which is the typical current collector used for cathodes, is not chemically stable at high pH levels like this and can lead to aluminum corrosion. To mitigate this effect, they coated the current collector surface with a thin 5 μm of carbon to preserve the current collector surface. This will prevent direct contact between the alkaline NMC and the aluminum to prevent corrosion. In addition to preventing corrosion, it was found that the carbon coating improves the interface between the foil and cathode layer resulting in a decrease in charge transfer impedance. Loeffler continued from the results by Doberdo to improve manufacturing of CMC based electrodes and found that the binder was thermally stable at temperatures as high as 200 °C and electrochemically stable from 0.02V to 5.00V. Additionally, compression of CMC-based cathodes would improve cycling performance due to the effect it would have on surface morphology of the electrodes. While PVDF is the mainstream binder used in NMC-based cathodes, CMC proves to be a promising substitute in the future.

2.3 Conductive Additive

The carbon additive is an important part of the cathode as it plays a role in the electrical resistivity, ionic resitivity, and density of the electrode. While the conductive additive is only present in small weight percentages, it plays an important role in the electrode. The conductive additive combines with the binder used and results in a conductive polymer that connects the active material particles. While conductive additives do not play a role in the electrochemical process, they are needed to lower the cell resistance as active material particles typically have very low conductivities. The addition of conductive carbons is needed to increase the power density of a cell but it is necessary to keep the amount of additive low so that the volume fraction of conductive additive to active material stays as low as possible to optimize for the energy density as well. There is a critical volume fraction where the volume fraction of the conductive additive needs to be increased to before the electrode resistivity decreases otherwise the resistivity stays at a high constant level. However, there is also an ultimate resistivity level where further addition makes no change to the resistivity. These two factors are used to determine the quality of conductive additives. Additionally, the surface area, morphology, compaction behavior, and the processing of conductive additives are also important factors that affect the impact of conductive additives in electrodes.[38]

Conductive carbons are often used as the conductive additive in electrodes and specifically carbon blacks are common. In work done by Chen, et. al., they found that the use of carbon black and PVDF led to better overall conductivity than the use of other conductors like graphite. [39] Which affirms the reason for using carbon blacks like acetylene black, Super S, and Super P which are commonly used in electrode manufacturing.

2.4 Electrolyte

There have not been many changes in the electrolyte as compared to other components in electrode research. For the most part, lithium hexafluorophosphate ($LiPF_6$) salt with organic carbonate solvents has been the main electrolyte in Li-ion batteries. The reason for this is that electrolyte components, and the solvents are particularly sensitive to operating potentials rather than electrode capacity. So as long as new cathode chemistries perform in the typical window of operations, major changes are not needed. Another reason is that electrolyte additives became more common in their use with the knowledge of solid electrolyte interphase (SEI) formation on electrode surfaces. Using additives as consumable components during SEI formation allows for the $LiPF_6$ formulation to remain relatively unchanged. The last reason is mainly economics as the supply chain is reluctant to change unless there is a significant benefit. [40]

While $LiPF_6$ is the main salt used in electrolytes due to their well-balanced properties, it does have some disadvantages in its thermal and chemical stability. Other phosphate and borate salts have been explored like LiTFOP, $LiBF_4$, or LiBOB. However, the problem with these developments has been that they could improve on the problems of $LiPF_6$, but this typically result in a tradeoff and result in worse results in another category. In one case, LiBOB is more stable at higher temperatures but is only electrochemically stable up to 4.2V where as $LiPF_6$ is 4.5V. [41]

The main formulation of $LiPF_6$ in ester solvents is the typical electrolyte used. The criteria for a good solvent for $LiPF_6$ requires a high dielectric permittivity and low viscosity while being stable with both the anode and cathode, however there is no one solvent that meet these requirements. However, solvents that have high dielectric permittivity and a low viscosity can be mixed. This leads to the common solution of ethylene carbonate (EC), for dielectric permittivity, and one of dimethyl carbonate DMC), diethyl carbonate (DEC), and ethylmethyl carbonate (EMC) to lower the viscosity.[42]

It is also worth mentioning some of the more notable electrolyte additives in use as well. Work done by Wang, et. al., peformed a systematic study of vinylene carbonate (VC) and prop-1-ene-1,3 sultone (PES), as well as blends of each including ethylene sulfate (DTD), trimethylene sulfate (TMS), ethylene sulfite (ES), and sulfur containing additives like methylene methane disulfonate (MMDS), tris(-trimethyl-silyl)-phosphate (TTSP), and tris(-trimethyl-silyl)-phosphite (TTSPi). The choice to use these additives were based on the positives results shown from previous studies and is representative of promising additives currently used. [40] They used a “figure of merit” approach to rank the effectiveness of these additives’ abilities to maximize cell life and minimize impedance. Their results showed 2% VC is a good baseline to compare results and if an additive does not show better performance over 2%VC then it is unlikely to have any benefits. It was found that using an $LiPF_6$ electrolyte with additive blends using VC or PES as a base with additional MMDS, ES or DTD, and TTSP or TTSPi would give NMC/graphite cells excellent performances. Their work shows that these blends can improve cycling life and improve electrochemical performance over all temperature ranges. However, the reason why could not be determined and the distinguishing the "best" is also a daunting task.[43]

2.5 Electrode Thickness And Material Loading

Developing thicker electrodes has been researched in recent years to decrease the stack assembly time as well as a way to increase capacity available in an electrode. An electrode's specific energy and specific power, in terms of weight and volume, have been important concerns when designing electrodes. The electrode thickness and porosity have a substantial effect on a cell's electrochemical capabilities. Increasing electrode thickness can improve the energy density by decreasing the ratio of inactive materials compared to typical electrodes. However, increase in the electrode thickness results in drawbacks like decreased lithium ion diffusion within electrodes due to increasing complexity in mass transport. There are also concerns in manufacturing that thicker elecrodes can decrease the mechanical stability of the cell as well.

Work has been done by a few groups to optimize and explain the effects on mass transport in recent years. Marks et al, did some work in determining the effect of electode densities and thicknesses. They tested cells with 26% porosities that were similar to commercial electrodes and had to make certain that the electrolyte could penetrate the electrode. With the increase of binder content, it becomes more likely that the porosity would be closed and the electrolyte can't penetrate the electrode. They also determined that the necessary amount of solvent needed for the slurry was proportional to the surface area of the carbon and active material used. Finally, they found that compression would improve the adhesion of thicker electrodes. [44]

Zheng, et al. also worked to understand the effect of electrode thickness in cathodes. In their study, they did a comparative study of electrode thicknesses in NMC and LFP cathodes as NMC offers a high energy and power density while LFP have good safety and cycling characteristics. The main focus was the rate capability and long term cycling with regards to electrode thickness. Electrode thicknesses between 24 μm and 104 μm were tested for NMC electrodes. They found a power-law relation between the material loading and the maximum working C-rate and a correlation between electrode thickness and rate capability, energy density, power density, and long-term cycling. Increasing the electrode thickness resulted in significant changes in rate capability, cycling, and energy densities. The rate capability losses were attributed due to decreased Li-ion diffusion within the electrode. There was also an increase of internal resistance but it was not attributed as a main cause for significant capacity loss. As expected, energy density in the electrode also increased as electrode thickness was increased. However, the power density decreased as well. They also found that cycling capabilities suffered with increased electrode thickness and there was a higher capacity fade as a result. This capacity fade was attributed to severe polarization and poor mechanical stability in the electrode. [45]

Research done by Singh, et. al., compares the electrochemical performance of thick and thin electrodes. They used NMC cathodes with carbon black and PVDF, and SMG-A graphite anode. Then the electrodes were calendered to reduce the thickness. They compared 70 μm and 320 μm electrodes in half cell and full cell configurations. Commercial cells have a porosity of 30% but they increased the porosity to 40% in their thick electrodes so that good ionic contact and high lithium ion transport could be maintained. Their results showed that at low C-rates, there is a large increase in capacity between the thin and thick electrodes at C/10 from 337 Wh/L to about 412 Wh/L respectively which shows an increase of 19% with the use of thicker electrodes However, for the thick electrode, there is significant decrease in capacity as the C-rate increases to C/2 where the thick electrode has a drop in capacity to by about 50% which was much more significant than the decrease in the thinner electrode. The significant decrease in capacity in the thick electrode may be attributed to poor mass transport and kinetics but the large capacity may be applicable for certain applications that need large capacity and low C-rates. There were also severe aging mechanisms observed that was attributed to lithium plating during charge. [46]

In further research Singh, et. al., worked to improve the lithium ion cells with the thick electrodes by introducing carbon fibers to improve the mechanical stability while also acting as electron conductors and work to enhance the porosity. They did a systematic comparison electrodes from 250 μm to 350 μm and porosities ranging from 48%-58% for anodes and 38%-44% for cathodes. The introduction of carbon fibers increased the mechanical integrity of the electrodes that were previously prone to disintegration with low calendaring. These cells could then reach energy densities of 189 Wh/kg and 441 Wh/L which shows improvement from their previous work. Compression improved the contact between particles which could provide a continuous network. Furthermore, increasing the porosity above 50% in the anode and 40% in the cathode showed no improvement in cell performance. As a whole, most studies continue to work towards improved cycling and better performance at higher C-rates but the mass transport and mechanical stability continues to be concern. [47]

2.6 Side Reactions

2.6.1 SEI Formation

The solid electrolyte interface (SEI) layer serves as a protective layer that prevents the anode material, typically a carbon species, from further reactions with the electrons and electrolyte. The SEI layer is formed during the first few charge-discharge cycles which is referred to as formation cycling. Formation cycling is what the first several charge-discharge cycles are called during which the electrolyte reacts with the anode active material at reducing potentials. [48]The morphology and composition of the SEI layer depends on a multitude of factors like the charge-discharge process, the anode active material, the electrolyte additives, and the wetting of the electrode. The quality of the SEI layer affects cell performance, irreversible charge loss, rate capability, cyclability, and safety of a cell. So the ideal result should be an SEI layer that simultaneously resistant electrically and ionically conductive however some factors like the wetting process is a time consuming and practically difficult process. [49]

However, there are problems with the decomposition of the SEI layer during cycling. The initial formation cycling results in a large initial capacity loss due to the consumption of electrolyte, which is dependent on the specific surface area of the graphite. [50] This can continue to be a problem during cycling. While the SEI layer is supposed to be ionically conductive for the transport of Li^+ from the cathode, it will also allow other charged and neutral species through as well. These species may be solvated lithium cations from the electrolyte or other components from the electrolyte. This results in corrosion of the anode active material as well as further electrolyte decomposition which then causes further SEI formation. The regions where the electrode faces corrosion will also be penetrated by SEI which can decrease the active surface area of anode. This continued formation of SEI formation can be considered one of the negative ageing mechanisms in Li-ion cells that result in capacity fade over time. The effects are often more pronounced at elevated temperatures as well. [51]

2.6.2 Lithium Plating

Lithium plating is when the amount of lithium in the cathode exceeds the amount of lithium that can be intercalated in the anode. To prevent this from happening, anodes are generally designed to have excess capacity so that intercalation sites do not run out. If lithium plating does occur, metallic lithium will deposit itself on the anode which can lead to reliability and safety concerns. The odds of Li plating occurring is strongly related to the cell design parameters. Anode materials with high reversible potentials are unlikely to suffer from plating but materials with reversible potential closer to the lithium deposition potential is more likely to suffer from lithium plating. While the electrode capacities are designed so that the anode intercalation sites are in excess, kinetic reasons like slower Li intercalation can lead to underutilization of the anode which contributes to Li plating. Most occurrences of lithium plating is reversible but a small amount ends up becoming irreversibly plated and this small amount on the graphite is unstable and reactions with the graphite may occur.[52]

Slower kinetics and transport of Li can be attributed to the electrolyte as studied by Smart and Ratnakumar. The nature of the electrolyte and anode, as well as the operating conditions like low temperatures, high charge rate and high voltage can increase the chances of Li plating. Smart and Ratnakumar also found that Li plating would lead to degradation of the anode/electrolyte interface as lithium is reactive to the electrolyte. This degradation of the interface will serve as a problem in degrading the performance, reliability, and safety of Li-ion cells. One reason may be from the presence of dendrite formation that can occur alongside lithium plating. Since poor Li kinetics are one of the reasons for lithium plating, and Li kinetics are dictated by the SEI layer, then the choice of electrolyte may serve to prevent Li plating. They found that the formation of a sturdy SEI layer via the use of high-EC electrolytes may impede lithium intercalation at low temperatures and cause lithium plating.[53]

Identification of lithium plating can serve to protect the cell and prevent inefficiencies and capacity fade. Some in situ methods of identification are being researched to identify the occurrence of Li plating in progress such as identifying the change in cell thickness during cycling as lithium plating increases the volume[54], or by measuring the heat flow as there are unique thermal heat flow signatures at the onset of lithium plating[55]. These methods could be adapted to larger scales such as in automobiles to better optimize performance and to prevent accidents.

3. MICROSTRUCTURE GENERATION

For this research, an NMC/graphite full cell is selected as it is a commonly focused on cell with good potential. The cathode uses NMC as the active material, PVDF as the binder, and a carbon black known as acetylene black as the conductive additive. For the anode, the active material will be graphite and the binder will be PVDF. This set of electrode components was chosen because of their prevalent use in mainstream li-ion electrode manufacturing.

3.1 Electrode Microstructure

For the purposes of this research, stochastic microstructure generation is used to generate a structure representing the active material phase and how NMC or graphite is present within the structure. There are several parameters that can be changed when generating the active material microstructure: the shape and size of the particle, the volume fraction of the active material, the box length, and the voxel size. Figure 3 shows an example of the completed microstructure and the separated active material structure and secondary phase deposition. The secondary phase refers to the PVDF/carbon black composite, which will be referred to as the secondary phase, that is deposited to the active material microstructure. As shown in Figure 3, the active material structure is composed of larger red particles that represent the active material while the secondary phase is made up of very fine green particles that represent the PVDF/carbon black composite.

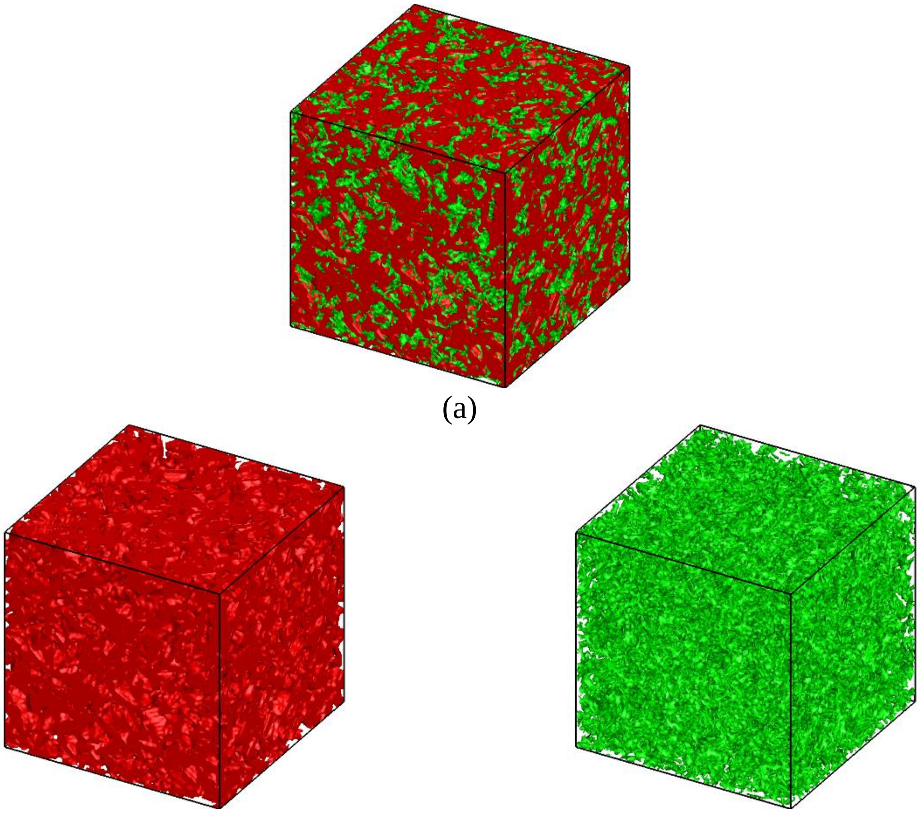

(a)

(b) (c)

Figure 3. (a) Completed Microstructure, (b) Active Material phase, (c) Secondary Phase

The shape of the particles used for the anode and cathode were platelets and spheres respectively. The shapes chosen are good approximations of the appearance of the particles in real world applications. While actual NMC and graphite particles will have manufacturing variance, the stochastic generation can provide an average that will approximate the active material microstructure on the basis that the average distribution of the actual particles center around the size of the particle chosen.

The active material volume percentage is the percentage of the active material that is present in the specified volume being investigated. Various microstructures are generated with increasing volume fraction values to reflect a range of possible real world scenarios.

The voxel size refers to the size of the voxel. The voxel is the smallest sampled volume element in 3D space. Similar to how a pixel is the smallest element measured in 2D space. The smaller the voxel size, the more detailed the representation will be. The voxel size needs to be small enough so that the microstructure representation can be as precise as possible. However, too small of a voxel size can be unnecessary.

The box length is the length of each side of the examined control volume. This determines the volume of the sample of the microstructure that will be investigated. A larger box length and volume results in a larger sample size that is more likely to give results that are more accurate and representative of the properties of the electrode microstructures.

Voxel size and box length can have a large effect on results as these two properties affect the precision and accuracy of the studied region. Therefore, the determination of appropriate values for voxel size and box length will be discussed further in the statistical analysis portion.

Once the secondary phase is added, the microstructure will include both the active material and the secondary phase to act as a complete electrode. The secondary phase is added to the active material structure stochastically. The method by which the secondary phase deposits onto the active material structure first identifies locations on the active material that qualify for deposition at a certain rate and continues until the stopping criteria, which is when the desired secondary phase volume percentage is reached.

The amount of secondary phase addition will correspond to four factors: the desired active material vol%, the desired porous vol%, the desired secondary phase vol%, and the morphological weight factor. The volume percentages of each material phases are joined properties. The goal is a desired porous volume fraction and to achieve this, a certain amount of secondary phase volume fraction will be input to the active material phase volume fraction as required. The morphological weight factor does not affect the volume fractions. It is a way to identify the likelihood that deposition will occur on or near previously deposited sites. As previously mentioned, locations on the active material structure will be identified for secondary phase deposition and once a certain number of deposition occurs, the cycle will begin again and the code will determine once again sites for deposition. An energy value is assigned to each site according to what its neighboring particles are and the cumulative energy density of all the sites is taken. This cumulative energy landscape is then used to determine which sites qualify for deposition. What the morphological weight factor does is that it makes locations that were previously deposited on more likely to be qualified candidates for deposition.

The determining factor for the amount of secondary phase addition that will be applied to each microstructure depends on the porosity that is desired. Commercial electrodes typically have a porosity of ~30 vol% so the porosity range used will account for porous volumes along those lines. For the anode, the desired porosities range from 25 vol% to 40 vol% with increasing steps of 5 vol%. For the cathode, the desired porosity range is from 15 vol% to 35 vol% with increasing steps of 5 vol%. With the previously mentioned volume percentage range of the active materials, this will result in the secondary phase addition ranging from 0 vol% to 40 vol% with increasing steps of 10 vol%. The use of 0 vol% shows the properties of a bare active material structure and the electrochemical importance of the secondary phase addition.

3.2 Effective Property Calculations

The purpose of generating these microstructures is to determine the porous electrode properties of the cathode and electrode. The properties are determined after the secondary phase addition for each microstructure. In this stage, three properties are measured: the effective conductivity of the structure in the x, y, and z direction, the effective tortuosity in the x, y, and z direction, and the specific active area between the active material, the secondary phase, and the porous volume.

The specific surface area is found by counting the number of faces that each phase has in common with each other. These faces are defined as the surfaces of the voxels of the primary structures and the secondary phase structure. The following formula is used to calculate the specific active area:

$$a_{jk} = \frac{f * N_{jk}}{M_x M_y M_z (\frac{\Delta}{R})}$$

This formula calculates the specific surface area for phases ‘j’ and ‘k’. Depending on which phase is assigned to ‘j’ or ‘k’, the active area between any combination of the active material, porous space, or secondary phase can be found. Where f is the surface area of the faces, N_{jk} is the number of voxel faces, M_x, M_y, and M_z is the REV volume, and $\frac{\Delta}{R}$ is the voxel size. The values found here are dimensionless numbers that can be scaled up or down depending on the size of the actual particles used.

The effective conductivity and tortuosity are found using direct numerical simulation calculations with Dirichlet boundary conditions. The tortuosity is modeled using,

$$\nabla \bullet (D \nabla C) = 0$$

$$D(\vec{x}) = \begin{Bmatrix} 1 \text{ if } \vec{x} \in \text{ Pore} \\ 0 \text{ if } \vec{x} \in \text{ Solid} \end{Bmatrix}$$

$$J = -D \frac{\varepsilon}{\tau_n} \frac{\partial c}{\partial n}$$

The following boundary conditions are applied to the tortuosity equations.

$$c(0, y, z) = c_{left} \text{ and } c(L, y, z) = c_{right}$$

$$\frac{\partial c}{\partial n} = 0 \text{ (for every other face)}$$

Similarly, the conductivity is modeled with,

$$\nabla \bullet (\sigma \nabla \phi) = 0$$

$$\sigma(\vec{x}) = \begin{Bmatrix} \sigma_{AM} \text{ if } \vec{x} \in \text{ AM} \\ \sigma_{CA+B} \text{ if } \vec{x} \in \text{ CA+B} \\ 0 \text{ if } \vec{x} \in \text{ Pore} \end{Bmatrix}$$

$$J = -\sigma_n \frac{\partial \phi}{\partial n}$$

With boundary conditions,

$$\phi(0,y,z)=\phi_{left} \text{ and } c(L,y,z)=\phi_{right}$$
$$\frac{\partial\phi}{\partial n}=0 \text{ (for every other face)}$$

Values are assigned to each phase according to their respective tortuosity values or conductivity values with the aid of a coefficient matrix that identifies the right phases. Once each phase is identified, the tortuosity and conductivity is solved along each coordinate axis in order of x, y, then z.

3.3 Statistical Analysis

First, a statistical study needs to be done to confirm that the active material structures and the composite structures with the secondary phase addition result in porous media properties that are representative of both the structure and of the secondary phase addition. The statistical analysis is also needed to determine the appropriate voxel size and box length that can give accurate results. Five statistical studies were performed: 1) voxel size analysis, 2) representative elementary volume (REV) analysis, 3) active material generation analysis, 4) simultaneous deposition analysis, 5) secondary phase addition analysis.

As previously mentioned, an analysis needs to be done to determine what voxel size and REV are representative sizes for the microstructure. The voxel size and REV analyses are necessary to do as a large enough REV is needed for a representative sample size while also having a small enough voxel size so that the results are precise.

This also needs to be coupled with computational speed as well. It is possible to have an unnecessarily large sample size or too fine a voxel size that will slow down the performance of the system without being needed. So, the analyses is done to recognize the point where the voxel size analysis and REV analysis are performed to determine the point where the values of effective tortuosity, effective conductivity, and specific active area begin to converge. Once the representative sample volume is determined, the active material generation analysis is performed where the same active material microstructure is stochastically generated several times. to confirm that the Geodict constructs will yield results within a margin of error.

Once a representative volume for the Geodict structures are determined, the next step in the statistical study is to analyze the results of the secondary phase addition. Similar to how the voxel size and REV analyses were done, an analysis on the simultaneous depositions needs to be done. As it was mentioned in the section about the secondary phase addition above, the simultaneous deposition is the number of sites that deposition will occur in each cycle. If too many depositions occur at once, there can be errors in the results. In the opposite situation, too few depositions will cause unnecessary performance hurdles. Once the right number of depositions per cycle is determined, the same secondary phase addition is run multiple times to confirm the repeatability of the process.

The first statistical analysis done was based on the voxel size of the structure. This refers to the size of the voxels in the box structure. The voxel size-to-particle radius ratio $\frac{R}{\Delta}$ was increased from 2 to 16, while keeping the box length-to-particle radius ratio constant. Using ratios allows for these properties to apply regardless of what the particle size actually is. The purpose of this statistical analysis is to determine the best voxel size to use in the microstructural generation. A larger voxel size increases the performance speed as the results are less fine but a smaller voxel gives a better resolution and more accurate image of the structure. This study is meant to find the best voxel size and structural resolution without sacrificing time and performance.

In Figure 4, it shows the structures used for the statistical analysis. Seven different voxel sizes ranging from $\frac{R}{\Delta}$ = 2 to 16 were looked at to determine the voxel length that should be used. The lowest ratio in Figure 4a has the highest density and Figure 4g has the lowest density. The porosity, active material volume, and secondary volume were set to 25 vol%, 55 vol%, and 20 vol% respectively. This is done to ensure that the independent variable in the set is the voxel size. As Table 1 shows, the variation in the properties decreases as the voxel size increases, most notably in the conductivity. However, the tortuosity and active area appears to increase exponentially as voxel ratio decreases. Since the conductivity and tortuosity appears to show stable results with a voxel ratio of 10, that will be the voxel size used.

The second statistical analysis that was performed was on the box length to determine the representative elementary volume (REV). The REV is the smallest volume needed for a measurement to be considered representative of a whole structure. If the structure is bigger than the REV, then the amount of unnecessary calculations done increases and the time needed for the calculations increase. If the structure is too small, then the volume can not be considered representative. With a proper REV, the properties extracted from the volumes can be considered as average values typical of the microstructure. With the right REV, the results from the measurements should be stable and consistent. In this analysis, the box length-to particle radius ratio ranged from 8 to 16 with incremental increases of 2.

Table 1. Effect of voxel size-to-particle ratio on microstructure properties

R/Δ Ratio	Porous vol%	Active Material vol%	Secondary Vol%	01 area	Tortuosity	Conductivity
2	24.3321	54.9998	20.6678	115.6798221	541.4528827	0.217613333
4	24.3703	54.9998	20.6296	22.76018075	121.57357	0.238078667
8	24.4544	55.0003	20.545	2.86395355	23.38611733	0.278202
10	24.5158	55.0049	20.479	1.330511016	16.60377533	0.282372667
12	24.568	55.0046	20.4271	0.725292865	14.76538367	0.285342
14	24.6103	55.0133	20.3761	0.401251869	11.93299333	0.289361
16	24.657	55.005	20.3377	0.251499743	13.55840767	0.289462667

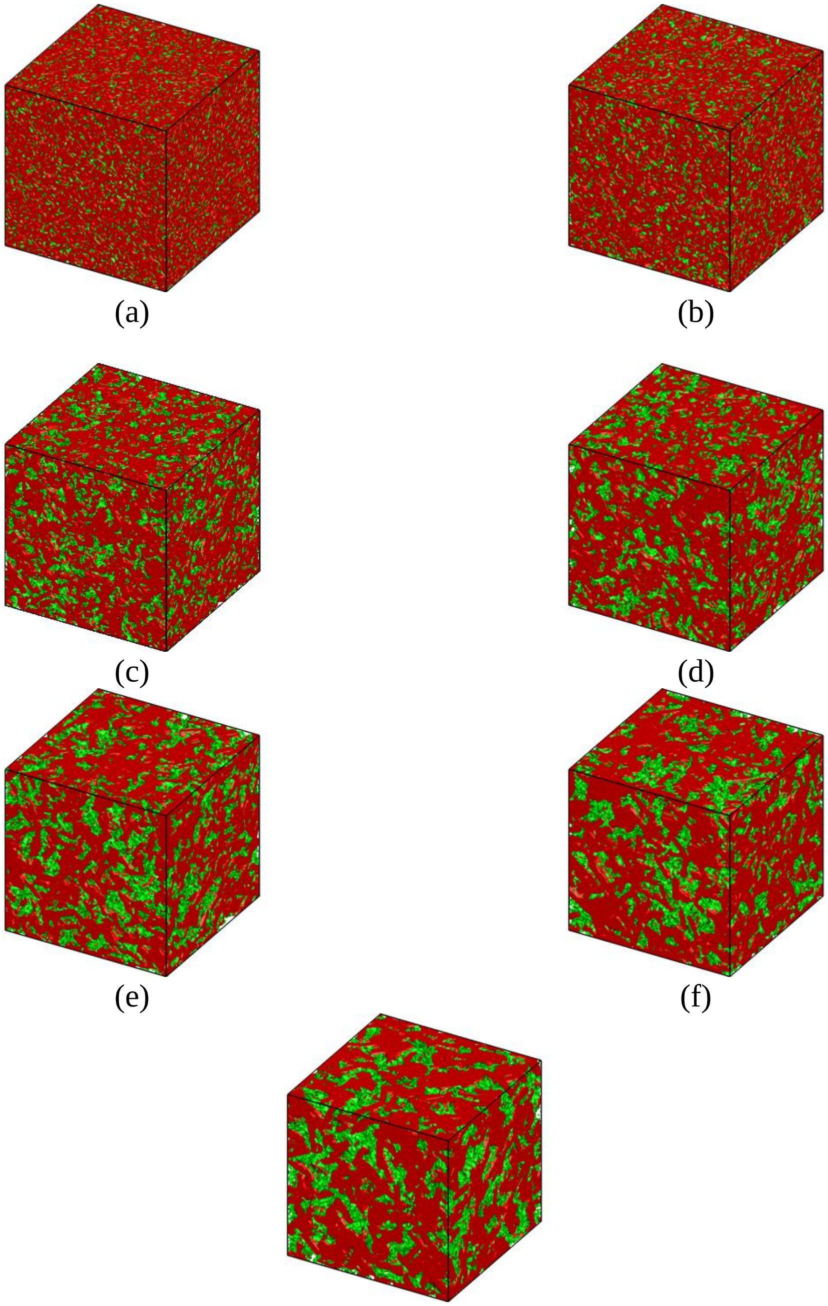

(a) (b) (c) (d) (e) (f) (g)

Figure 4. Microstructures with increasing $\frac{R}{\Delta}$ = (a) 2, (b) 4, (c) 8, (d) 10, (e) 12, (f) 14, (g) 16

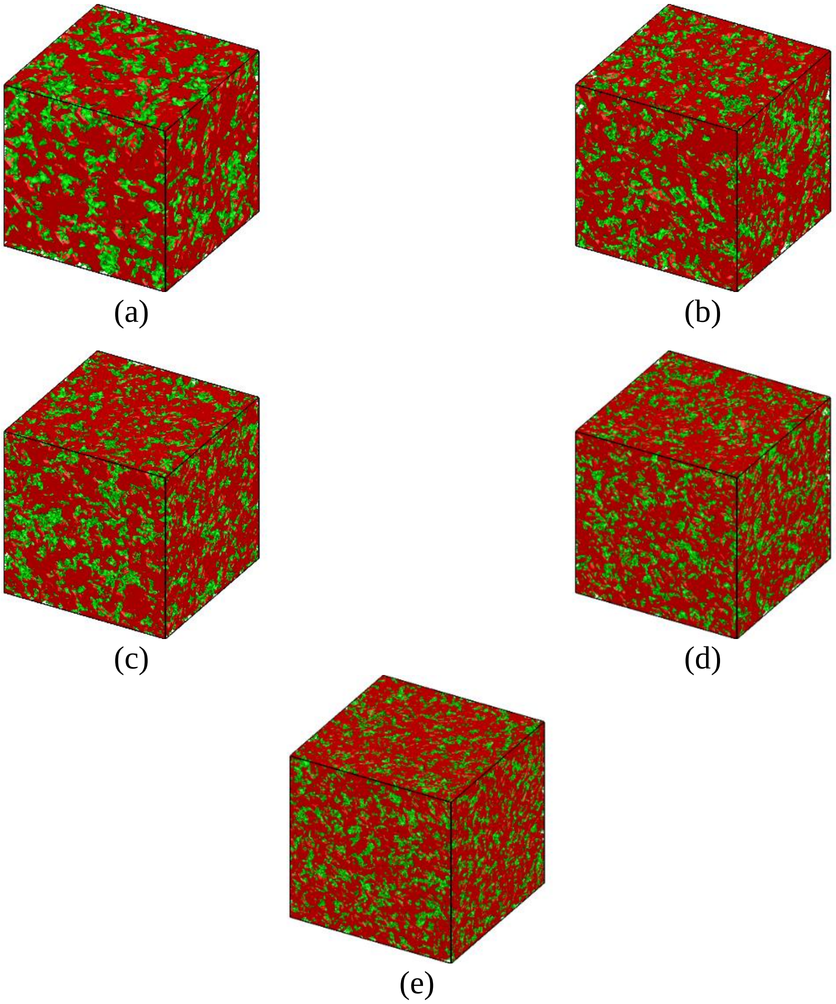

Figure 5. Microstructures with increasing $\frac{L}{R}$ = (a) 8, (b) 10, (c) 12, (d) 14, (e) 16

Table 2. Effect of box length-to-particle ratio on microstructure properties

L/R Ratio	Porous vol%	Active Material vol%	Secondary Vol%	01 area	Tortuosity	Conductivity
8	24.49707	55.004297	20.498047	1.352427143	19.67457667	0.284557333
10	24.5141	55.0049	20.4807	1.335714944	17.83843867	0.282074333
12	24.518692	55.000347	20.480787	1.348664658	16.99947767	0.286154333
14	24.524672	55.000219	20.475	1.368693522	16.849639	0.285189
16	24.514331	55.002368	20.483228	1.36132709	16.93468733	0.287226

In Figure 5, it shows the different volumes used to determine the correct REV. The density of the cells are all the same but Figure 5a has the smallest volume while Figure 5e has the largest volume and holds the largest sample of the microstructure composition. Since the volume is cubic, the parameter that will be changed is the box length. The box length-to-particle ratio $\frac{L}{R}$ increases from 8 to 16 with increments of 2 while using the previously determined voxel ratio of 10. From Table 2, the active area and conductivity are stable throughout but the tortuosity begins to stabilize only once the box length size increases. For the purpose of time, the box length used was determined to be $\frac{L}{R}$=10. The tortuosity at $\frac{L}{R}$=10 has not completely stabilized but the margin of error was determined to be negligible.

The third statistical analysis was repeated generations of the active material microstructure. In this analysis, we used the results from the first two statistical analyses and use a voxel size of 10 μm and a box length of 100 μm, which gave a good REV and resolution. The purpose of generating the same structure multiple times is to confirm that the REV is representative and that the same active material microstructure generation will not vary wildly from structure to structure.

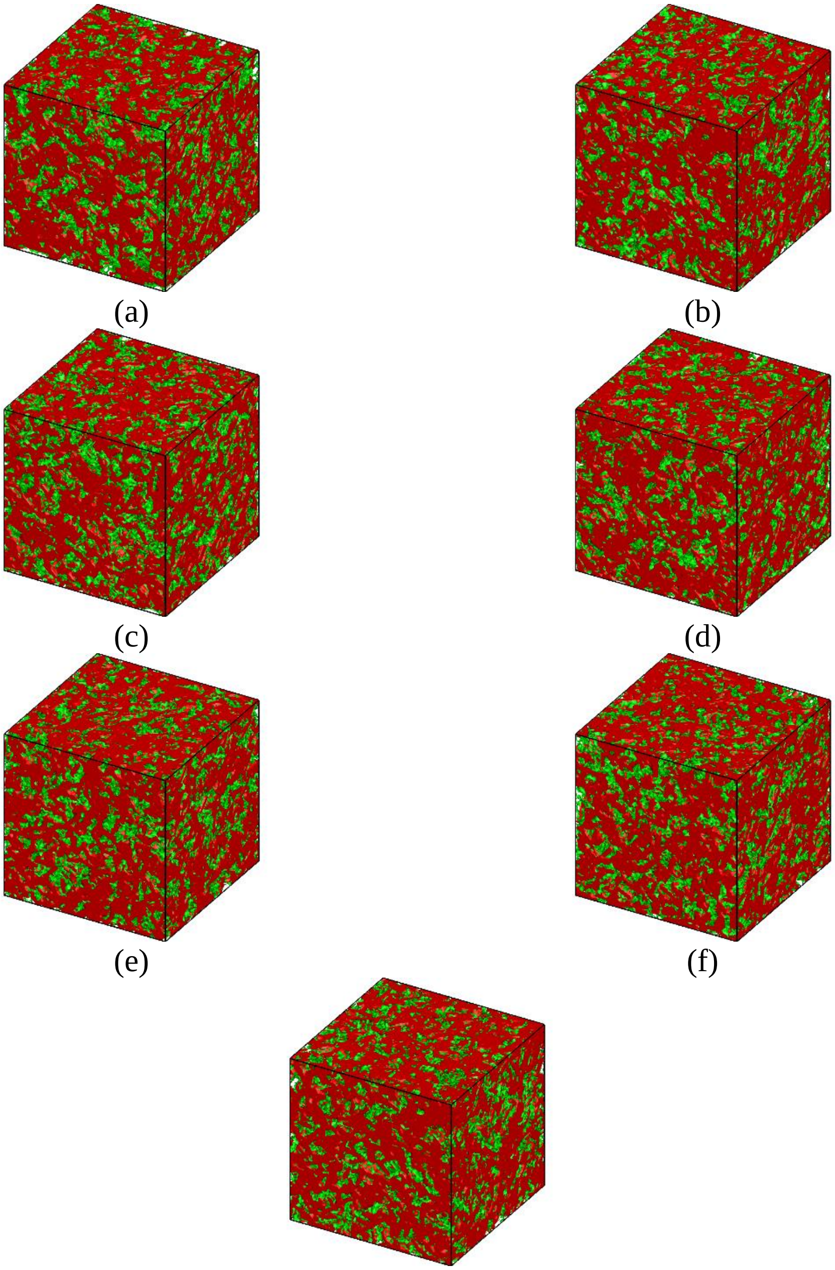

(a) (b) (c) (d) (e) (f) (g)

Figure 6. Micostructure with the same active material settings

An active material structure was generated 7 times and the same secondary phase deposition was applied to each structure using the previously determined voxel resolution and REV. In Figure 6, the figure shows the difference in the stochastic generation of active material structures that, while taking up the same active material volume, have different physical structures but the sample should be large enough that the statistical variation should be minimal. As the data from Table 3 shows, the deviation of the active area and conductivity is very low while the tortuosity is higher but within a sensible range within the norm that may be due to slight differences in active material volume and secondary deposition volume.

Table 3. Statistical variation in microstructure properties of the active material structure

runs	Porous vol%	Active Material vol%	Secondary Vol%	01 area	Tortuosity	Conductivity
1	24.5133	55.003	20.4861	1.348598002	20.23064833	0.287414
2	24.5134	55.0049	20.4814	1.334961042	16.582811	0.281977333
3	24.5156	55.0023	20.4818	1.354002082	16.05934	0.283945667
4	24.5016	55.0071	20.491	1.361647853	18.49791633	0.284204333
5	24.5162	55.0063	20.4772	1.356890929	19.09421133	0.283766333
6	24.5108	55.0023	20.4866	1.368773232	15.694484	0.283879667
7	24.5141	55.0049	20.4807	1.335714944	17.83843867	0.282074333

The fourth statistical analysis performed is adjusting the number of simultaneous depositions. The procedure by which the secondary phase deposits onto the active material structure requires multiple passes to completely deposit the desired volume percentage. Testing different number of simultaneous depositions per pass. Having a higher number of simultaneous depositions will likely result in a lower deposition accuracy that can affect the measurement results of the tortuosity and active area. However, decreasing the number of simultaneous depositions will increase the accuracy of the measurements but will also increase the number of passes needed and the number of calculations as well.

Table 4. Effect of the number of deposition sites on microstructure properties

Simultaneous Depositions	Porous vol%	Active Material vol%	Secondary Vol%	01 area	Tortuosity	Conductivity
1/25	23.2408	55.0049	21.754	1.164285539	18.912774	0.284400667
1/50	24.0479	55.0049	20.9469	1.275135882	16.43468467	0.282879
1/100	24.5165	55.0049	20.4783	1.338030025	16.79241867	0.281833
1/200	24.7484	55.0049	20.2464	1.366911827	16.98559967	0.281345667
1/400	24.8701	55.0049	20.1247	1.387333909	15.87457433	0.281087667

The results have been tabulated in Table 4. The number of simultaneous depositions increases as a fraction and so the fraction decreases from 1/25 to 1/400 with 1/25 having the highest number of simultaneous depostions and 1/400 having the lowest number of simultaneous depositions. This means that a finer result is produced as the fraction decreases. As for the measured results, the most noticeable effect caused by the depositions is the decrease in the secondary phase volume as the nsimultaneous fraction decreases and nears the desired secondary phase volume. Otherwise, the active area, tortuosity, and conductivity results begin to stabilize at the 1/100 fraction. However, using the nsimultaneous fraction of 1/400 slows down calculation significantly. The choice was made to use the 1/100 fraction as the calculation speed was much quicker while the results were determined to be within the margin of error.

Table 5. Statistical variation in microstructure properties due to stochastic generation

Runs	Porous vol%	Active Material vol%	Secondary Vol%	01 area	Tortuosity	Conductivity
1	24.5141	55.0049	20.4807	1.335714944	17.83843867	0.282074333
2	24.5086	55.0049	20.4862	1.336342084	16.69759867	0.281802
3	24.5002	55.0049	20.4946	1.335301299	16.39764567	0.282242
4	24.5138	55.0049	20.481	1.333479924	18.56981833	0.282097333
5	24.5142	55.0049	20.4806	1.341465952	17.61741267	0.281909667
6	24.5177	55.0049	20.4771	1.335181208	16.421365	0.282443
7	24.51	55.0049	20.4848	1.32821595	16.34069567	0.281939

Now that the REV, resolution, and deposition rate have been determined, the fifth statistical analysis is to ensure that the secondary phase deposition provides consistent results each time. Thus, a similar study to the third study is performed. This time, the secondary phase is deposited onto an active material microstructure several times to show that the results of deposition will generate similar measurement results regardless of deposition. This is to prove that the deposition for a certain set of parameters will not vary randomly.

Like the 3rd analysis, this analysis focuses on the repetition of the secondary phase volume. In Figure 7, the active material structures are all the same but the secondary phase volumes all take up the same volume percentage but deposit in different ways on the active material structure. As the data in Table 5 shows, there is very little variation in the conductivity and active area. However, the tortuosity has a higher variation but this type of variation is expected in the measurement of tortuosity and can be concluded to be within the margin of error.

The results of the statistical analysis show that an REV with sides of 100 um, a voxel length of 10 um, and 100 simultaneous depositions will have representative results. Now that the statistical analysis has been done, a parametric study can be done on the microstructures to determine how the active area, specific conductivity, and specific tortuosity changes as a result of variation in microstructure properties

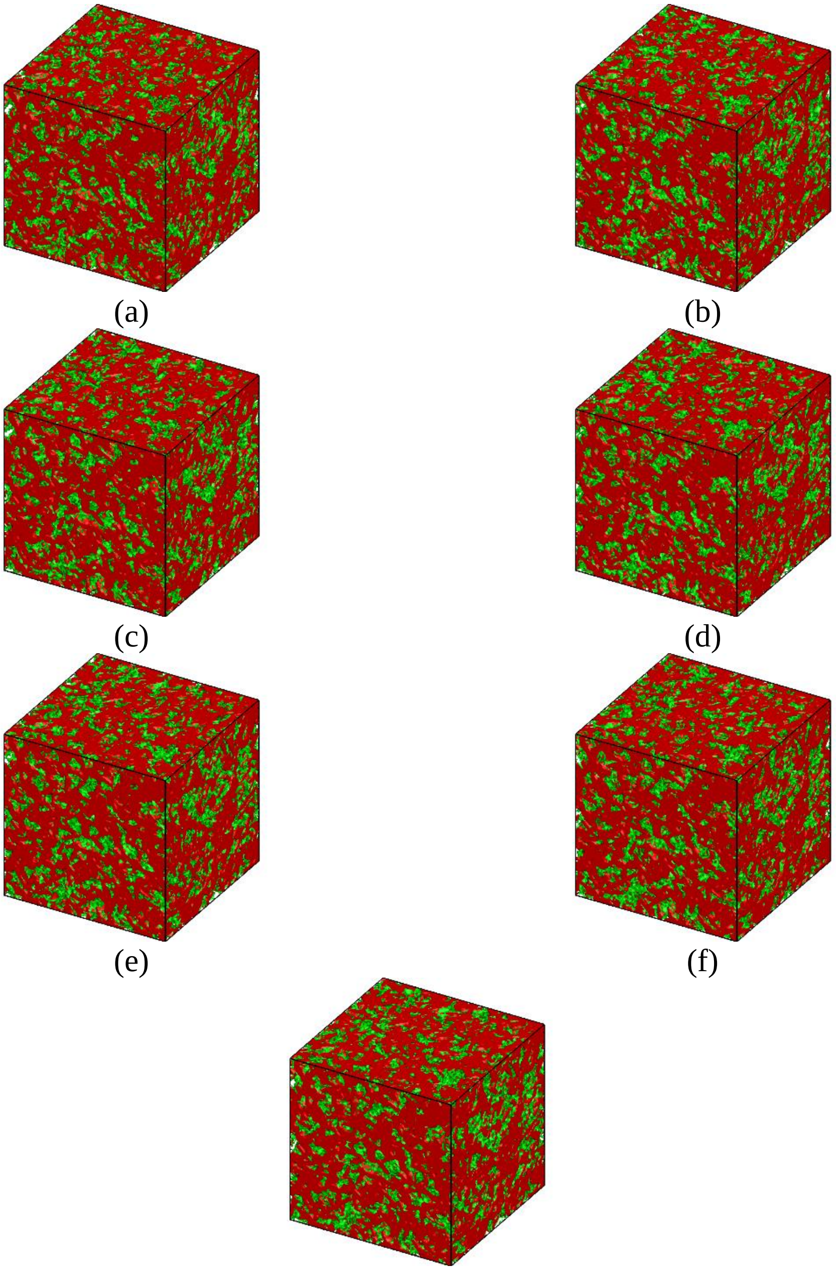
(a) (b) (c) (d) (e) (f) (g)

Figure 7. Micostructure with the same active material structure with 20 vol% deposition

3.4 Microstructure Generation

Microstructures were generated for the cathode and anode where the active material of the cathode was NMC and the active material for the anode was graphite. However, the secondary phase deposition for both electrode was comprised of a mixture of PVDF and conductive additive. There are a number of differences that need to be accounted for while generating the microstructures. The first difference is that the shape of the NMC and graphite particles are fundamentally different. NMC particles are generally spherical while graphite particles are elliptical platelets. However, there is not much information about the specific details of the shape of the platelets. From literature, there are details about the active material loading, and it is known that the basal plane of the platelet is much larger than the edge plane.[56-61] What is largely unknown is the aspect ratio of the elliptical basal plane. There is very little conclusive data on how circular the basal plane. While the active material structure for the cathode is modeled to be fully comprised of spherical particles, the active material structure generated for the anode has two additional factors that need to be included. These factors are the basal plane aspect ratio, measured as the ratio of the minor radius b and the major radius a, and the edge plane aspect ratio, measured as the ratio of the height h and the major radius a.

Besides the aspect ratios introduced with the platelet particles, the parametric variables for the anode and cathode are the same. A selection of secondary phase volume percentage, porosity volume percentage, and morphology factor ω. When the active material structure is first generated, the desired porosity and secondary volume percentage have to be taken into account for since the active material volume percentage is the first value accounted for and an additional secondary phase volume percentage is added to that to total the desired porous volume percentage. The morphology factor comes into play during the secondary phase deposition. This factor is a way to determine the likelihood that the secondary phase will deposit on itself rather than on the active material structure. The morphology factor is used as a way to quantify the effect of different manufacturing procedures. It is difficult to measure exactly what manufacturing changes will result in different morphological changes so a range of values for the morphology factor will need to be tested. This is important as the morphology factor can affect the active area and tortuosity drastically. If the morphology factor is higher then the chance of self deposition increases and the active area will also increase for larger secondary phase volume percentages. However, a higher morphology factor is also likely to increase the tortuosity as the secondary phase volume increases.

Figure 8 shows the combination of parameters used in the microstructure generation. From Figure 8b, the anode there are five categories: porosity vol%, binder vol%, morphology factor, basal plane aspect ratio, and edge plane aspect ratio which produces a total of 1024 different microstructures that need to be generated for the parametric study. However, from Figure 8a, the cathode does not need to include aspect ratios as the particle of NMC is spherical and only requires porosity vol%, binder vol%, and morphology factor for a total of 125 different microstructures.

ω
0.1
0.3
0.5
0.7
0.9

x

Porosity Vol %
15
20
25
30
35

x

Secondary Phase Vol %
0
10
20
30
40

(a)

$\frac{h}{a}$
0.2
0.4
0.6
0.8

x

$\frac{b}{a}$
0.4
0.6
0.8
1.0

x

ω
0.2
0.4
0.6
0.8

x

Porosity Vol %
25
30
35
40

x

Secondary Phase Vol %
0
10
20
30

(b)

Figure 8. Microstructure parametric input for (a) cathode and (b) anode

Knowing the desired active material vol%, secondary vol%, and porous vol% allows for the generation of desired microstructures as previously stated. As shown in Figure 8, the active material structure is created first with increasing active material vol% to match the desired prescribed porous vol%. For the anode, this is done repeatedly to include all combinations of basal and edge aspect ratios. Then the secondary phase addition is deposited with increasing amounts of binder such that the porosity is kept at its prescribed value.

Once the active material structures are completed, the secondary deposition can occur and is added until the prescribed secondary vol% and porous vol% are met. The secondary phase deposition is done on all of the previously generated active material structures again and again until all combinations of porosity vol%, binder vol%, and morphology factor have been applied.

Figure 9 shows an example of the progression of deposition occurs as the active material vol% and secondary vol% increase. All completed microstructures were measured for the active areas between the porous vol%, active material vol%, and secondary vol%. Additionally, the tortuosity and conductivity of the structures were measured in the x, y, and z directions. Once the tortuosity and conductivity in x, y, and z were measured, the average of the values were taken to determine the effective tortuosity and effective conductivity. Figure 10 shows an example of the 3D scalar fields of the tortuosity and conductivity vary in the x, y, and z directions. Note that the tortuosity gradient field shows the values in the porous space and the conductivity gradient field shows the conductivity through the particles. The subtle difference in the gradients show the variation of tortuosity measurements in different axes and why it is needed to measure these values in all axes.

The tabulated microstructure data is then used to develop a set of functional correlations for the properties of the anode and cathode. Separate correlations were developed for the active material-pore area, the active material-secondary phase area, the active material surface area, the secondary phase-pore area, the tortuosity, and the conductivity. As previously stated, the anode microstructure has two more variables that need to be accounted for so the anode and cathode will have different correlations as well. The values of the conductivity and tortuosity in the x, y, and z directions were averaged to find the effective conductivity and tortuosity. These averaged values were used for the correlations extraction.

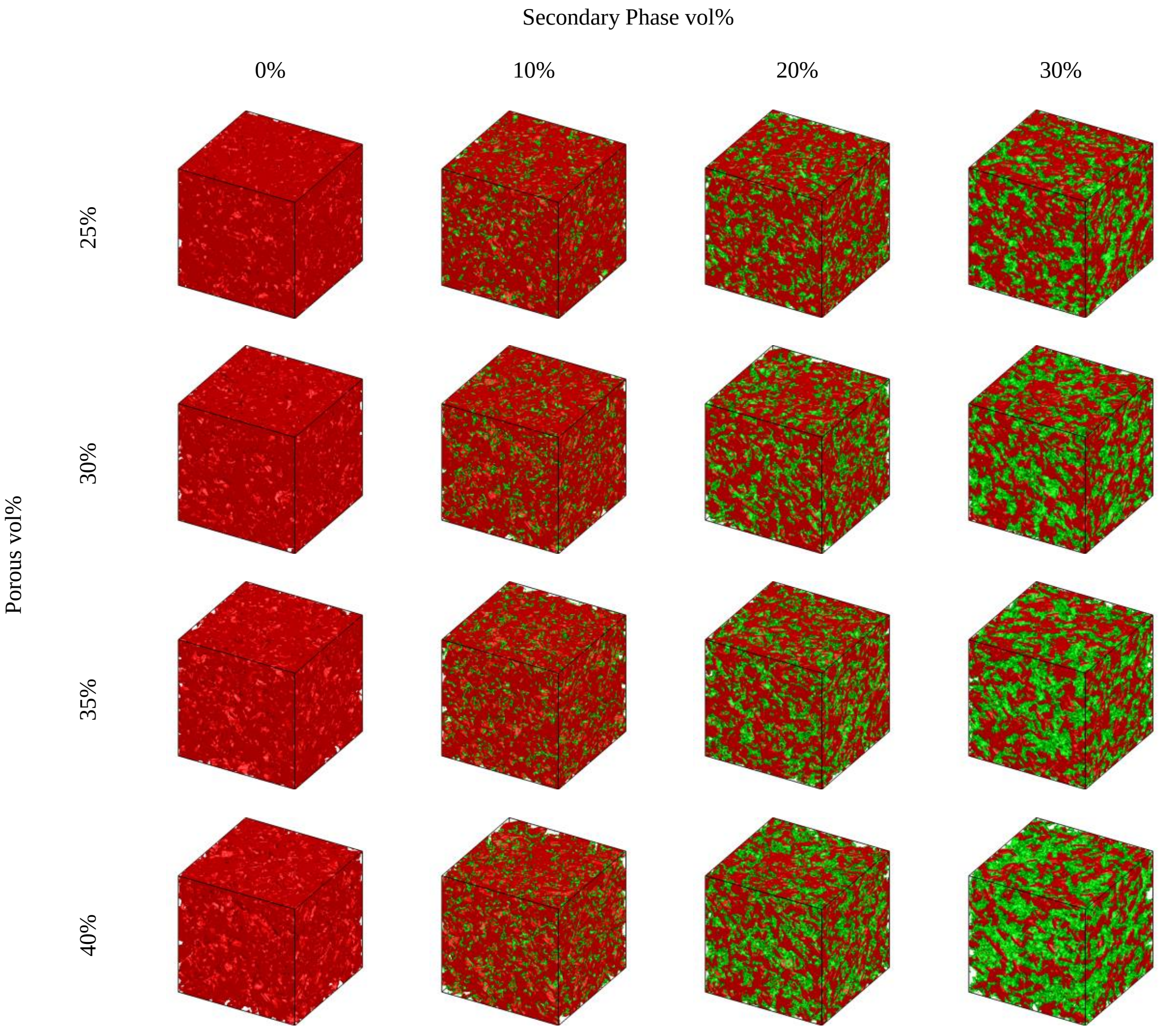

Figure 9. Anode Microstructure as porosity and secondary phase vol% increase

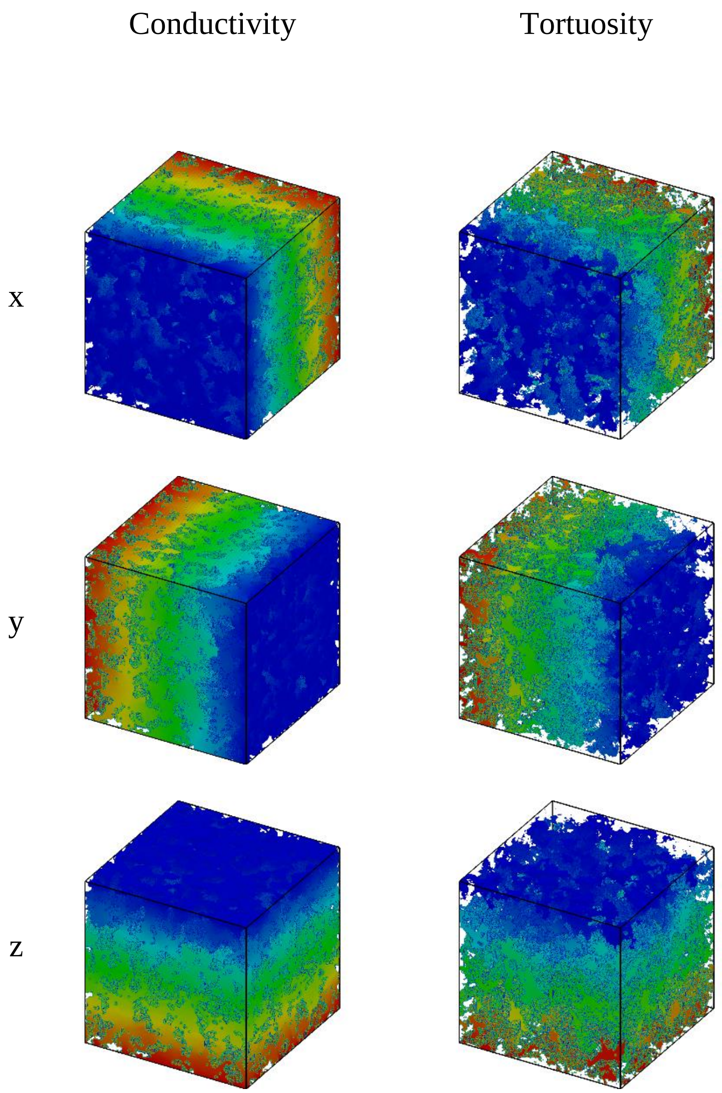

Figure 10. Conductivity and Tortuosity in x, y, and z axis

3.5 Deriving Functional Dependence of Porous Electrode Properties

The data was evaluated using matlab and plotted in a 3D space where the x-axis was the porosity vol%, the y-axis was the binder vol%, and the z-axis was the examined property. Since there are more than three independent variables in the anode and cathode, separate evaluations were made for each increase in the morphological factor ω, and then even more separate evaluations for the anode as the relationship including the edge and basal plane aspect ratios also need to be determined.

Table 6. Cathode expressions describing microstructural properties of composite electrodes made up of spherical active material particles and coefficient of determination. The relations express each of the properties as a function of porosity, secondary phase volume fraction and morphology factor.

Microstructural property	Expression	Coefficient of determination, R^2
Active material – pore area	$a_{01} = \left(-1.8079(1-\varepsilon-\varepsilon_2)^2 + 1.4103(1-\varepsilon-\varepsilon_2) + 0.9247\right) * e^{-\varepsilon_2(28.2684+5.1843\varepsilon_2-21.9745\omega)}$	0.9981
Active material – secondary phase area	$a_{12} = \varepsilon_2(1-1.6119\varepsilon_2-0.0663\omega) * \left(7.4654(1-\varepsilon-\varepsilon_2)^2 + 2.3173(1-\varepsilon-\varepsilon_2) + 4.2340\right)$	0.9341
Active material surface area	$a_{1(0+2)} = -3.5932(1-\varepsilon-\varepsilon_2)^2 + 4.3319(1-\varepsilon-\varepsilon_2) - 0.2483$	0.9580
Secondary phase – pore area	$a_{20} = \varepsilon_2(1-1.8744\varepsilon_2+0.0521\omega) * \left(-59.5423(1-\varepsilon)^2 + 74.1352(1-\varepsilon) - 10.3652\right)$	0.9435
Tortuosity	$\tau = \left(0.6768 - 5.1707\varepsilon_2 + 12.0492\varepsilon_2^2 + 0.5283\varepsilon_2\omega\right) * \varepsilon^{-\left(1.2790+9.2521\varepsilon_2-22.9833\varepsilon_2^2-0.2939\varepsilon_2\omega\right)}$	0.7432
Conductivity	$\sigma = \varepsilon_2(0.1839-0.4219\varepsilon+1.0475\varepsilon_2-0.0186\omega)$	0.9900

The figures below in Figure 11-16 show the 3D contours of the cathode with a fixed morphology factor. The points are from the measured data from the microstructure data set. The points of data are curve-fitted to extract a correlation. The 3D contours in the figure shows the curve fit of the extracted correlation against the data set. The functional relationships and the coefficient of determination can be found in Table 6 for the cathode and Table 7 for the anode.

In Figure 11, the data shown is for the functional dependence of the active material phase-porous phase interfacial area in the cathode. The curve increases exponentially as the secondary phase decreases. What the data shows is that as porosity increases, the interfacial area slightly increases. However, as the morphological factor increases, the interfacial increases significantly. This makes sense because, the morphological factor determines if the secondary phase will deposit on the active material structure or not and increasing the likelihood of self deposition will increase the active material-porous interfacial area.

Table 7. Anode expressions describing microstructural properties of composite electrodes made up of spherical active material particles and coefficient of determination. The relations express each of the properties as a function of porosity, secondary phase volume fraction and morphology factor.

Microstructural property	Expression	Coefficient of determination, R^2
Active material – pore area	$a_{01} = \left(1.6552 + 8.9631(1-\varepsilon-\varepsilon_2) - 9.0132(1-\varepsilon-\varepsilon_2)^2\right)$ $*e^{\varepsilon_2(-8.0502-1.8920\varepsilon_2+4.7374\omega)(1.4039-2.3096h+1.5308h^2)(1.9284-1.6294b+0.7602b^2)}$	0.9732
Active material – secondary phase area	$a_{12} = (1.6292 + 12.1075(1-\varepsilon-\varepsilon_2) - 5.3096(1-\varepsilon-\varepsilon_2)^2)$ $*\varepsilon_2(1-1.1578\varepsilon_2 - 0.2646\omega)$ $*(2.2969 - 2.6953h + 1.7510h^2 + 2.4435 - 1.4222b + 0.6747b^2)$	0.9916
Active material surface area	$a_{1(0+2)} = (-0.3816 + 9.9848(1-\varepsilon-\varepsilon_2) - 8.6440(1-\varepsilon-\varepsilon_2)^2)$ $*(1.6054 - 2.4667h - 1.6379h^2)(2.2784 - 1.7966b + 0.8503b^2)$	0.9728
Secondary phase – pore area	$a_{20} = (0.8906 + 8.8621(1-\varepsilon) - 8.6711(1-\varepsilon)^2)$ $*\varepsilon_2(1-1.5796\varepsilon_2 + 0.0303\omega)(2.8220 - 0.8011h + 0.2611h^2)$ $*(2.8624 - 0.6761b + 0.2126b^2)$	0.9929
Tortuosity	$\tau = (0.5808 + 2.41\varepsilon_2 - 1.8620\varepsilon_2{}^2 + 0.5333\varepsilon_2\omega)$ $*(0.6617 + 0.2643h + 3.4104h^2)(0.6441 - 0.8419b + 0.3891b^2)$ $*\varepsilon^{(-1.0522+1.2666\varepsilon_2-0.9306\varepsilon_2{}^2-0.5961\varepsilon_2\omega)(1.5636-2.1463h+1.1537h^2)(2.1711+1.2525b-0.2530b^2)}$	0.9704
Conductivity	$\sigma = (0.9547 + 0.9852\varepsilon_2 - 1.4836\varepsilon_2{}^2 - 0.0697\varepsilon_2\omega)$ $*(0.9472 + 0.3806h - 0.2624h^2)(0.9469 + 0.2492b - 0.1241b^2)$ $*(1-\varepsilon-\varepsilon_2)^{(1.6507+0.5783\varepsilon_2-2.8421\varepsilon_2-0.0575\varepsilon_2\omega)*(1.0176+0.8864h-0.6257h^2)(1.0420+0.5237b-0.3041b^2)}$	0.9978

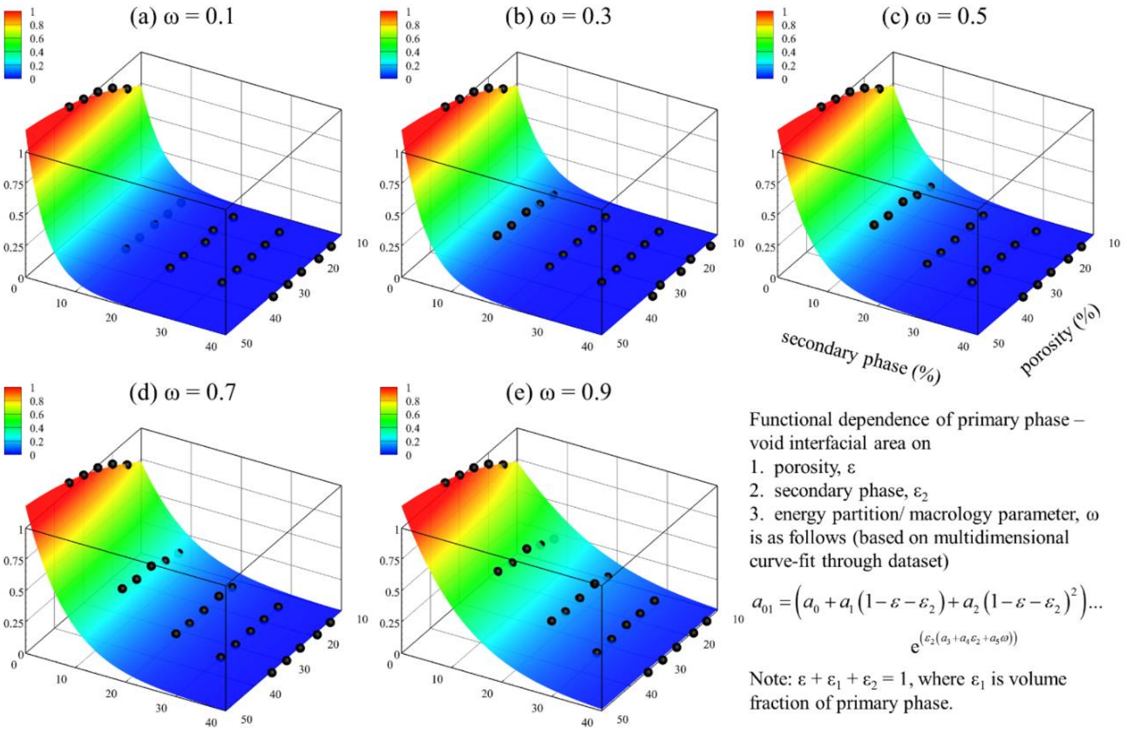

Functional dependence of primary phase – void interfacial area on

1. porosity, ε
2. secondary phase, ε_2
3. energy partition/ macrology parameter, ω

is as follows (based on multidimensional curve-fit through dataset)

$$a_{01} = \left(a_0 + a_1\left(1-\varepsilon-\varepsilon_2\right) + a_2\left(1-\varepsilon-\varepsilon_2\right)^2\right)\ldots \; e^{\left(\varepsilon_2\left(a_3+a_4\varepsilon_2+a_5\omega\right)\right)}$$

Note: $\varepsilon + \varepsilon_1 + \varepsilon_2 = 1$, where ε_1 is volume fraction of primary phase.

Figure 11. Cathode Microstructure active material-porous interfacial area

Figure 12 shows the functional relationship of the active material-secondary phase interfacial relationship for the cathode. The curve follows an negative parabolic shape. The area is lower at lower secondary phase vol% and peaks at a secondary phase vol% of 25%. As the porosity increases, the initial interfacial increases but the peak also decreases. When the morphological factor increases, the area faces a small uniform decrease along the entire curve.

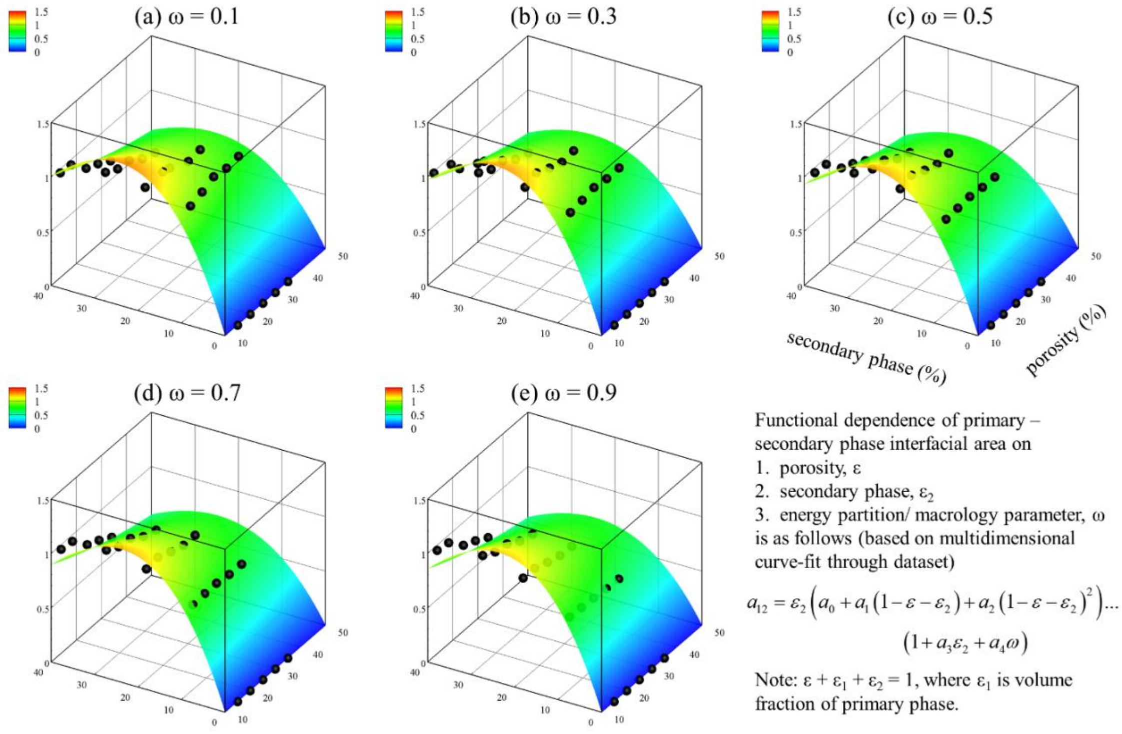

Functional dependence of primary – secondary phase interfacial area on

1. porosity, ε
2. secondary phase, ε_2
3. energy partition/ macrology parameter, ω

is as follows (based on multidimensional curve-fit through dataset)

$$a_{12} = \varepsilon_2 \left(a_0 + a_1 \left(1 - \varepsilon - \varepsilon_2\right) + a_2 \left(1 - \varepsilon - \varepsilon_2\right)^2 \right) \ldots \left(1 + a_3 \varepsilon_2 + a_4 \omega\right)$$

Note: $\varepsilon + \varepsilon_1 + \varepsilon_2 = 1$, where ε_1 is volume fraction of primary phase.

Figure 12. Cathode Microstructure active material-secondary phase interfacial area

Figure 13 shows the active material surface area for the cathode. As this is the surface area of the active material, there is no change as the morphological factor changes as the morphology factor only affects the secondary phase deposition. Also as expected, the active material surface area is at its lowest when the secondary phase and porous volume percentages are highest There seems to be a maxima when the active material volume percentage is about 50 vol%. There is also a decrease when both the secondary phase and porous volumes are both low as well.

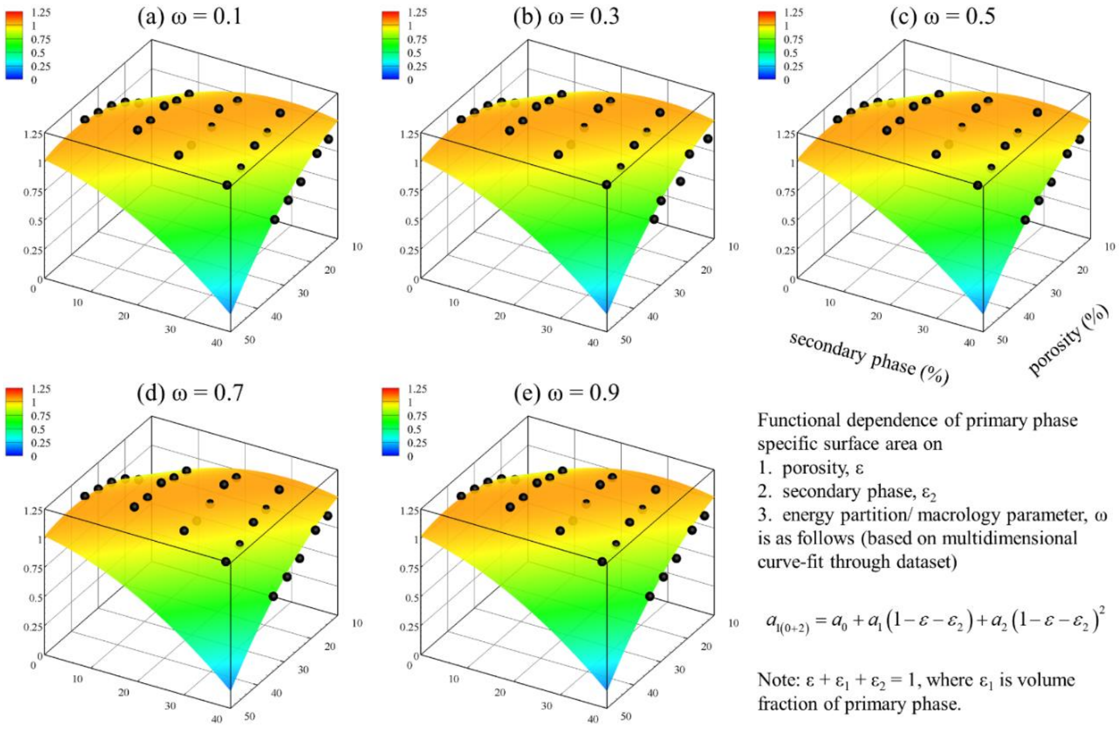

Functional dependence of primary phase specific surface area on

1. porosity, ε
2. secondary phase, ε_2
3. energy partition/ macrology parameter, ω

is as follows (based on multidimensional curve-fit through dataset)

$$a_{1(0+2)} = a_0 + a_1\left(1-\varepsilon-\varepsilon_2\right) + a_2\left(1-\varepsilon-\varepsilon_2\right)^2$$

Note: $\varepsilon + \varepsilon_1 + \varepsilon_2 = 1$, where ε_1 is volume fraction of primary phase.

Figure 13. Cathode Microstructure active material structure surface area

Figure 14 shows the secondary phase-porous interfacial area for the cathode. Similar to the active material-secondary phase curve, the shape has an inverse parabolic curve as well in regards to the secondary phase addition. In the case, as the porosity increases, the curve will also increase at higher secondary phase volume percentages. As the morphological factor increases, the interfacial area also increases but at a smaller rate than from the increase in porosity.

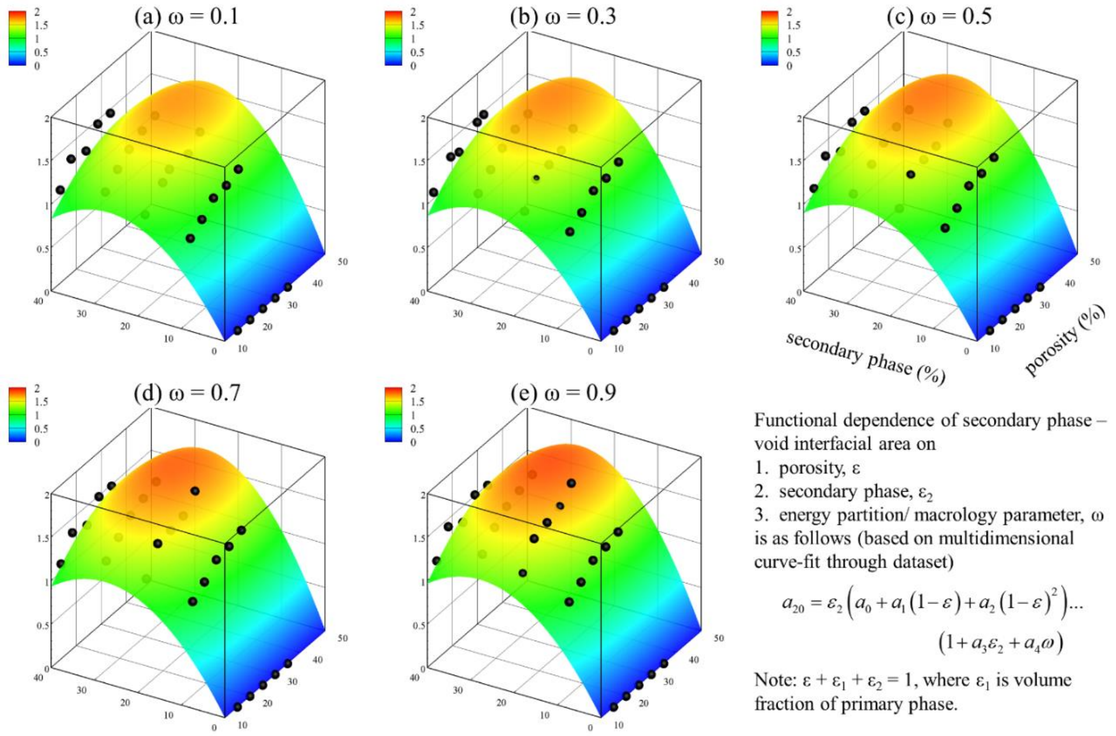

Functional dependence of secondary phase – void interfacial area on

1. porosity, ε
2. secondary phase, ε_2
3. energy partition/ macrology parameter, ω

is as follows (based on multidimensional curve-fit through dataset)

$$a_{20} = \varepsilon_2 \left(a_0 + a_1 (1-\varepsilon) + a_2 (1-\varepsilon)^2 \right) \ldots \left(1 + a_3 \varepsilon_2 + a_4 \omega \right)$$

Note: $\varepsilon + \varepsilon_1 + \varepsilon_2 = 1$, where ε_1 is volume fraction of primary phase.

Figure 14. Cathode Microstructure Secondary Phase-Porous interfacial area

Figure 15 shows the tortuosity functional relationship for the cathode. When the porosity is high, the uniformly low. When the porosity decreases, the tortuosity increases exponentially. However, as the secondary phase decreases and the active material phase increases, for any given porous volume percentage, the tortuosity seems to have two peaks in regards to the secondary phase. One peak at about 30 vol% and a higher peak at 10 vol%. This may be due to the abundance of the secondary phase at 30 vol% impeding the kinetics while the density of the active material may be the cause when the secondary phase is at 10 vol%.

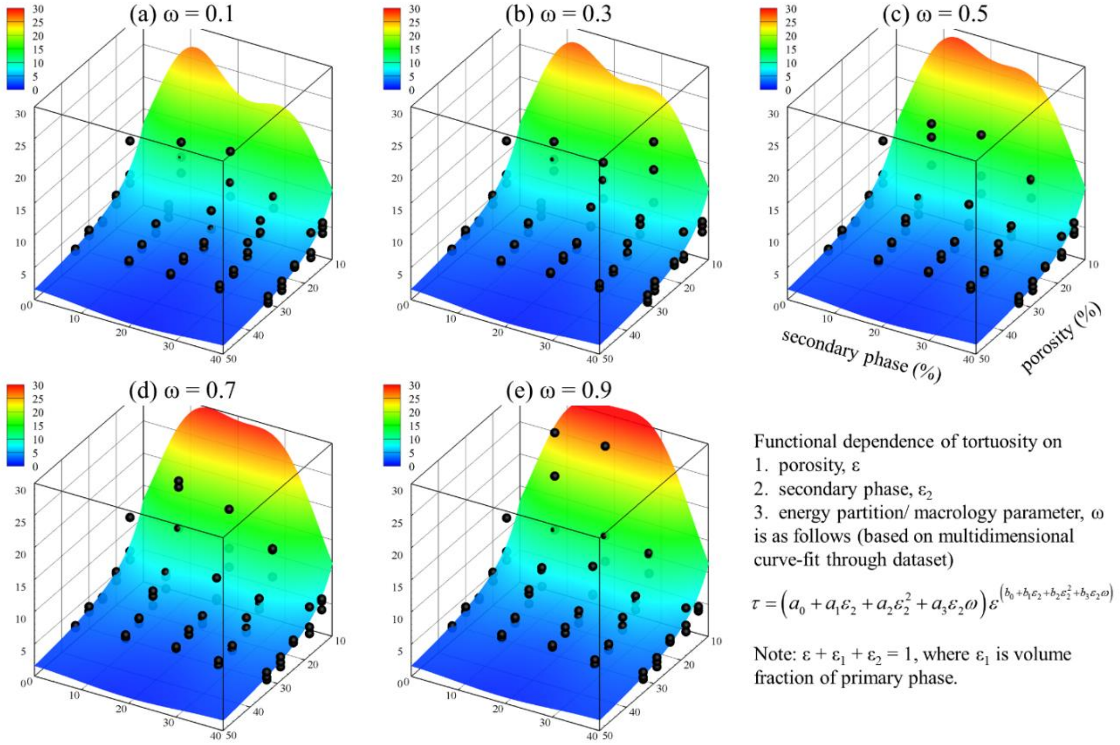

Functional dependence of tortuosity on
1. porosity, ε
2. secondary phase, ε_2
3. energy partition/ macrology parameter, ω
is as follows (based on multidimensional curve-fit through dataset)

$$\tau = \left(a_0 + a_1\varepsilon_2 + a_2\varepsilon_2^2 + a_3\varepsilon_2\omega\right)\varepsilon^{\left(b_0 + b_1\varepsilon_2 + b_2\varepsilon_2^2 + b_3\varepsilon_2\omega\right)}$$

Note: $\varepsilon + \varepsilon_1 + \varepsilon_2 = 1$, where ε_1 is volume fraction of primary phase.

Figure 15. Cathode Microstructure Tortuosity

Figure 16 shows the conductivity profile for the cathode. Normally the active material is not very conductive so as the secondary phase volume percentage increases, there is an increase in the conductivity. Additionally, as the porous volume decreases, which allows for a larger volume of active material and secondary phase, the conductivity will increase. However, changing the morphological factor does not appear to cause any change in conductivity.

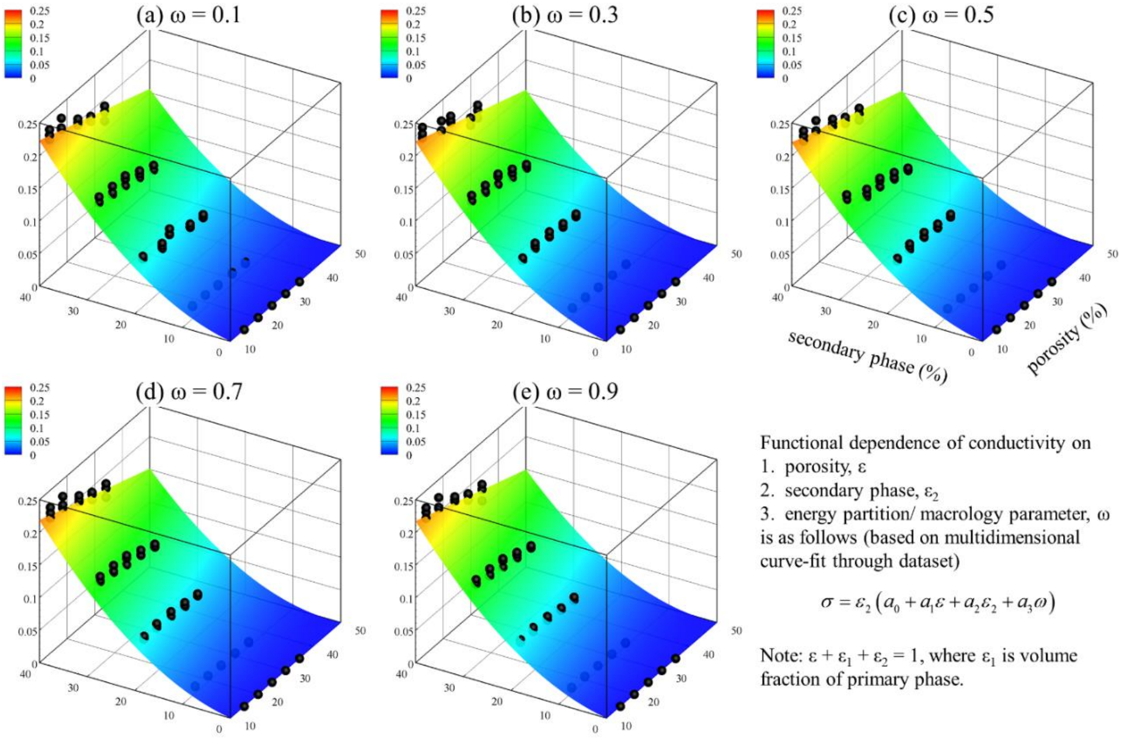

Functional dependence of conductivity on
1. porosity, ε
2. secondary phase, ε_2
3. energy partition/ macrology parameter, ω
is as follows (based on multidimensional curve-fit through dataset)

$$\sigma = \varepsilon_2 \left(a_0 + a_1\varepsilon + a_2\varepsilon_2 + a_3\omega \right)$$

Note: $\varepsilon + \varepsilon_1 + \varepsilon_2 = 1$, where ε_1 is volume fraction of primary phase.

Figure 16. Cathode Microstructure Conductivity

Figures 17-22 show 2D contours and line plots of the anode microstructure properties. These plots show the effect of increasing the binder weight percentage and morphology factor, the effect of platelet shape, and the effect of porosity. The secondary phase contours show the effect of binder as it increases from 0 to 10 wt% and as the morphology factor increases from 0 to 1. The particle morphology contour features an increase in the edge plane aspect ratio and basal plane aspect ratio from 0.05 to 0.95. The line plots show the effect of increasing porosity in a variety of different anode microstructures.

Figure 17 shows the effect on the active material-porous interfacial area. In Figure 17a, it shows that as the binder wt% increases, there is a subsequent decrease in the interfacial area. Also, as the morphology factor ω increases, the active area increases. This should be expected as similar results were found in the cathode. More binder will result in lower active interfacial area but increased likelihood of self-deposition will result in a higher active area. In Figure17b, as the particle becomes rounder and thicker, the active area decreases. Conversely, the active area is at its highest when the particles are thinner and narrower. Notably, there appears to be a parabolic contour when the basal aspect ratio is low. In general, it seems thinner graphite particles with low edge plane aspect ratios will result in the best results. Incidentally, rounder particles seem to have the worst results but it does not necessarily seem that a round particle will decrease the active area. Finally, Figure 17c shows that increasing the porosity will uniformly increase the active area as the porous space increases in relation to the volume percentage of the active material and binder phase.

Figure 18 shows the active material-secondary phase interfacial area. Figure 18a shows that the morphology factor has almost no effect on the interfacial area. However, as the binder wt% increases, the active material-secondary phase interfacial area increases. This makes sense as the increase in binder results in a larger binder surface area that is in contact with the active material. Figure 18b shows similar results to Figure 17b where the roundest and thickest particles have the lowest interfacial area while the thinnest and narrowest particles have the lowest results. Figure 18c shows that as the porosity increases, there is a maximum at about 39 vol% and decreases slightly after that peak.

Figure 19 shows the active material surface area. In Figure 19a, the morphology factor has a low effect at low binder wt%, but as the binder wt% increases, Once again, Figure 19b shows similar results to the other properties as the rounder and thicker particles have the lowest interfacial areas. However, it seems that the effect of particle roundness is slightly shifted to the right with higher values the slimmer the particle is. In Figure 19c, as porosity increases, there is a consistent trend that the active material surface area decreases. This could make sense as less active material is present in the microstructure as the porosity increases.

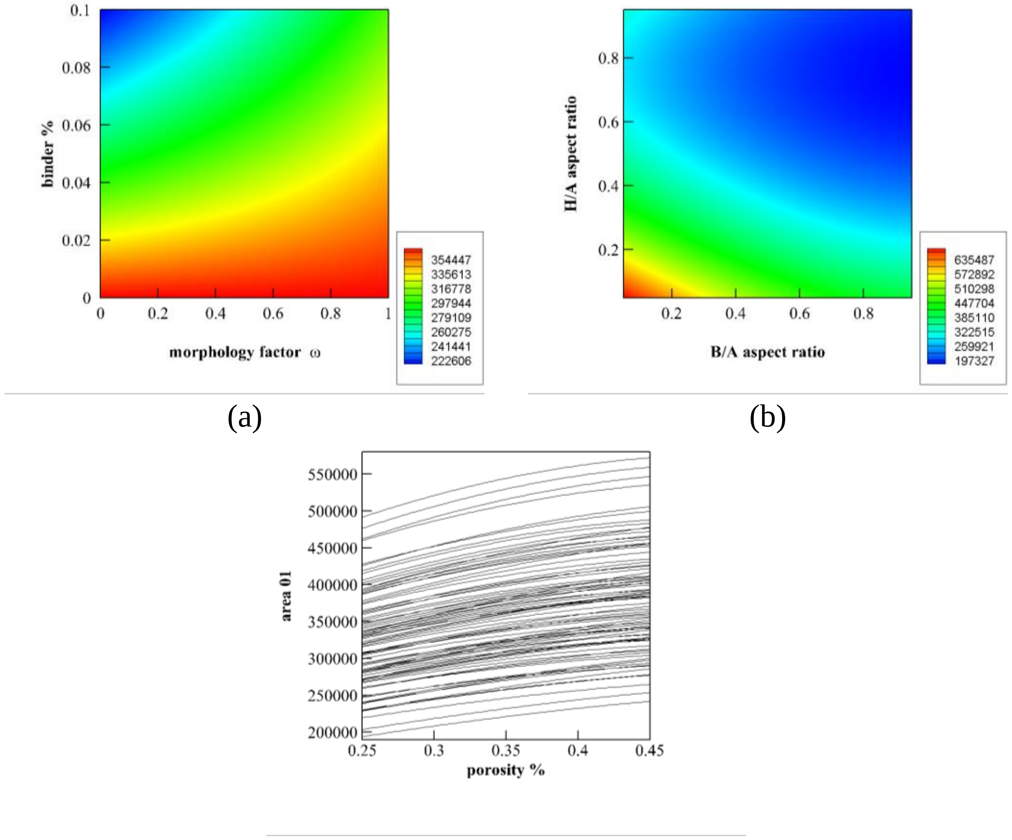

(a)

(b)

©

Figure 17. Anode active material-porous interfacial area in regards to (a) binder and morphology factor, (b) graphite particle morphology, and (c) porosity

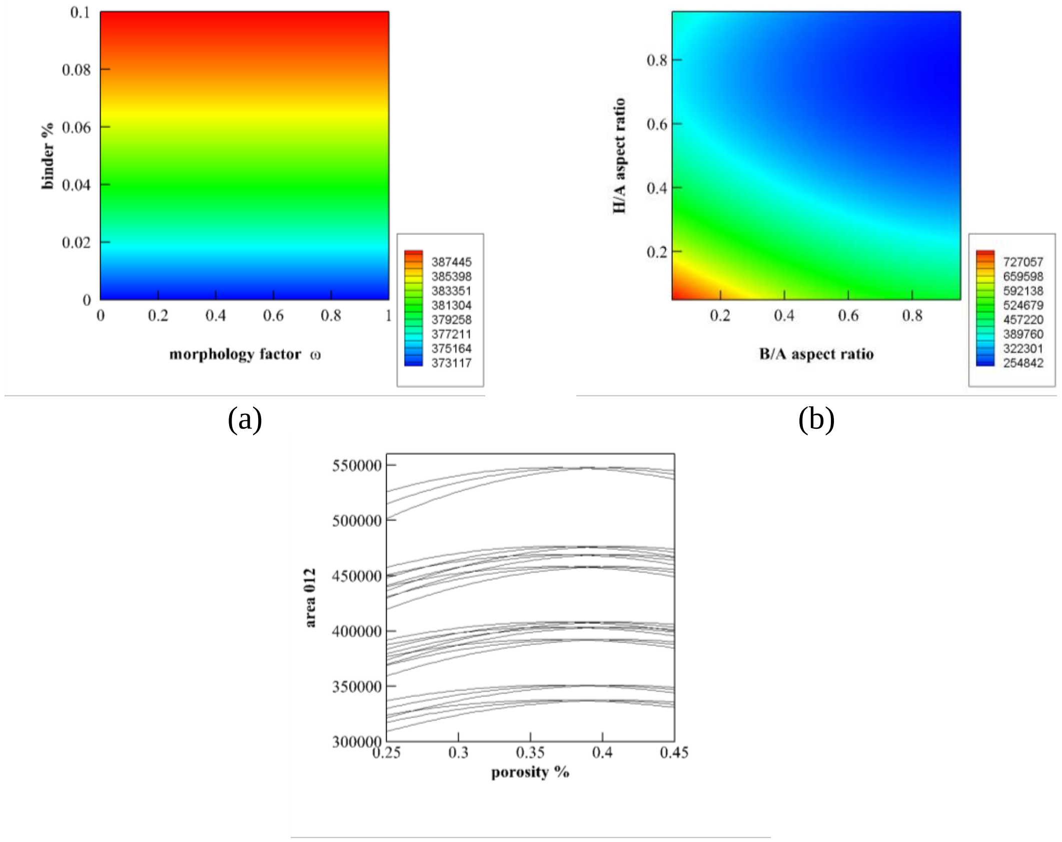

(a) (b)

(c)

Figure 18. Anode active material-secondary phase interfacial area in regards to (a) binder and morphology factor, (b) graphite particle morphology, and (c) porosity

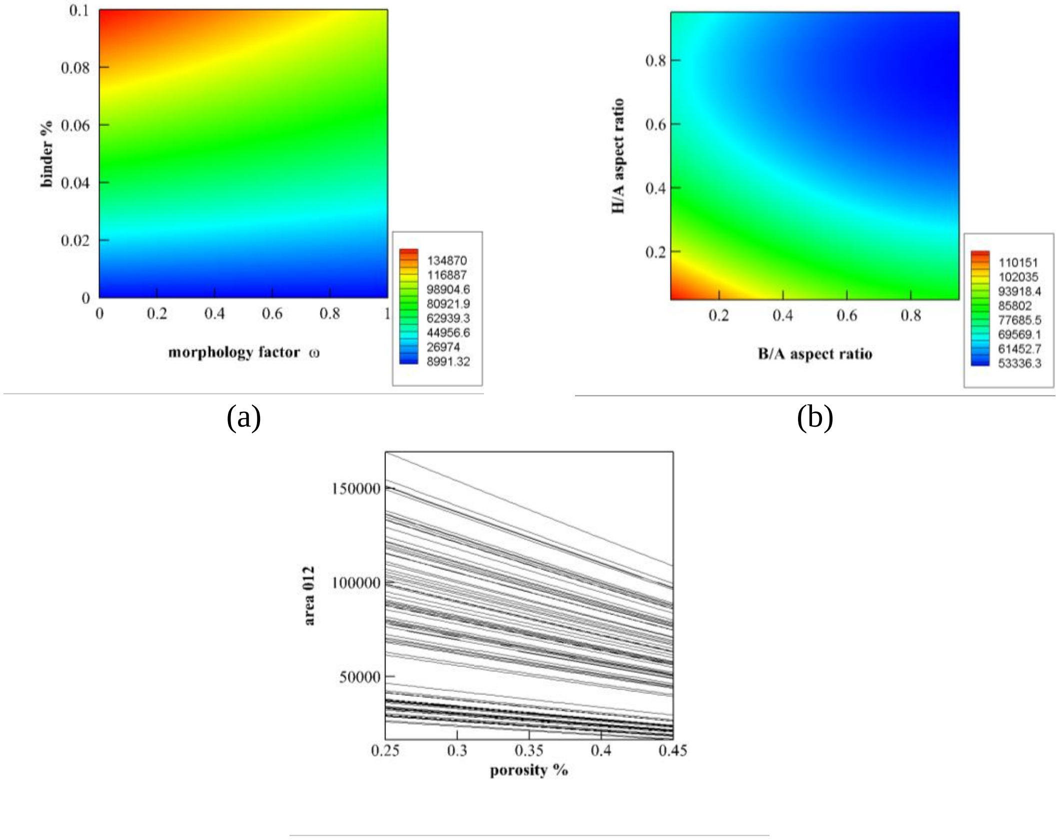

(a) (b)

(c)

Figure 19. Anode active material surface area in regards to (a) binder and morphology factor, (b) graphite particle morphology, and (c) porosity

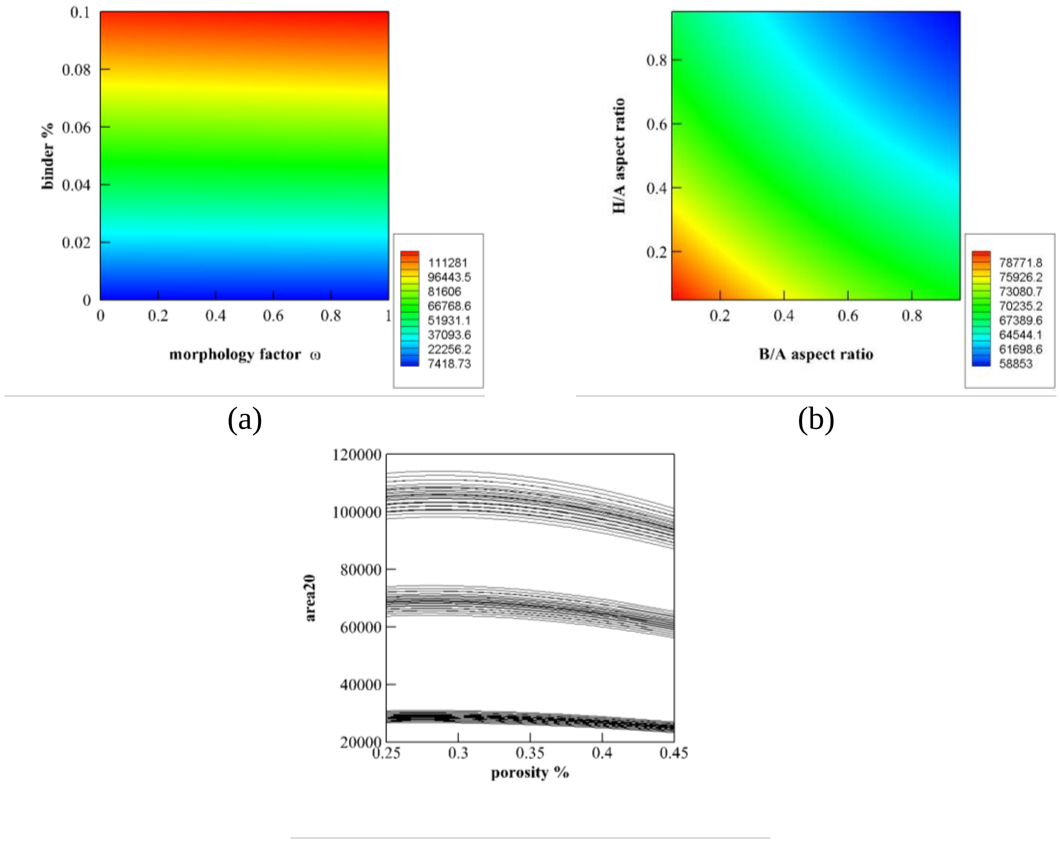

(a) (b)

(c)

Figure 20. Anode secondary phase-porous interfacial area in regards to (a) binder and morphology factor, (b) graphite particle morphology, and (c) porosity

Figure 20 shows the secondary phase-porous interfacial area. Figure 20a shows that there is a minimal effect due to the morphology factor. However, the binder wt% does have an effect. When the binder wt% increases, there is also an increase in the interfacial area. Seemingly, in Figure 20b the interfacial area would change as the morphology changes due to the change in how deposition occurs on the secondary phase but that does not appear to be the case. As the basal plane and edge plane aspect ratio increases, the interfacial area decreases. So the thinnest and narrowest particles have the highest interfacial area and the roundest and thickest particles have the lowest aspect ratios. This may be because active material structures with low aspect ratios have the highest surface areas that allow for the most coverage of binder. As the porosity increases, in Figure 20c, there is a negative parabolic shape to the curve with a maximum at around 28 vol%. So that would indicate that lower porosities will yield the best secondary-porous interfacial areas.

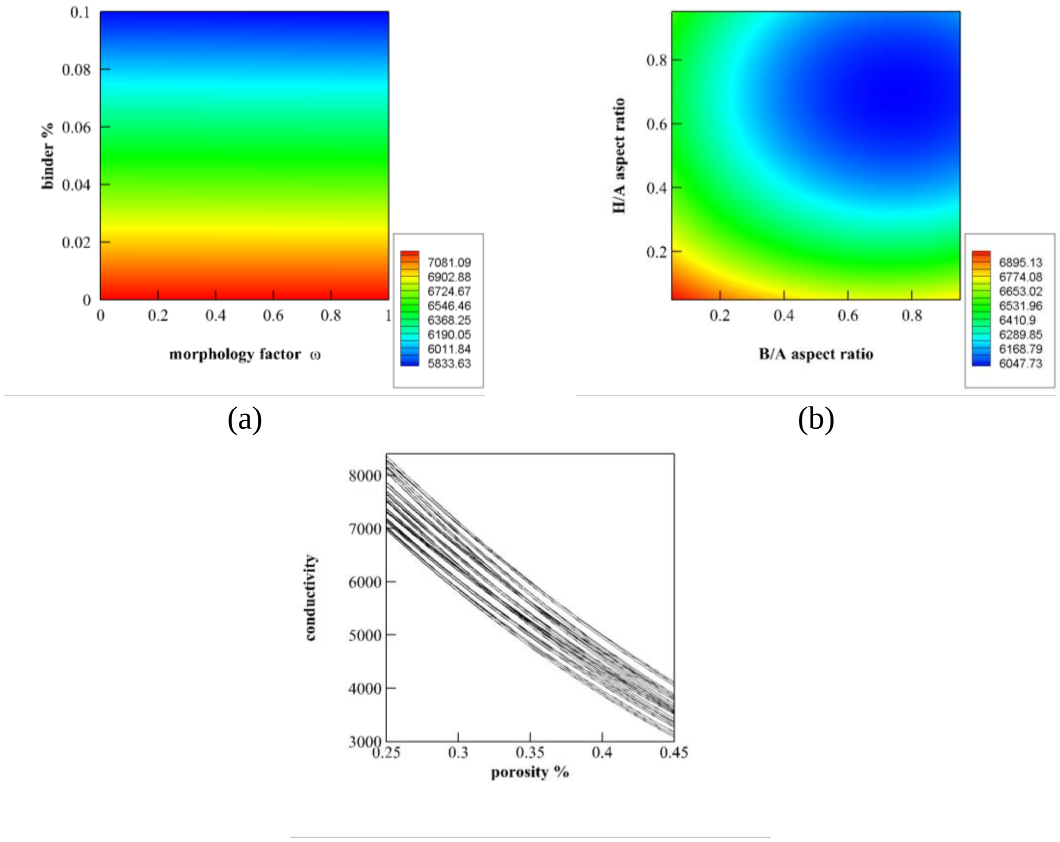

(a)

(b)

(c)

Figure 21. Anode Conductivity in regards to (a) binder and morphology factor, (b) graphite particle morphology, and (c) porosity

Figure 21 shows the conductivity in the anode microstructure. Figure 18a shows that there is no change in the conductivity of the microstructure as a result of change in the binder morphology. However, there is an increase in conductivity as the binder increases. This makes sense because one of the purposes of the secondary phase is to increase the conductivity as the addition of conductive additives like carbon black is to improve the conductivity of the active material. Additionally, it also makes sense that the morphology factor has no appreciable effect as there only needs to be the presence of the conductive additive to improve the conductivity. Like many of the other plots, the conductivity in Figure 21b appears to follow the form of a parabaloid where the largest conductivities appear when the basal plane and edge plane aspect ratios are lowest. It appears that the lowest conductivity is around where the basal plane aspect ratio is at 0.8 and the edge plane aspect ratio is at 0.7. So, while the conductivity generally decreases as the particle morphology increases, there is an increase in conductivity once the particle reaches a certain point and becomes rounder and thicker. In Figure 21c, increasing the porosity of the structure shows that there will be a largely linear decrease in the conductivity. As the porosity increases, there is typically a decrease in the volume percentage of the active material and secondary phase.

Figure 22 shows the tortuosity in the anode microstructure. Figure 22a doesn’t appear to show any particular trend in regards to the addition of binder as the tortuosity actually decreases at low morphology factors while the tortuosity increases at high morphology factors. However, increasing the morphology factor does appear to cause the tortuosity to increase. This makes sense as increasing the morphology factor leads to more self-deposition which in turn can cause the binder to deposit higher on itself and possibly block pathways in the porous volume. In Figure 22b, it appears that increasing the edge plane aspect ratio will largely decrease the tortuosity of the particle across all values of the basal plane aspect ratio. While the tortuosity has its highest values where the basal plane is at its roundest and the edge plane is thinnest. In Figure 19c, the tortuosity appears to have an exponential decrease as the porosity increases. This makes sense as increasing the porosity allows for more open space for ions to transport through.

For the thermo-electrochemical characterization, the three most important properties determined in this section are the interfacial area between the active material and the porous phase, or known as the active area, the conductivity, and the tortuosity. These properties are all necessary properties in the calculation of the governing equations that will be introduced in the next chapter.

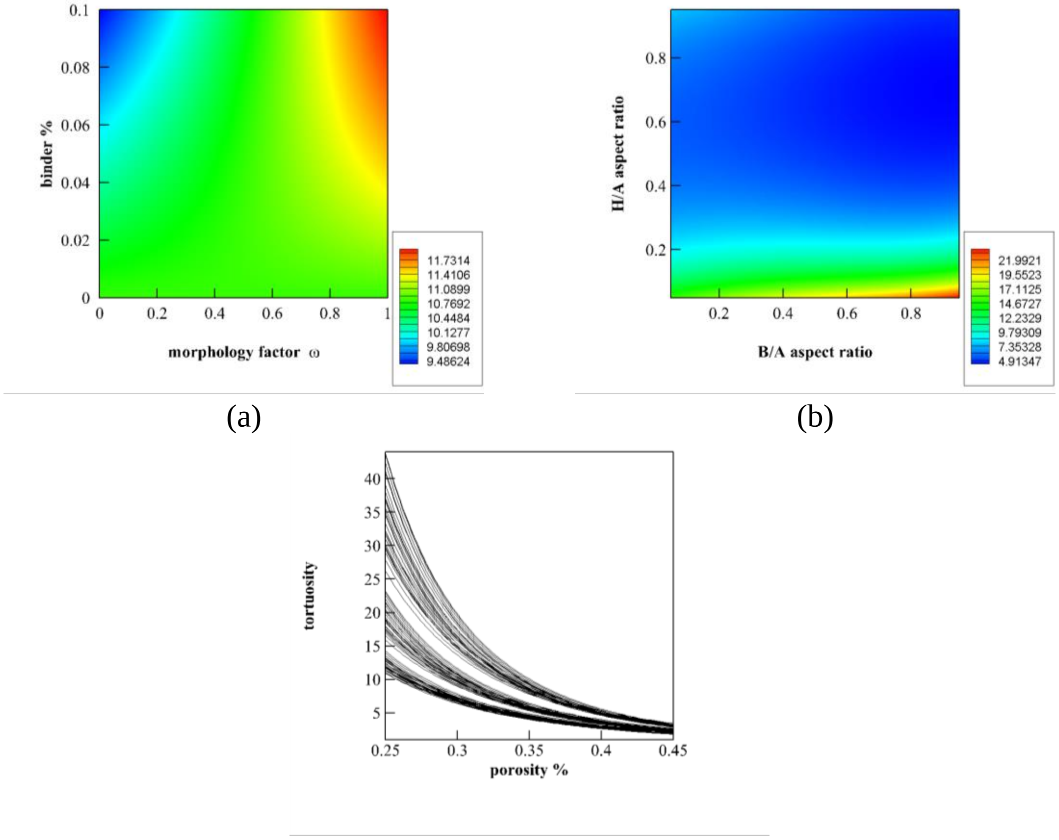

(a) (b)

(c)

Figure 22. Anode Tortuosity in regards to (a) binder and morphology factor, (b) graphite particle morphology, and (c) porosity

3.6 Microstructural Limitations

Now that the correlations have been found, it is important to understand how those correlations and how active area, porosity, and the active area relate to the limitations of the electrode. Two terms, N_{ohmic} and $N_{kinetic}$, can be defined that give an understanding of how tortuosity and active area affect the pore phase transport resistance and the kinetic overpotential, respectively. These terms are defined below:

$$N_{ohmic} = 1 - \frac{\varepsilon}{\tau}$$

$$N_{kinetic} = 1 - \frac{a}{a^{th}}$$

N_{ohmic} defines the pore phase transport resistance. This means that it shows how much of a negative effect the tortuosity has on an electrode. So, the higher the tortuosity, the higher the value of N_{ohmic}. This shows that the electrode is more limited ohmically as the transport through the porous phase is slower due to the higher tortuosity. $N_{kinetic}$ shows the kinetic overpotential of the electrode. This value is affected by the active area of the electrode. The lower the active area, the more kinetically limited the electrode is because the lower the active area, the smaller the area where Li-ions can react at.

In Figure 23, N_{ohmic} and $N_{kinetic}$ are shown for the cathode as the active material weight fraction is increased with regards to the morphology factor and porosity. Initially, it can be seen that $N_{kinetic}$ is much higher for all values while $N_{kinetic}$ is not as significant of a factor. However, as the weight fraction increases, it can be seen that

$N_{kinetic}$ decreases because the increase of active material causes an increase in active area. This addition of active material does lead to a tradeoff since N_{ohmic} increases since the tortuosity increases and becomes the limiting factor instead. Typically, there is a tradeoff between active area and tortuosity but it can't be seen what effect this tradeoff has on performance with just this.

In Figure 24, N_{ohmic} and $N_{kinetic}$ are shown for the anode. In the anode, unlike the cathode, the particle shape is an important area to investigate so rather than investigating the increase of the active material, the basal plane ratio is investigated instead. Initially, for a round particle with b/a of 1.0, N_{ohmic} is very high for all porosities and values of h/a and thus indicates that a round particle will cause ohmic limitations related to tortuosity. However, $N_{kinetic}$ has a distribution that shows there are only kinetic limitations for low h/a ratios but is not kinetically limited at higher h/a ratios which indicates that the active area is low at low h/a ratios. Now, as the basal plane ratio decreases and the shape goes from round to more oval, there is no significant changes in the ohmic limitations as N_{ohmic} stays high. However, $N_{kinetic}$ actually decreases for most values of h/a which indicates that the active area increases as b/a decreases. So it can be seen that the increase of active material causes a tradeoff between the tortuosity and active area that shifts the effect of $N_{kinetic\ to}$ N_{ohmic} and leads to ohmic limitations related to the pore phase transport. With the particle shape of the anode, the tortuosity is always a problem and will always have high pore phase transport resistance while the kinetic overpotential decreases as the particle shape becomes less round. So ideally, an oval graphite particle will have the least limitations.

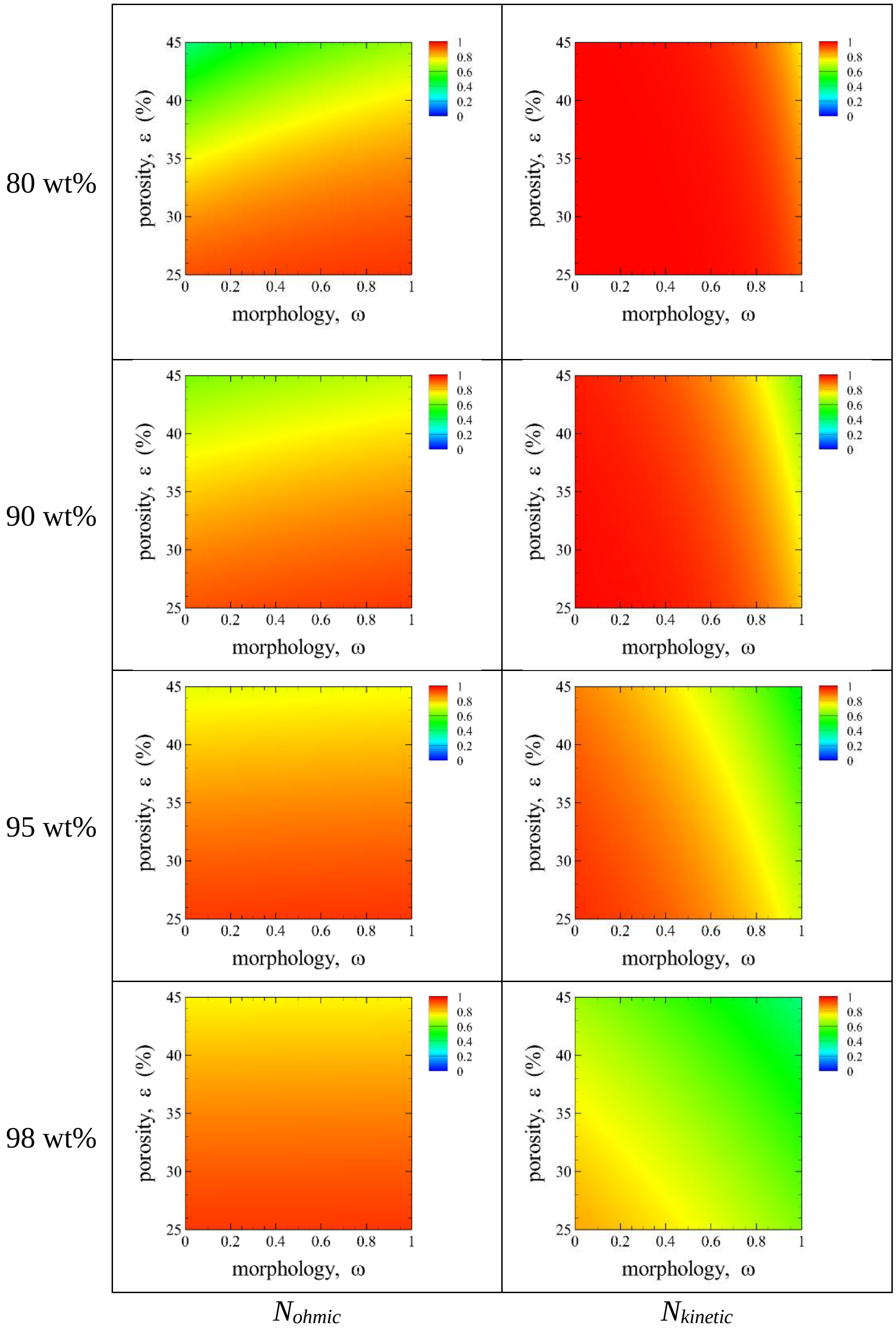

Figure 23. Cathode microstructure limitations in regards to active material weight fraction

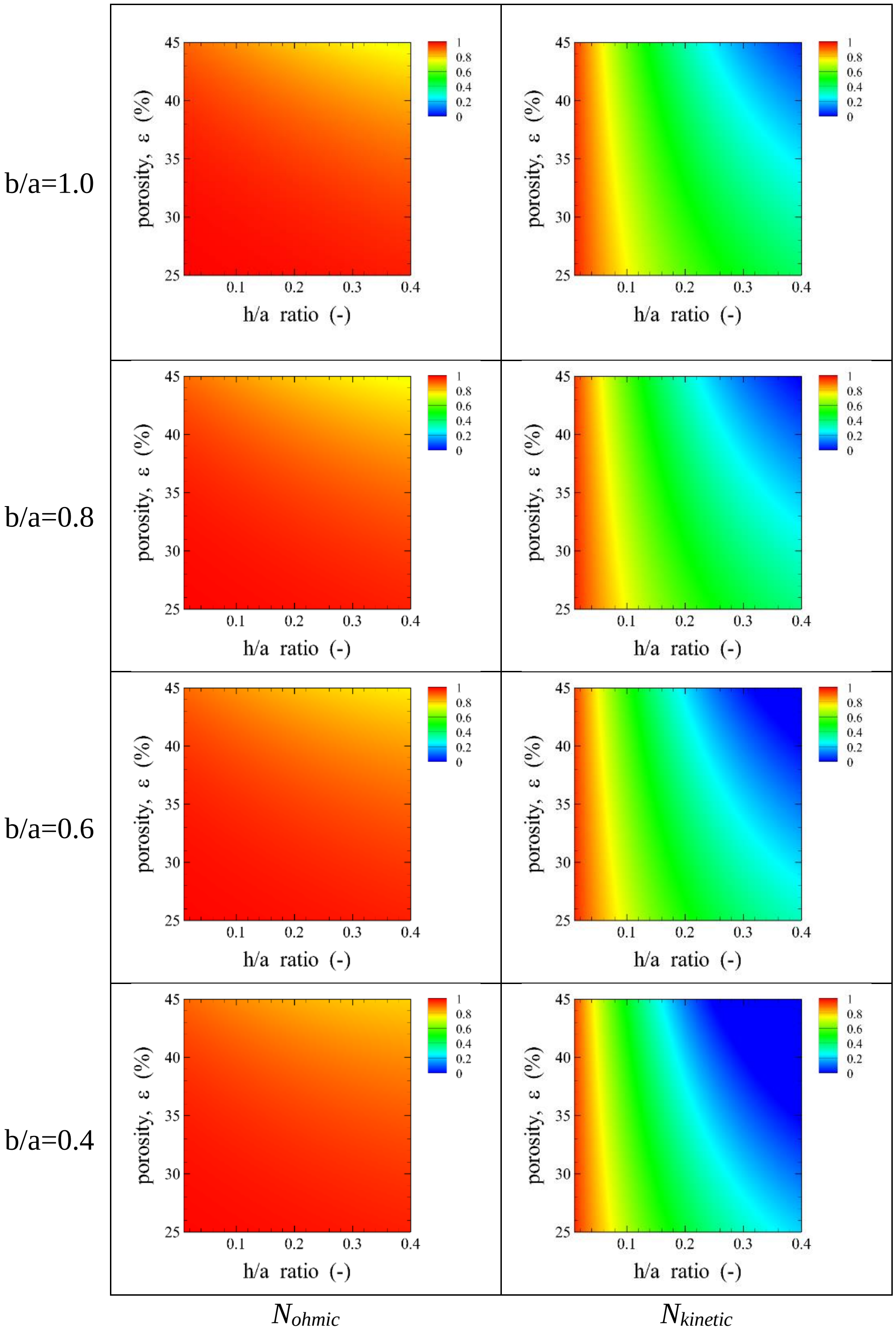

Figure 24. Anode Microstructure Limitations in regards to particle shape

4. THERMO-ELECTROCHEMICAL CHARACTERIZATION

4.1 Governing Equations

An electrochemical-thermal coupled model was developed to determine the influence of thermal effects on Li-ion batteries in regards to the changes in the electrode microstructure. Ji et al. has done some work investigating the thermal effects but without considering the complex nature of the electrode microstructures. The electrochemical-thermal coupled model used takes into account the nuances of the microstructure involved. This means that the extracted correlations for the active area, conductivity, and tortuosity developed from the microstructure generation will be used, in addition to a set of governing equations, to model the effects of particle and microstructural morphology in the anode and cathode electrodes and how they will affect thermal and electrochemical performance in a Li-ion cell.

The thermos-electrochemical governing equations include the Butler-Volmer equation, the species conservation in the solid phase, the species conservation in the electrolyte phase, the charge conservation in the solid phase, the charge conservation in the electrolyte phase, and the conservation of energy in the Li-ion cell.

The Butler-Volmer equation is a way to describe the electrochemical reaction kinetics and how the current depends on the applied potentials due to the cathodic and anodic reactions in each electrode. The equation is shown below:

$$J = a_c k_c \left\{ C_c \left(C_c^{max} - C_c \right) C_e \right\} \left\{ \exp\left({F\eta}/{2RT} \right) - \exp\left(-{F\eta}/{2RT} \right) \right\}$$

The species conservation in the solid phase is based on Fick's law of diffusion and results from performing a mass balance while considering the active material particles radially as the particles are either spherical or cylindrical platelets. This governing equation can be used to solve the lithium transport inside of the active material particles. It should be noted that the species conservation of the graphite particle and NMC particle will be different because of the difference in the particle shape. The boundary conditions indicate that the species flux occurs at the particle surface while there is no flux at the particle center. The species conservation of a graphite particle in regards to the platelet particle:

$$\frac{\partial C_a}{\partial t} = \mathcal{D}_a \frac{\partial^2 C_a}{\partial z^2}$$

$$-\mathcal{D}_a \frac{\partial C_a}{\partial z} = {J}/{a_a^{th} F}$$

The species conservation of an NMC particle with regards to the spherical particle:

$$\frac{\partial C_c}{\partial t} = \frac{\mathcal{D}_c}{r^2} \frac{\partial}{\partial r}\left(r^2 \frac{\partial C_c}{\partial r} \right)$$

$$-\mathcal{D}_c \frac{\partial C_c}{\partial r} = {J}/{a_c^{th} F}$$

Similarly to the species conservation in the solid phase, the species conservation in the electrolyte phase involves Fick's law of diffusion. However, this governing equation involves the diffusion of lithium ions inside the electrolyte rather than the active material particles. Of note is that D_e^{eff} is the effective diffusion rate of the lithium ions in the electrolyte. The volumetric current density j is given as the multiple of the current density and the specific active surface area of the electrode. The interfacial area comes from the previously determined active area between the porous space and the active material area from the microstructure generation.

$$\varepsilon \frac{\partial C_e}{\partial t} = \frac{\partial}{\partial x}\left(\mathcal{D}_e \frac{\varepsilon}{\tau} \frac{\partial C_e}{\partial x} \right) + \left(\frac{1-t_+}{F} \right) J$$

The charge conservation in the solid phase comes from Ohm's law. Φ_s is the solid phase potential, and σ_s^{eff} is the effective conductivity from the microstructure generation.

$$\sigma^{eff} \frac{\partial^2 \phi_s}{\partial x^2} = J$$

Like the solid phase, the electrolyte phase is also conductive. Therefore, a charge conservation equation is also needed. The electrolyte will allow for charged particles to flow as well so the diffusion of charged particles is also included. In the case of the electrolyte, the charge carriers are ions rather than electrons. Charge conservation in the electrolyte phase involves the charge transport in the electrolyte phase. This governing equation is driven by the electrolyte potential ϕ_e and ionic concentration $c_{e.}$

$$\frac{\partial}{\partial x}\left(\kappa \frac{\varepsilon}{\tau}\frac{\partial \phi_e}{\partial x}\right)+\frac{\partial}{\partial x}\left(\kappa_D \frac{\varepsilon}{\tau}\frac{\partial \ln C_e}{\partial x}\right)+J=0$$

The conservation of energy and heat transfer can be used to study the thermal effects of the Li-ion cell. A lumped thermal model can be used as the Biot number is low for Li-ion cells with typical external cooling conditions. The heat generation rate $\dot{Q}$ involves terms for reaction heat, reversible heat, and the joule heat. The reaction heat is the irreversible heat that occurs as a result of the electrochemical reaction. The reversible heat accounts for the change in entropy of the cell. Finally, the joule heating term refers to the heat produced as an electric current passes through a conductive material. It is essentially the heat caused by resistance in the cell. Then the sum of the three heating terms are integrated over the length of the cell and multiplied by the electrode area. Separate boundary conditions are used for different parts of the cell as needed.

$$mC_p \frac{dT_{cell}}{dt}=-hA\left(T-T_\infty\right)+\dot{Q}$$

$$\dot{Q}=A_{cs}\int_L \left\{\sigma^{eff}\nabla\phi_s\cdot\nabla\phi_s+\kappa\frac{\varepsilon}{\tau}\nabla\phi_e\cdot\nabla\phi_e+\kappa_D\frac{\varepsilon}{\tau}\nabla\phi_e\cdot\nabla\ln C_e+J\eta-JT\frac{\partial U}{\partial T}\right\}\mathrm{d}x$$

4.2 Coupled Electrochemical-Thermal Behavior

Figure 25 shows a representative discharge and temperature profile of an 18650 Li-ion cell at 1C under calorimetry conditions. For this cell, the anode and the cathode have the same porosity of 30 vol%. Table 8 shows the microstructural properties of the electrodes. What is notable about this is that the tortuosity and the active area of the anode are much higher than tortuosity and the active area of the cathode. This would indicate that the anode is more limited through ohmic means as high tortuosity means that the pore phase resistance is very high while the cathode is more limited kinetically as the lower active area indicates that there is less area for the ions to intercalate.

Table 8. Electrode Properties of an 18650 cell with electrodes of 30% porosity

	ε	τ	$a\,(\mathrm{m}^2/\mathrm{m}^3)$	$a\,(\mathrm{m}^2/\mathrm{m}^3)$
Anode	30%	10.8038	310476.2	661839.5
Cathode	30%	2.4552	4332	289577

Figure 26 shows the effect of cell discharge under adiabatic and isothermal conditions. For both conditions, the discharge rate is increased from 1C to 5C. Under adiabatic conditions, the temperature increases and the capacity and voltage decrease. Similarly, the voltage and temperature also decrease under isothermal conditions. However, because it is isothermal, the temperature stays the same. While the capacity and voltage both decrease, the effect of increasing C-rate is more significant under isothermal operations. The reason behind this is because at higher temperatures, the transport processes become more efficient and the capacity improves for the same C-rate. So since the temperature increases under adiabatic operations, the cell performs more efficiently and thus the capacity improves for the same C-rate compared to the isothermal cell where the improvements of higher temperatures do not occur.

Because the anode and cathode are ohmically or kinetically limited, it is necessary to identify how this affects the thermal behavior of the cell. Typically, joule heating is affected by the potential gradient in the solid phase, the potential gradient in the electrolyte phase, and the concentration gradient in the electrolyte phase. Then, these components are identified in the cathode, anode, and separator:

$$Q_{ohmic,anode} = A_{cs} \int_{L_{anode}} \left\{ \sigma_a \left(\frac{\partial \phi_a}{\partial x} \right)^2 + \kappa \frac{\varepsilon}{\tau} \left(\frac{\partial \phi_e}{\partial x} \right)^2 + \kappa_D \frac{\varepsilon}{\tau} \left(\frac{\partial \phi_e}{\partial x} \frac{\partial \ln C_e}{\partial x} \right) \right\} \mathrm{d}x$$

$$Q_{ohmic,cathode} = A_{cs} \int_{L_{cathode}} \left\{ \sigma_c \left(\frac{\partial \phi_c}{\partial x} \right)^2 + \kappa \frac{\varepsilon}{\tau} \left(\frac{\partial \phi_e}{\partial x} \right)^2 + \kappa_D \frac{\varepsilon}{\tau} \left(\frac{\partial \phi_e}{\partial x} \frac{\partial \ln C_e}{\partial x} \right) \right\} \mathrm{d}x$$

$$Q_{ohmic,separator} = A_{cs} \int_{L_{separator}} \left\{ \kappa \frac{\varepsilon}{\tau} \left(\frac{\partial \phi_e}{\partial x} \right)^2 + \kappa_D \frac{\varepsilon}{\tau} \left(\frac{\partial \phi_e}{\partial x} \frac{\partial \ln C_e}{\partial x} \right) \right\} \mathrm{d}x$$

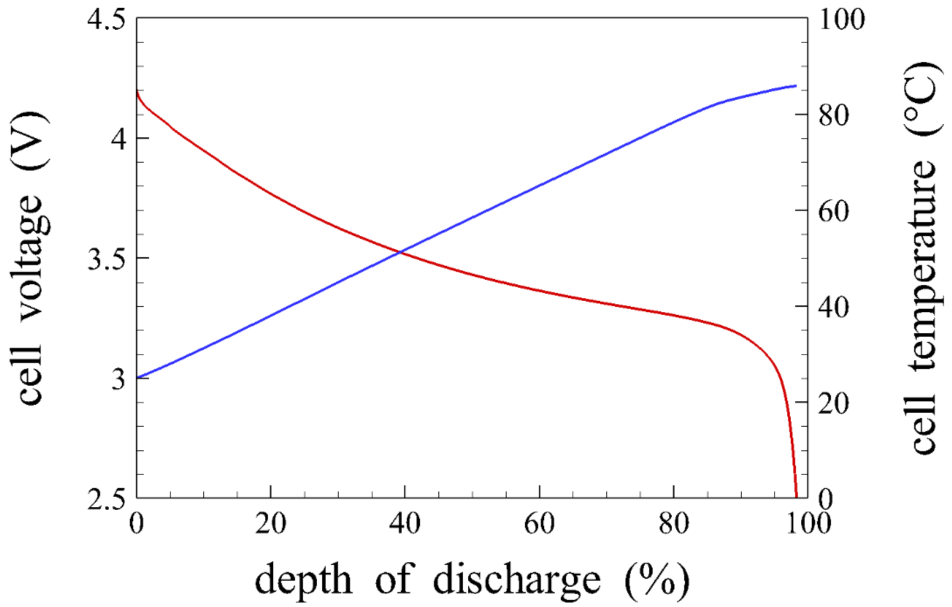

Figure 25. Electrochemical-thermal behavior of an 18650 Li-ion cell at 1C under calorimetry conditions

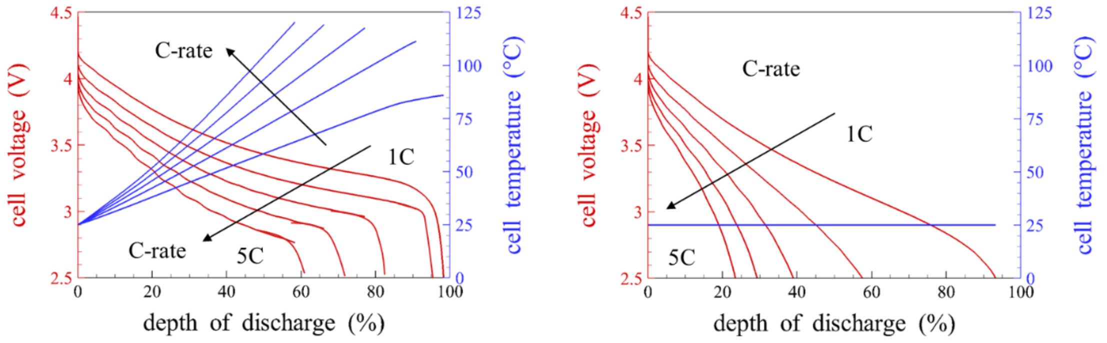

adiabatic operation

isothermal operation

(a) (b)

Figure 26. 18650 cell discharge with increasing C-rate under (a) adiabatic operation and (b) isothermal operation

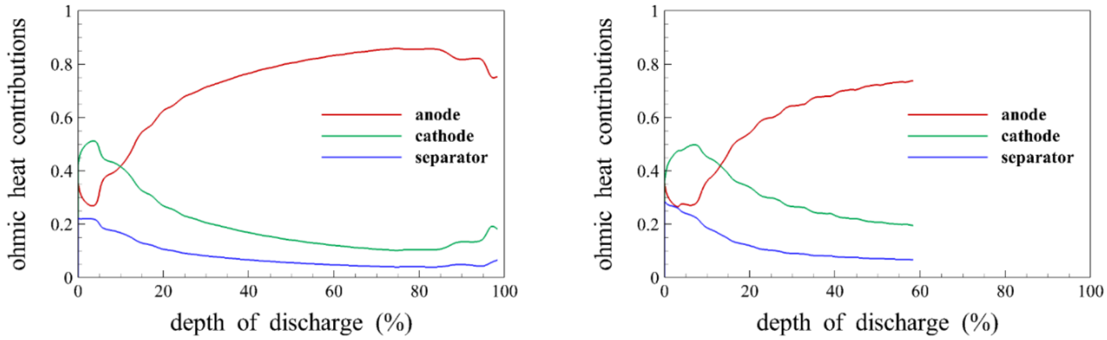

(a) (b)

Figure 27. Joule heat contributions from components of an 18650 cell at (a) 1C and (b) 5C

Notice that the anode and cathode both include all three components corresponding to the solid potential gradient, electrolyte potential gradient, and the electrolyte concentration gradient mentioned above. However, the separator does not include the solid potential gradient because there is not active material in the separator. The conductivity and the term $\frac{\varepsilon}{\tau}$, which relates to the N_{ohmic} term, have a significant role in the joule heating. Figure 27 shows N_{ohmic} at 1C and 5C as the cell discharges. It shows that the ohmic heat contribution of the anode is much higher than the ohmic heat contribution in the cathode and the separator. As the discharge rate increases, the concentration gradient increases as well due to higher transport resistance as the ions do not flow through the electrolyte phase fast enough. Another effect of increasing discharge rate is the increase in the electrolyte phase drop which leads to an additional toll on cell voltage, especially in the anode. This is largely expected from the knowledge that the anode has a much higher tortuosity than the cathode which leads to large ohmic losses. So, what can be concluded from this is that a higher tortuosity will lead to higher joule heating. Related to that, this means that the anode is a major source of joule heating.

Next, the reaction heating comes from the kinetics of the electrodes. So, similar to the joule heating, the reaction heat needs to be found for the anode and the cathode. However, since there is no active material in the separator, there will be no reaction heat occurring in the separator. So there is a Q_{kinetic} for the anode and the cathode:

$$Q_{kinetic,anode} = A_{cs} \int_{L_{anode}} J\eta_a \, \mathrm{d}x = A_{cs} \int_{L_{anode}} J\left(\phi_a - \phi_e - U_a\right) \mathrm{d}x$$

$$Q_{kinetic,cathode} = A_{cs} \int_{L_{cathode}} J\eta_c \, \mathrm{d}x = A_{cs} \int_{L_{cathode}} J\left(\phi_c - \phi_e - U_c\right) \mathrm{d}x$$

The kinetic heat is particularly dependent on the overpotential η. From the Butler-Volmer equation:

$$J \propto \left(ak\right)\sinh\left(\frac{F\eta}{2RT}\right)$$

This relation shows that the current density is proportional to the active area a, the reaction rate constant k_c, and the overpotential η. As the active area and reaction rate constant decrease, the overpotential will increase. So when the active area is low, there will be a large increase in the overpotential which then leads to an increase in the reaction heat of the electrode. Based on the electrode properties of the 18650 cell, this would suggest that the cathode is a major source of reaction heat. Figure 28, which shows $N_{kinetic}$ for 1C and 5C as an 18650 cell discharges, can confirm that the contributions from kinetic heating are much higher from the cathode than the anode and so, the cathode is responsible for major kinetic losses. Noticeably, the cathodic contribution is significantly higher than the anodic contribution. This is because the active area of the anode is roughly 700x greater than the active area of the cathode. It can then be concluded that low active area will lead to kinetic losses and reaction heating. Incidentally, this also means that the cathode is likely to be a significant source of reaction heat.

Figure 29 shows the overall heat contribution from each component of the cell. At 1C, the heat generation contribution from the joule and kinetic heating are similar while the entropic heating is fairly negligible as a whole. This indicates that the contributions from the anode and cathode are similar. However, as the C-rate increases to 5C, the kinetic contributions decrease and the heat generation is dominated by the joule heating. This makes sense as the kinetic reactions become more efficient at higher temperatures. As the C-rate increases, the temperature also increases and the electrode kinetics improve.

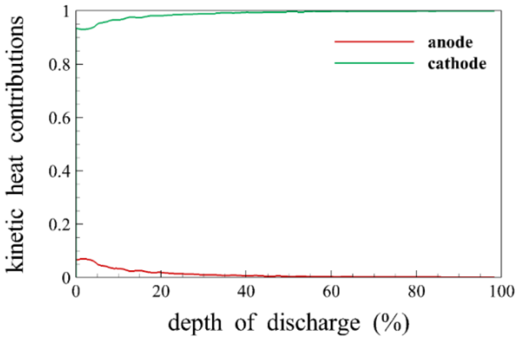

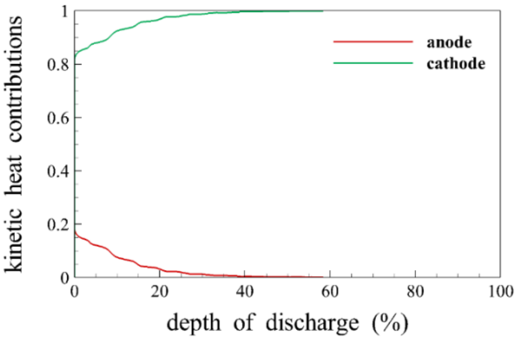

(a) (b)

Figure 28. Reaction heat contributions from components of an 18650 cell at (a) 1C and (b) 5C

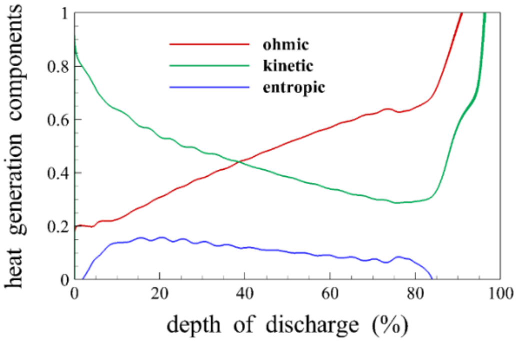

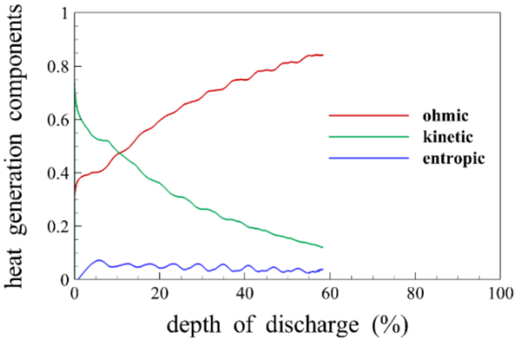

(a) (b)

Figure 29. Overall heat contributions from components of an 18650 cell at (a) 1C and (b) 5C

4.3 Thermo-Electrochemical Investigations

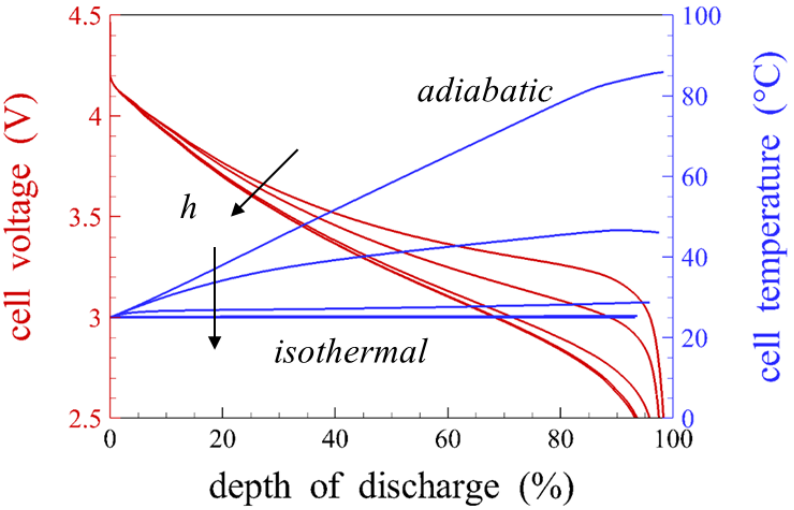

Figure 30. Effect of Ambient Convection

To determine the effect of electrode microstructures on the thermo-electrochemical performance, a number of investigations were done based on environmental cooling, cathode properties, and anode properties. The first investigation looks into the effect of ambient convection on the cell. This is done by increasing the convection coefficient *h* in the lumped capacitance model to determine the amount of heat lost to the ambient atmosphere. Figure 30 shows the effect of increasing the convection coefficient *h* from 0 to infinity. It can be seen that as *h* increases, the temperature, voltage, and capacity decrease. Additionally a convection coefficient of 0 essentially replicates ambient operations while a convection coefficient of infinity replicates isothermal operations.

As the temperature increases, the transport processes become more efficient and so the cell performance increases but when the temperature does not increase, the transport processes do not gain those benefits. This can be seen in Figure 31 that shows the heat generation contributions from joule/ohmic heating, kinetic/reaction heating, and entropic heat. As the convection coefficient increases, the average kinetic heat increases as well which corresponds to inefficient transport processes. So, for maximum capacity and average cell voltage are available under adiabatic cell operation. However, even though a cell may have the best electrochemical performance at adiabatic conditions, care should be taken as the thermal performance is at its worst as well and temperatures above 80 °C are susceptible to thermal runaway and may cause fires or explosions.

Then an investigation is done on the cathode porosity and the cathode particle size. These are two factors that can be readily changed in the manufacturing of cathodes. First, the effect of cathode porosity is studied by increasing the porosity from 25 vol% to 40 vol%. Figure 32 shows the electrochemical and thermal profiles of the cell with increasing porosity. It can be seen that increasing the cathode porosity will result in an increase in voltage and capacity while also decreasing the temperature as well. This is due to the fact that increasing the cathode porosity will also lead to a decrease in tortuosity as well. This results in a decrease in the transport resistance and a decline in the ohmic losses. Figure 33 shows the ohmic heat contributions for increasing porosities and it shows that the ohmic heat contributions from the cathode decrease as the porosity increases. So this results in more efficient transport as well as a significant decrease in heat generation. With this, increasing the cathode porosity is an effective way of increasing the electrochemical and thermal performance of a cell.

Secondly, the particle radius of the cathode active material was investigated. Figure 34 shows the effect of increasing the particle radius of the NMC. The effect of particle radius is not very significant as there is no change in the capacity of the cell. However, there is a small decrease in voltage and increase in the temperature. While increasing the particle size improves the active area of the cathode a_c, the reaction rate constant k_c is still quite poor. In Figure 35, the kinetic heat contribution shows that the majority of the kinetic heat contributions comes from the cathode even with a larger active area and the cathodic kinetic heat contributions only continue to grow as the particle radius increases. This shows that the active area ratio $a_a k_a / a_c k_c$ is still significantly in the favor of the anode and further shows that the cathode is a major source of kinetic losses regardless of changes in the particle size. However, reduction in particle radius will lead to improvements in the temperature and voltage even if those results are relatively minor.

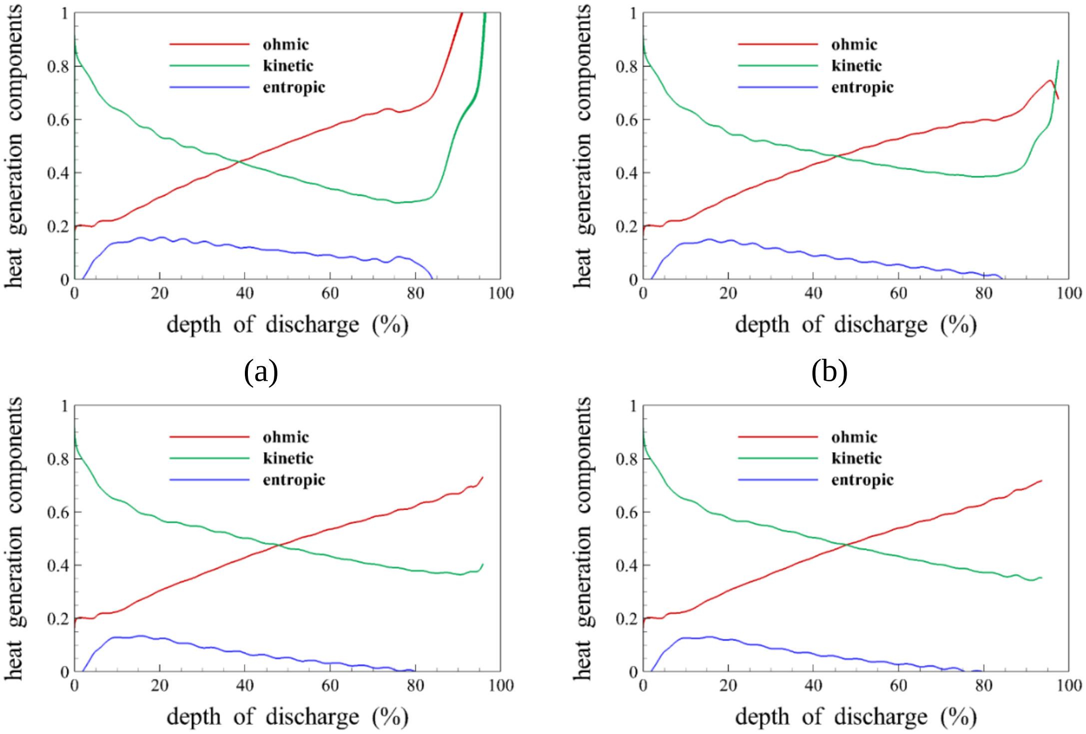

(a) (b)

(c) (d)

Figure 31. Heat Generation contributions for convection coefficients of (a) 0, (b) 10, (c) 100, and (d) →∞

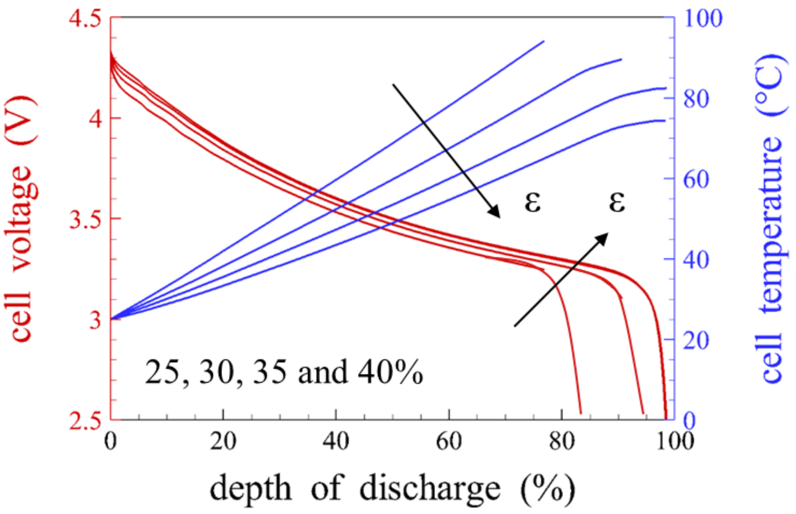

Figure 32. Effect of Cathode Porosity

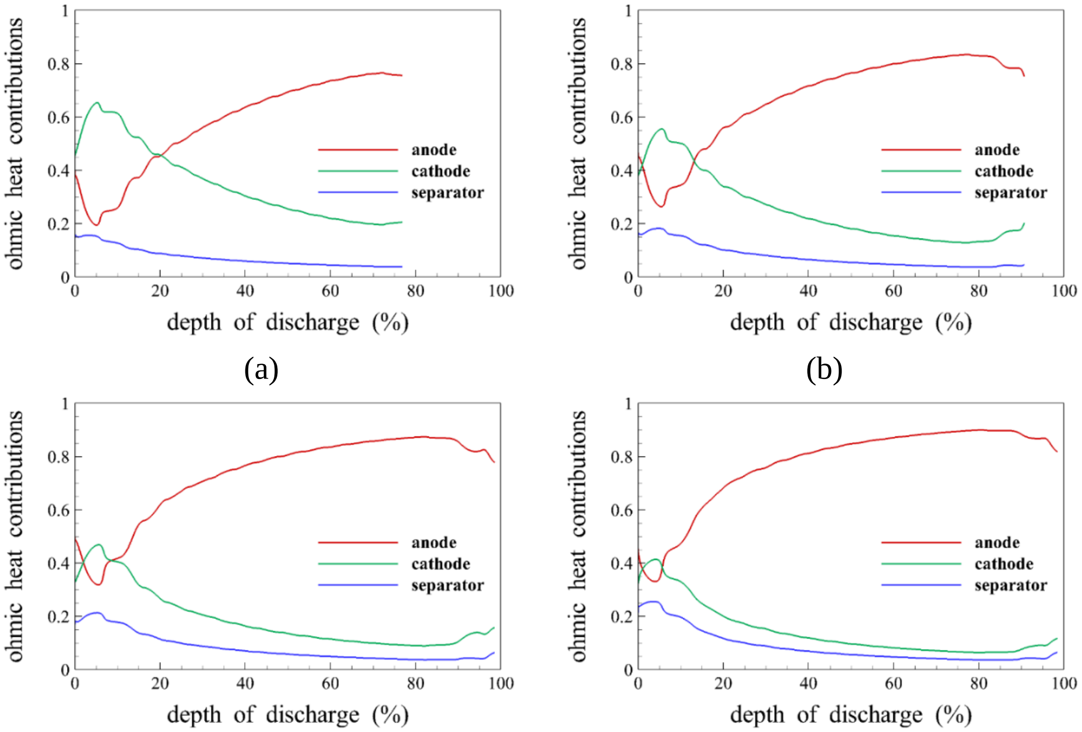

(a) (b)

(c) (d)

Figure 33. Ohmic heat contributions for cathode porosities of (a) 25%, (b) 30%, (c) 35%, and (d) 40%

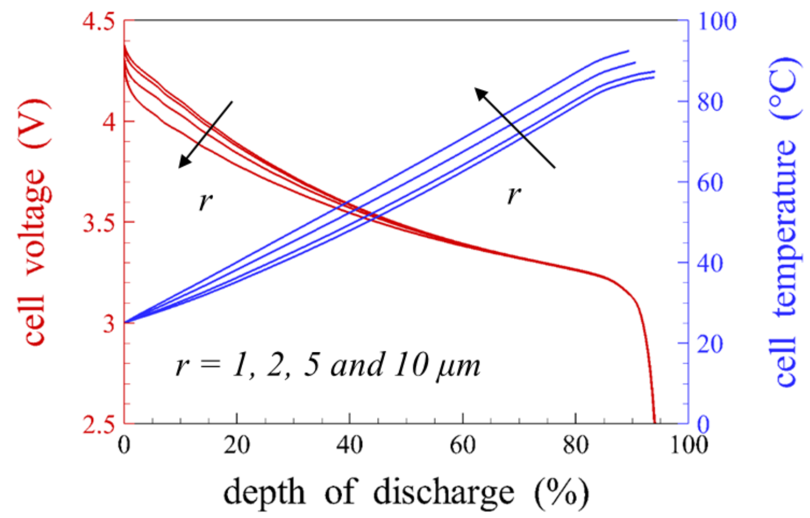

Figure 34. Effect of Cathode Particle Radius

Then the effect of adjusting the anode is investigated. Like the cathode, two investigations are done on the anode porosity and the anode particle. In the case of the particle, the anode's particle shape is investigated instead of the particle size. Figure 36 shows the effect of increasing anode porosity on the thermal and electrochemical performance of the cell. Increasing the porosity results in a decrease in temperature. Increasing the porosity also leads to an increase in voltage, however there is also a decrease in the capacity. This is because the Li is stored in the anode at the beginning of discharge. By increasing the porosity, this leads to a decrease in the total Li stored in the anode and thus a reduced total capacity in the cell. Additionally, the increase in porosity also leads to a decrease in tortuosity which then leads to better pore transport. Figure 37 shows the ohmic heat contributions, which is directly related to the tortuosity. This decrease in tortuosity will then lead to a decrease in the ohmic losses in the anode and as the porosity increases, the ohmic heat contributions from the anode decreases as well. This decrease is fairly significant to the point that the main source of ohmic heating shifts to the cathode at higher anodic porosities.

Finally, an investigation of the effect of anode particle aspect ratio is done. Figure 38 shows an example of the graphite particle structure. There are two aspect ratios that have been mentioned, the b/a ratio and the h/a ratio. In this investigation, the h/a ratio will be considered. In Figure 39, two h/a ratios of 0.2 and 0.3 are looked at. As h/a increases, the capacity and voltage increases. There is also an additional decrease in the temperature. As the h/a ratio increases, the tortuosity of the porous phase decreases which then leads to improved transport and efficient cell operation. This can also be seen in Figure 40 that increasing the h/a ratio's decrease in tortuosity leads to a decrease in the ohmic losses and a decrease in the ohmic heat contributions. Adjusting these electrode properties to tune the active area and tortuosity can lead to major improvements in the cell performance.

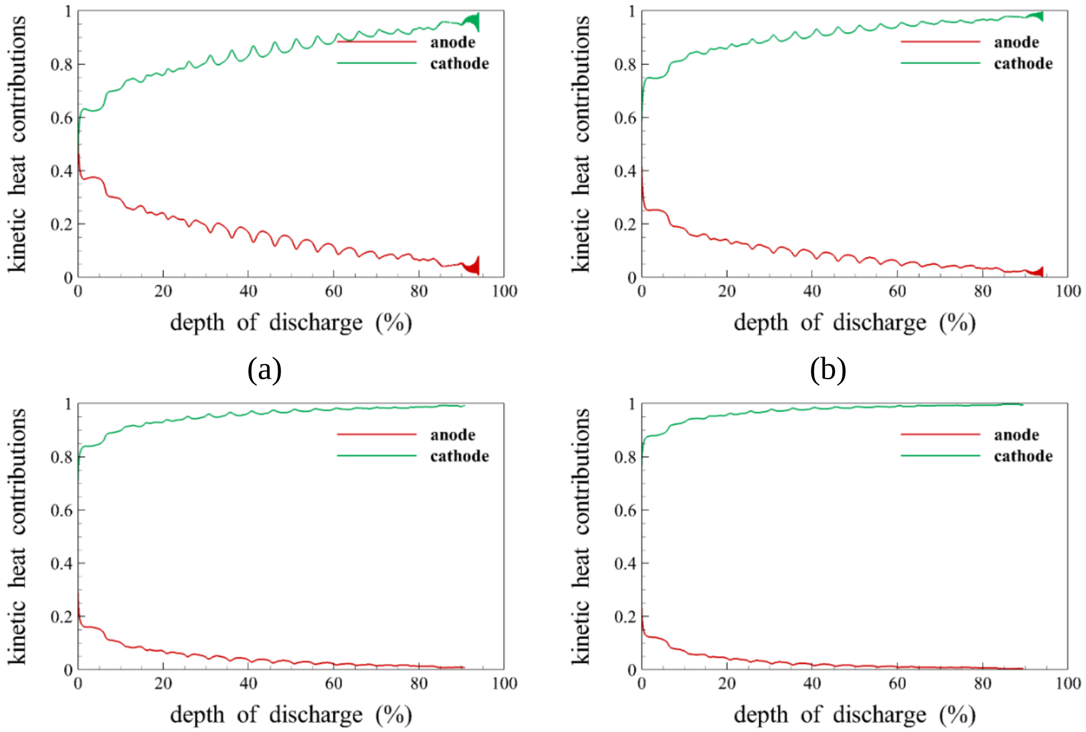

(a) (b)

(c) (d)

Figure 35. Kinetic Heat Contributions for particle radius of (a) 1 µm, (b) 2 µm, (c) 5 µm, (d) 10 µm

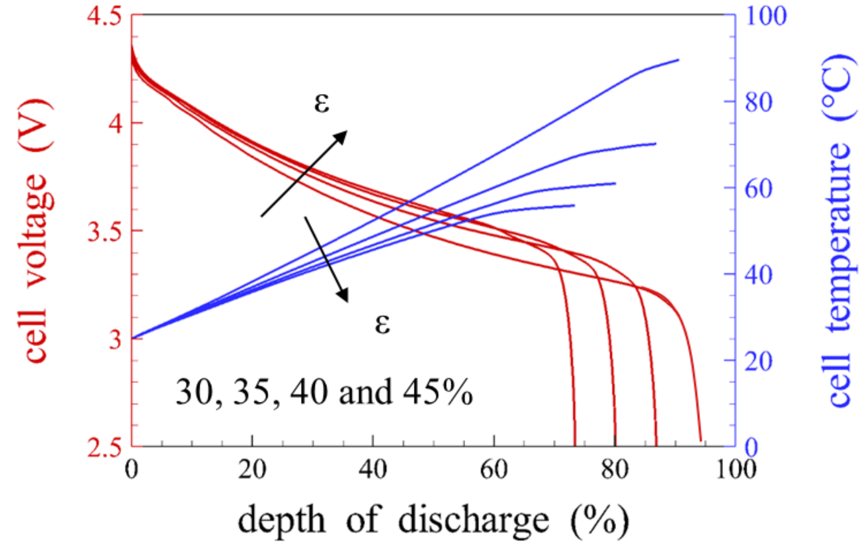

Figure 36. Effect of Anode Porosity

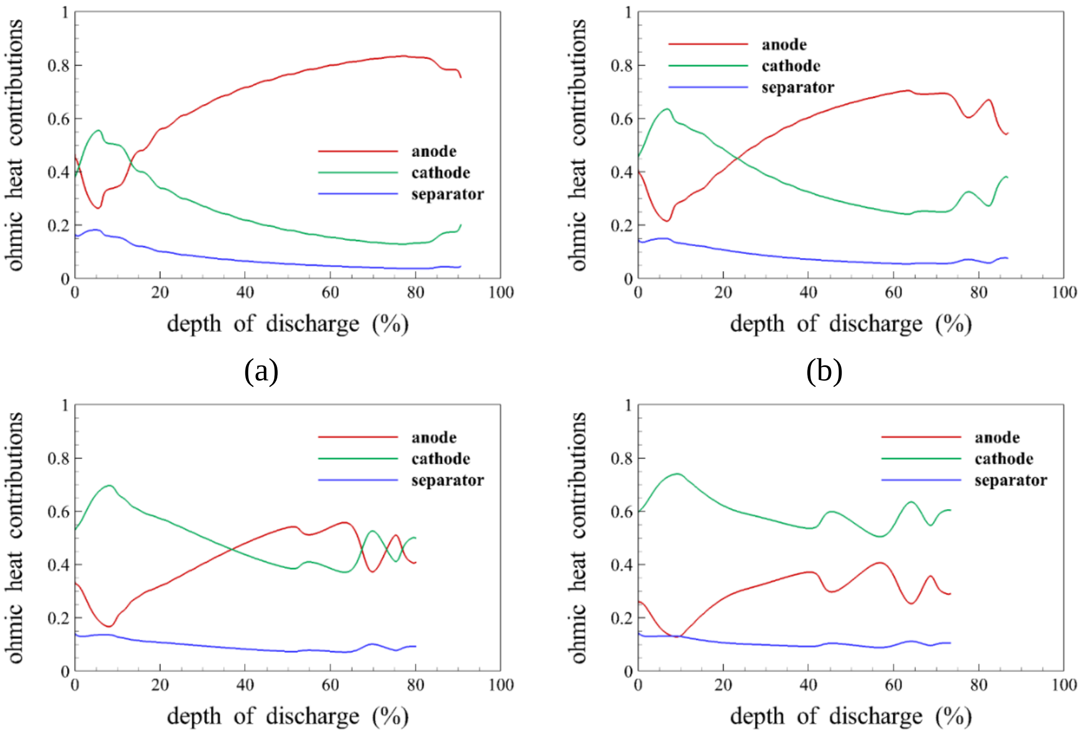

(a) (b)

(c) (d)

Figure 37. Ohmic heat contributions for anode porosity of (a) 30%, (b) 35%, (c) 40%, (d) 45%

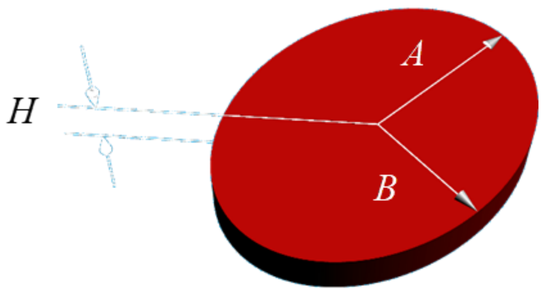

Figure 38. Anode platelet particle with dimensions

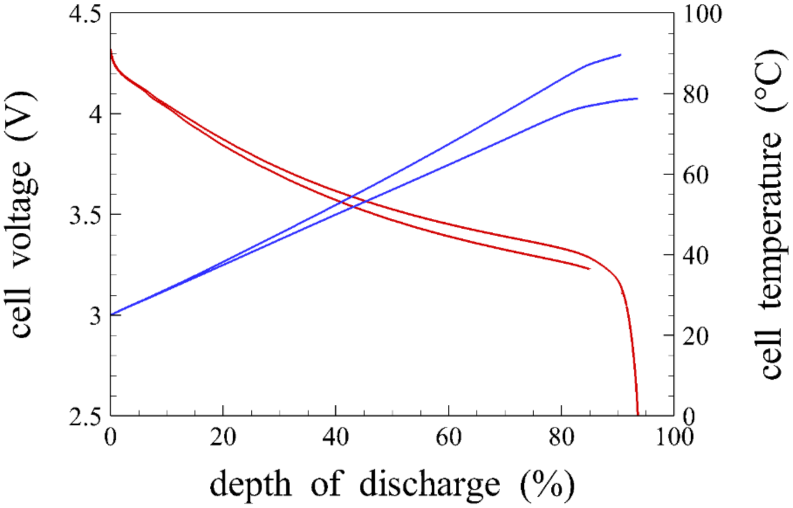

Figure 39. Effect of Anode Particle Aspect Ratio

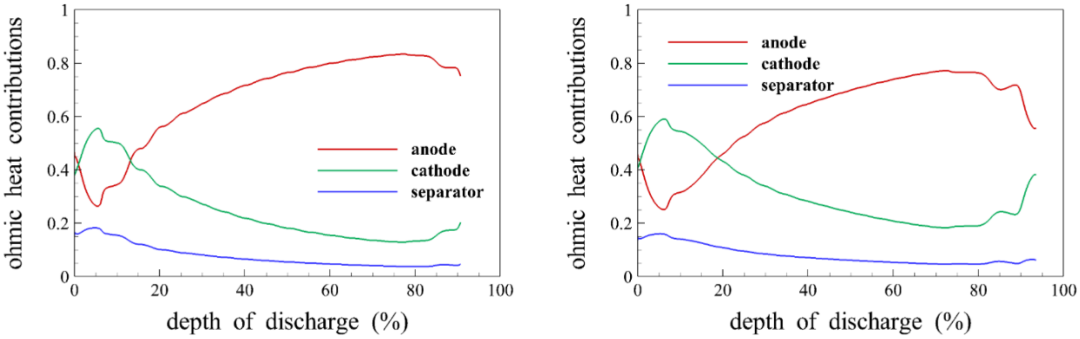

(a) (b)

Figure 40. Ohmic heat contributions for anode aspect ratio of (a) 0.2, (b) 0.3

5. CONCLUSIONS AND FURTHER RESEARCH

The thorough microstructure generation performed here has allowed for the development of good functional dependencies that can be used to model the active area, conductivity, and tortuosity for a wide array of microstructure morphologies for an NMC cathode and graphite anode. Further work can be done to determine a similar fit to other chemistries like LCO in the future. This would simplify future microstructural investigations as this provides an accurate evaluation of important microstructural properties in the anode and cathode.

From the thermo-electrochemical characterization scenarios performed and the characterization of the thermal behavior, it can be seen that changes in the electrodes have a significant effect on both the cell capacity and temperature rise. For an anode and a cathode with the same porosity, it was determined that an anode will have a much higher tortuosity than a cathode while also having a significantly higher active area as well. This difference leads to differences in the heat contributions from the anode and the cathode. It was determined that high tortuosity will head to higher heating contribution from ohmic heat, thus it can be inferred that the anode is a major source of ohmic heating, while having low active area will lead to higher kinetic heating contributions so it can be considered that the cathode is a major source of kinetic heat. So, adjusting the cathode and anode to maximize the active area and minimize the tortuosity will lead to the best performance electrochemically and thermally. However, it should be noted that temperatures above 80 °C will likely lead to thermal runaway so that needs to be accounted for as well. Adjusting the tortuosity and active area by making modifications in the microstructure allows for the tuning of different sources of heat generation.

In the future, further research can be done here to improve the model developed. For example, thermal runaway and the causes of thermal runaway was not considered here so exploring the effects of side reactions in the electrode microstructure and look into how they affect the onset of thermal reactions that lead to thermal runaway will be one area of research that could be explored. Additionally, heat generation and the rise in temperature will also cause thermal stresses so exploring the effect of heat generation on mechanical stresses and how those stresses affect the microstructure is also an important area of work as well. Then coupling all of these factors will lead to a comprehensive model of the effect on electrode microstructure on the thermo-electrochemical performance of Li-ion microstructures.

REFERENCES

[1] Gogotsi, Y., and Simon, P., 2011, "True Performance Metrics in Electrochemical Energy Storage," Science, AAAS, pp. 917-918.

[2] Goodenough, J. B., and Park, K.-S., 2013, "The Li-Ion Rechargeable Battery: A Perspective," Journal of the American Chemical Society, 135, pp. 1167-1176.

[3] Smith, K. A., Rahn, C. D., and Wang, C.-Y., 2007, "Control oriented 1D electrochemical model of lithium ion battery," Energy Conversion and Management, 48, pp. 2565-2578.

[4] Xu, W., Wang, J., Ding, F., Chen, X., Nasybulin, E., Zhangad, Y., and Zhang, J.-G., 2014, "Lithium metal anodes for rechargeable batteries," Energy & Environmental Science, 7, pp. 513-537.

[5] Li, H., Wang, Z., Chen, L., and Huang, X., 2009, "Research on Advanced Materials for Li-ion Batteries," Advanced Materials, 21, pp. 4593-4607.

[6] Tarascon, J.-M., and Armand, M., 2001, "Issues and challenges facing rechargeable lithium batteries," Nature, 414, pp. 359-367.

[7] Pasquier, A. D., Plitz, I., Menocal, S., and Amatucci, G., 2003, "A comparative study of Li-ion battery, supercapacitor and nonaqueous asymmetric hybrid devices for automotive applications," Journal of Power Sources, 115, pp. 171-178.

[8] Zhang, S. S., 2006, "A review on electrolyte additives for lithium-ion batteries," Journal of Power Sources, 162, pp. 1379-1394.

[9] Jalkanen, K., Karppinen, J., Skogstrom, L., Laurila, T., Nisula, M., and Vuorilehto, K., 2015, "Cycle aging of commercial NMC/graphite pouch cells at different temperatures," Applied Energy, 154, pp. 160-172.

[10] Aurbach, D., 2000, "Review of selected electrode–solution interactions which determine the performance of Li and Li ion batteries," Journal of Power Sources, 89, pp. 206-218.

[11] Whitehead, A. H., and Schreiber, M., 2005, "Current Collectors for Positive Electrodes of Lithium-Based Batteries," Journal of The Electrochemical Society, 152(11), pp. A2105-A2113.

[12] Wang, Y., Liao, H., Wang, J., qian, X., Zhu, Y., and Cheng, S., 2013, "Effects of Current Collectors on Electrochemical Performance of FeS_2 for Li-ion Battery," International Journal of Electrochemical Science, 8, pp. 4002-4009.

[13] Liu, D. X., Cao, L. R., and Co, A. C., 2016, "Demonstrating the Feasibility of Al as Anode Current Collector in Li-Ion Batteries via In Situ Neutron Depth Profiling," Chemistry of Materials, 28, p. 556−563.

[14] Myung, S.-T., Hitoshia, Y., and Sun, Y.-K., 2011, "Electrochemical behavior and passivation of current collectors in lithium-ion batteries," Journal of Materials Chemistry, 21, pp. 9891-9911.

[15] Jeffrey W. Braithwaite, Angelo Gonzales, Ganesan Nagasubramanian, Samuel J. Lucero, Diane E. Peebles, James A. Ohlhausen, and Cieslak, W. R., 1999, "Corrosion of Lithium-Ion Battery Current Collectors," Journal of The Electrochemical Society, 146(2), pp. 448-456.

[16] Etacheri, V., Marom, R., Elazari, R., Salitra, G., and Aurbach, D., 2011, "Challenges in the development of advanced Li-ion batteries: a review," Energy & Environmental Science, 4, pp. 3243-3262.

[17] Doeff, M. M., 2013, "Battery Cathodes," Batteries for Sustainability, R. J. Brodd, ed., Springer, New York.

[18] Goodenough, J. B., 2013, "Battery Components, Active Materials for," Batteries for Sustainability, R. J. Brodd, ed., Springer, New York.

[19] Zhang, X., Chung, M., Kim, H., Wang, C.-W., and Sastry, A. M., 2011, "Mechanics of Battery Cells and Materials," Handbook of Battery Materials, C. Daniel, and J. O. Besenhard, eds., Wiley-VCH, Weinheim, Germany.

[20] Jianchao Chen, Jianyong Liu, Yue Qi, Tao Sun, and Li, X., 2013, "Unveiling the Roles of Binder in the Mechanical Integrity of Electrodes for Lithium-Ion Batteries," Journal of The Electrochemical Society, 160(9), pp. A1502-A1509

[21] G. Liu, H. Zheng, S. Kim, Y. Deng, A. M. Minor, X. Song, and Battaglia, V. S., 2008, "Effects of Various Conductive Additive and Polymeric Binder Contents on the Performance of a Lithium-Ion
Composite Cathode," Journal of The Electrochemical Society, 155(12), pp. A887-A892.

[22] Languang Lu, Xuebing Han, Jianqiu Li, Jianfeng Hua, and Ouyang, M., 2013, "A review on the key issues for lithium-ion battery management in electric vehicles," Journal of Power Sources, 226, pp. 272-288.

[23] Doughty, D., and Roth, E. P., 2012, "A General Discussion of Li Ion Battery Safety," Interface, The Electrochemical Society.

[24] Spotnitz, R., and Franklin, J., 2003, "Abuse behavior of high-power, lithium-ion cells," Journal of Power Sources, 113, pp. 81-100.

[25] Dillon, S. J., and Sun, K., 2012, "Microstructural design considerations for Li-ion battery systems," Current Opinion in Solid State and Materials Science, 16, pp. 153-162.

[26] Wiedemann, A. H., Goldin, G. M., Barnett, S. A., Zhu, H., and Kee, R. J., 2013, "Effects of three-dimensional cathode microstructure on the performance of lithium-ion battery cathodes," Electrochimica Acta, 88, pp. 580-588.

[27] Mohanty, D., Hockaday, E., Li, J., Hensley, D. K., Daniel, C., and III, D. L. W., 2016, "Effect of electrode manufacturing defects on electrochemical performance of lithium-ion batteries: Cognizance of the battery failure sources," Journal of Power Sources, 312, pp. 70-79.

[28] Nitta, N., Wu, F., Lee, J. T., and Yushin, G., 2015, "Li-ion battery materials: present and future," Materials Today, 18(5), pp. 252-264.

[29] Mizushima, K., Jones, P. C., Wiseman, P. J., and Goodenough, J. B., 1980, "LixCoO2 (0<x<-1): A new cathode material for batteries of high energy density," Materials Research Bulletin, 15(6), pp. 783-789.

[30] Gu, M., Belharouak, I., Zheng, J., Wu, H., Xiao, J., Genc, A., Amine, K., Thevuthasan, S., Baer, D. R., Zhang, J.-G., Browning, N. D., Liu, J., and Wang, C., 2012, "Formation of the spinel phase in the layered composite cathode used in li-Ion batteries," ACS Nano, 7(1), pp. 760-767.

[31] Wagner, R., Preschitschek, N., Passerini, S., Leker, J., and Winter, M., 2013, "Current research trends and prospects among the various materials and designs used in lithium-based batteries," Journal of Applied Electrochemistry, 43, pp. 481-496.

[32] Bo Xu, Danna Qian, Ziying Wang, and Meng, Y. S., 2012, "Recent progress in cathode materials research for advanced lithium ion batteries," Materials Science and Engineering R, 73, pp. 51-65.

[33] Chou, S.-L., Pan, Y., Wang, J.-Z., Liu, H.-K., and Dou, S.-X., 2014, "Small things make a big difference: binder effects on the performance of Li and Na batteries," Physical Chemistry Chemical Physics, 16, pp. 20347--20359.

[34] Xu, J., Chou, S.-L., Gu, Q.-f., Liu, H.-K., and Dou, S.-X., 2013, "The effect of different binders on electrochemical properties of LiNi1/3Mn1/3Co1/3O2 cathode material in lithium ion batteries," Journal of Power Sources, 225, pp. 172-178.

[35] Wu, Q., Seonbaek Ha, Jai Prakash, Dennis W. Dees, and Lu, W., 2013, "Investigations on high energy lithium-ion batteries with aqueous binder," Electrochimica Acta, 114, pp. 1-6.

[36] Doberdò, I., Löffler, N., Laszczynski, N., Cericola, D., Penazzi, N., Bodoardo, S., Kima, G.-T., and Passerinia, S., 2014, "Enabling aqueous binders for lithium battery cathodes e Carbon coating of aluminum current collector," Journal of Power Sources, 248, pp. 1000-1006.

[37] Loeffler, N., Zamory, J. v., Laszczynski, N., Doberdo, I., Kim, G.-T., and Passerini, S., 2014, "Performance of LiNi1/3Mn1/3Co1/3O2/graphite batteries based on aqueous binder," Journal of Power Sources, 248, pp. 915-922.

[38] Spahr, M. E., Goers, D., Leone, A., Stallone, S., and Grivei, E., 2011, "Development of carbon conductive additives for advanced lithium ion batteries," Journal of Power Sources, 196, pp. 3403-3413.

[39] Chen, Y.-H., Wang, C.-W., Liu, G., Song, X.-Y., V. S. Battaglia, and Sastry, A. M., 2007, "Selection of Conductive Additives in Li-Ion Battery Cathodes A Numerical Study," Journal of The Electrochemical Society, 154(10), pp. A978-A986.

[40] Xu, K., 2014, "Electrolytes and Interphases in Li-Ion Batteries and Beyond," Chemical Reviews, 114, pp. 11503-11618.

[41] Xu, K., Deveney, B., Nechev, K., Lam, Y., and Jow, T. R., 2008, "Evaluating LiBOB/Lactone Electrolytes in Large-Format Lithium-Ion Cells Based on Nickelate and Iron Phosphate," Journal of The Electrochemical Society, 155(12).

[42] Xu, K., 2004, "Nonaqueous Liquid Electrolytes for Lithium-Based Rechargeable Batteries," Chemical Reviews, 104, pp. 4303-4418.

[43] Wang, D. Y., Xia, J., Ma, L., Nelson, K. J., Harlow, J. E., Xiong, D., Downie, L. E., Petibon, R., Burns, J. C., Xiao, A., Lamanna, W. M., and Dahn, J. R., 2014, "A Systematic Study of Electrolyte Additives in Li[Ni1/3Mn1/3Co1/3]O2 (NMC)/Graphite Pouch Cells," Journal of The Electrochemical Society, 161(12), pp. A1818-A1827.

[44] Marks, T., Trussler, S., Smith, A. J., Xiong, D., and Dahn, J. R., 2011, "A Guide to Li-Ion Coin-Cell Electrode Making for Academic Researchers," Journal of The Electrochemical Society, 158(1), pp. A51-A57.

[45] Zheng, H., Li, J., Song, Z., Liu, G., and Battaglia, V. S., 2012, "A comprehensive understanding of electrode thickness effects on the electrochemical performances of Li-ion battery cathodes," Electrochimica Acta, 71, pp. 258-265.

[46] Singh, M., Kaiser, J., and Hahn, H., 2015, "Thick Electrodes for High Energy Lithium Ion Batteries," Journal of The Electrochemical Society, 162(7), pp. A1196-A1201.

[47] Singh, M., Kaiser, J., and Hahn, H., 2016, "Effect of Porosity on the Thick Electrodes for High Energy Density Lithium Ion Batteries for Stationary Applications," Batteries, 2(35).

[48] Wood III, D. L., Li, J., and Daniel, C., 2015, "Prospects for reducing the processing cost of lithium ion batteries," Journal of Power Sources, 275, pp. 234-242.

[49] Verma, P., Maire, P., and Novak, P., 2010, "A review of the features and analyses of the solid electrolyte interphase in Li-ion batteries," Electrochimica Acta, 55, pp. 6332-6341.

[50] An, S. J., Li, J., Daniel, C., Mohanty, D., Nagpure, S., and III, D. L. W., 2016, "The state of understanding of the lithium-ion-battery graphite solid electrolyte interphase (SEI) and its relationship to formation cycling*," Carbon, 2016, pp. 52-76.

[51] J. Vetter, Novak, P., Wagner, M. R., Veit, C., ̈ller, K.-C. M., Besenhard, J. O., Winter, M., Wohlfahrt-Mehrens, M., Vogler, C., and Hammouche, A., 2005, "Ageing mechanisms in lithium-ion batteries " Journal of Power Sources, 147, pp. 269-281.

[52] Zinth, V., Lüders, C. v., Hofmann, M., Hattendorff, J., Buchberger, I., Erhard, S., Rebelo-Kornmeier, J., Jossen, A., and Gilles, R., 2014, " Lithium plating in lithium-ion

batteries at sub-ambient temperatures investigated by in situ neutron diffraction," Journal of Power Sources, 271, pp. 152-159.

[53] Smart, M. C., and Ratnakumar, B. V., 2011, "Effects of Electrolyte Composition on Lithium Plating in Lithium-Ion Cells," Journal of The Electrochemical Society, 158(4), pp. A379-A389.

[54] Bitzer, B., and Gruhle, A., 2014, "A new method for detecting lithium plating by measuring the cell thickness," Journal of Power Sources, 262, pp. 297-302.

[55] Downie, L. E., Krause, L. J., Burns, J. C., Jensen, L. D., Chevrier, V. L., and Dahn, J. R., 2013, "In Situ Detection of Lithium Plating on Graphite Electrodes by Electrochemical Calorimetry," Journal of The Electrochemical Society, 160(4), pp. A588-A594.

[56] Shim, J., and Striebel, K. A., 2003, "Effect of electrode density on cycle performance and irreversible capacity loss for natural graphite anode in lithium-ion batteries," Journal of Power Sources, 119(121), pp. 934-937.

[57] Shearing, P. R., Howard, L. E., Jorgensen, P. S., Brandon, N. P., and Harris, S. J., 2010, "Characterization of the 3-dimensional microstructure of a graphite negative electrode from a Li-ion battery," Electrochemistry Communications, 12, pp. 374-377.

[58] Levi, M. D., and Aurbach, D., 1997, "Diffusion Coefficients of Lithium Ions during Intercalation into Graphite Derived from the Simultaneous Measurements and Modeling of Electrochemical Impedance and Potentiostatic Intermittent Titration Characteristics of Thin Graphite Electrodes," Journal of Physical Chemistry, 101, pp. 4641-4647.

[59] Taiwo, O. O., Finegan, D. P., Gelb, J., Holzner, C., Brett, D. J. L., and Shearing, P. R., 2016, "The use of contrast enhancement techniques in X-ray imaging of lithium-ion electrodes," Chemical Engineering Science, 154, pp. 27-33.

[60] Taiwo, O. O., Finegan, D. P., Eastwood, D. S., Fife, J. L., Brown, L. D., Darr, J. A., Lee, P. D., Brett, D. J. L., and Shearing, P. R., 2016, "Comparison of three-dimensional analysis and stereological techniques for quantifying lithium-ion battery electrode microstructures," Journal of Microscopy, 26(3), pp. 280-292.

[61] Zheng, H., Zhang, L., Liu, G., Song, X., and Battaglia, V. S., 2012, "Correlationship between electrode mechanics and long-term cycling performance for graphite anode in lithium ion cells," Journal of Power Sources, 2012(217), pp. 530-537.